2006-01-01

Thermal Sprayed Surface Coatings and Optical Characterisation

Yueqiang Xue
Technological University Dublin

THERMAL SPRAYED SURFACE COATINGS AND OPTICAL CHARACTERISATION

MASTER OF PHILOSOPHY

By

Yueqiang Xue

Supervisors: Dr. David Kennedy
Dr. Emilia Mihaylova

2006

Dublin Institute of Technology

Declaration

I certify that this thesis which I now submit for examination for the award of M. Phil, is entirely my own work and has not been taken from the work of others save and to the extent that such work has been cited and acknowledged within the text of my work.

This thesis was prepared according to the regulations for postgraduate study by research of the Dublin Institute of Technology and has not been submitted in whole or in part for an award in any other Institute or University.

The work reported on in this thesis conforms to the principles and requirements of the Institute's guidelines for ethics in research.

The Institute has permission to keep, to lend or to copy this thesis in whole or in part, on condition that any such use of the material of the thesis is duly acknowledged.

Signature Linh Thuy Dang Date 12/06/2006
Candidate

Abstract

Thermal Sprayed Surface Coatings and

Optical Characterisation

By

Yueqiang Xue

This research work aims to establish the potential of defect detection of thermal sprayed surface coatings by using a newly developed optical non-destructive interferometric technique – Electronic Speckle Pattern Shearing Interferometry (ESPSI), rather than using mechanical destructive testing methods and other non-destructive methods. This technique has been used in many industries for non-destructive testing (NDT). However, it is innovative to use this technique for NDT of thermal sprayed metal alloy coatings, especially those that are produced by flame powder spraying process.

Investigations were carried out by the SUPERJET spray process, which was the flame powder spray process utilised in this research to produce coating samples. Recommendations have been made to optimise the thermal spraying process. Microstructure analysis of various surface coatings was conducted and discussions have been made based on the images obtained. Mechanical measurements were made on a number of thermal sprayed coating samples, including coating hardness measurement, coating surface roughness measurement and coating residual stress measurement. Coating surface roughness was also measured by the White Light Interferometry (WLI) method, and the results obtained were compared with the results obtained by mechanical measurements. The comparisons showed a very good agreement between them.

Defect detections have been made on various coating samples. The results showed that ESPSI technique can be applied successfully to surface coating for quality inspection and it is very effective for delamination detection.

Acknowledgements

I would like to express my gratitude to Dr. David Kennedy of the Department of Mechanical Engineering and Dr. Emilia Mihaylova of the IEO Centre in Dublin Institute of Technology, for their supervision and guidance during the course of the research.

I would also like to thank the academic staff for the help they gave me over the course of my work, especial thanks to Dr. Vincent Toal (Head of School of Physics) and Dr. Suzanne Martin (Manager of the IEO Centre). I am especially grateful to Niall Murphy, James Mahon, Seamus Greene, Martin Wyer and Dennis Mc Keown for their technical support and discussions throughout this work. I wish to thank all of my fellow postgraduate students within Dublin Institute of Technology, for their support and friendship.

Special thanks go to my parents and family for their endless support during my studies. My sincere thanks will be given to Liang Yu for her love, care and encouragement during the course of the work.

Table of Contents

List of Figures

List of Tables

Chapter 1 – Introduction

1.1 ROLE OF SURFACE ENGINEERING

Surface engineering refers to a wide range of technologies that aim to design and modify the surface properties of components. There are two main categories of surface engineering methods that can be used to optimise the surface properties and the bulk materials. These are surface coatings and surface modification, as depicted in Figure 1.1. Other processes involve surface shape design.

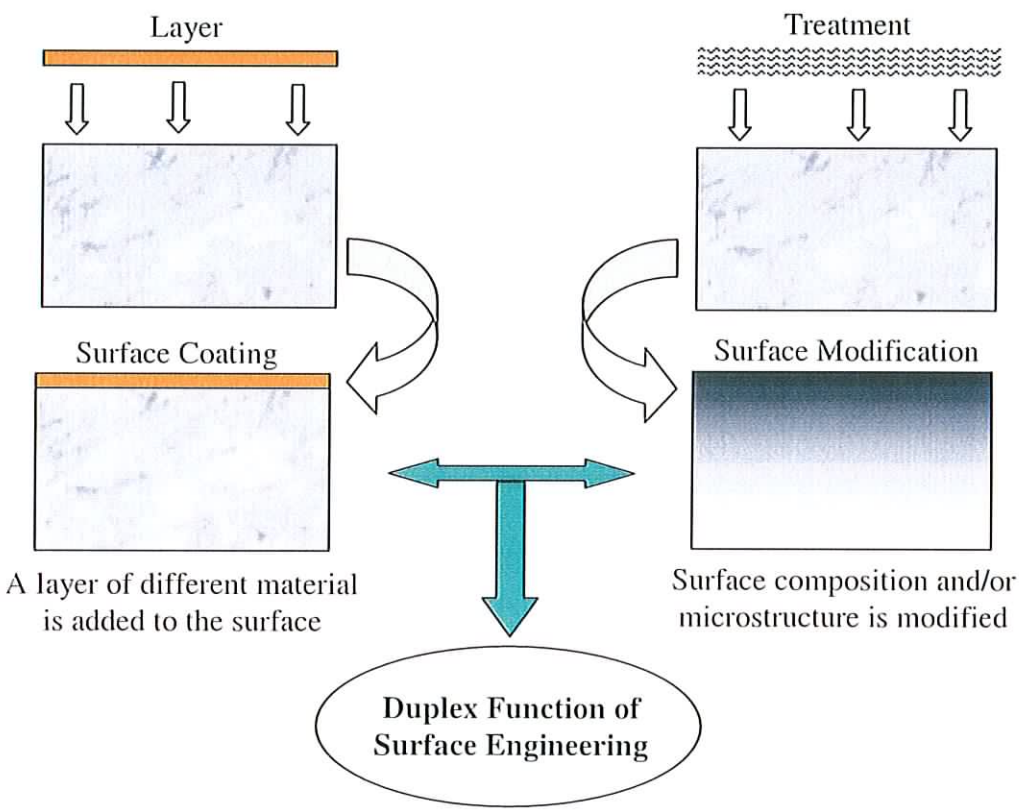

Figure 1.1. Description of Surface Engineering Methods

The applications of surface coatings have been extensively explored. They include aerospace and transport industries, chemical and petroleum industries, food, mining and other manufacturing industries. Recently, surface coatings have been utilised increasingly in some specialised areas. Such applications include the sports industry

[1, 2], biomedical/orthopaedics (e.g. hydroxylapatite), dentistry, cancer therapy, art industry (e.g. glass colouring) and bronze application [3].

The economic benefits of surface engineering are enormous. Matthews and his colleagues have estimated [4] that the UK market for surface engineering processes in 1995 was about £10 billion, of which £4.5 billion was engineering coatings to improve wear or corrosion resistance. These treatments affected manufactured products valued at £95.5 billion (about 7% of UK GDP). It was also predicted that by 2005 the value of the UK coating market would be approximately £21.3 billion, and those coatings would critically affect products with a value greater than £143 billion.

Surface coating processes involve depositing a layer of molten or semi-molten material onto the surface of a substrate. One of the main functions of a surface coating is to modify and reinforce the surface functions instead of reforming the composition of the bulk material. Some examples of surface coating processes include thin film coatings such as Physical Vapour Deposition (PVD) and Chemical Vapour Deposition (CVD), thermal spraying, sol-gel, cladding and electroplating [3]. Surface modification processes can be classified as hardening by flame, induction, laser or electron beam; high energy treatments (e.g. ion implantation); and diffusion treatments (e.g. carburising and nitriding). Surface modification processes are applicable to control friction, improve surface wear and corrosion resistance, and change the physical or mechanical properties of components. Surface modification treatments can be combined with surface coating processes, as in laser cladding. This combination enhances the advantages of surface coatings and surface modification, thus achieving specific requirements and fitness for purpose.

1.2 RESEARCH BACKGROUND

Thermal spraying is regarded as one of the key enabling surface engineering technologies. Since the thermal spraying technique was invented in the early part of the twentieth century, the use of thermal sprayed coatings has grown enormously and they are extensively used across the whole spectrum of engineering industries [5-7]. A variety of engineering problems have been solved using thermal spraying applications and as research continues the application of this coating technique may be used in engineering areas otherwise not considered [8,9].

In the thermal spraying processes, the consumable coating materials are fed to the spray gun and the temperature is adequate to melt the materials. Then they are projected in a particulate form towards a workpiece forming a coating of desired thickness. Thermal spraying techniques include flame spraying, arc spraying, plasma spraying, High Velocity Oxyfuel spraying (HVOF) and detonation flame spraying [3].

Flame powder spraying is one of the most commonly used and simplest thermal spraying methods. It is the most suitable flame spraying process for high alloy and self-fluxing surfacing materials. It is extensively used for wear-resistant coatings of nickel or cobalt base alloys, and the restoration of worn surfaces. In this research, the Castoline Eutectic's SUPERJET spray unit is throughout used as the spraying equipment to produce coating samples, and the coating material used in this project are all nickel based metal alloys.

Thermally sprayed nickel-based alloy coatings are used in a variety of applications. For example, they are extensively used as bond coats for thermal barrier coatings (TBCs) on turbine components and in internal combustion engine cylinders. They are also used for corrosion protection of boiler tubes and for machine parts as restorative layers, and in other numerous applications requiring wear-, high temperature- and corrosion-resistant surfaces [3, 10-12].

The principle of thermal spraying is that the coating materials are deposited on the substrate surface of a component to form a layer with a different material composition. Thus the combination of the coating and the substrate might be considered as a composite structure. Composite structures normally have a high possibility of having flaws due to the rules of formation and processing methods. It is important to have access to non-destructive testing (NDT) techniques to evaluate the structural integrity of the reinforced layer and the component substrate. Consequently, there is a need for inspection of surface coatings to assess deposition quality, and ensure performance during service life. Optical methods such as holography, Electronic Speckle Pattern Interferometry (ESPI), Electronic Speckle Pattern Shearing Interferometry (ESPSI), Moiré techniques and Thermography are emerging as strong candidates for industrial inspections.

1.3 AIMS AND OBJECTIVES

The main aim of this project was to apply non-contact optical techniques to the study of thermal sprayed surface coatings, focusing on the coating defect detection using the optical methods. The objectives were to:

i. Research various surface coating techniques and testing methods (mechanical and optical);
ii. Prepare substrate of different materials (steel, copper, aluminium and plastic);
iii. Deposit coatings of various types (all are Nickel based metal alloys) using thermal spraying coating process;
iv. Carried out mechanical measurement and testing of coatings (hardness, surface roughness, Young's Modulus and residual stress);
v. Perform optical characterisation of coating surface (microstructure and surface roughness), coating defect detection and analysis using optical methods;
vi. Compare the results obtained from the two measurements;
vii. Report on the benefits of optical processes for coating evaluation.

White Light Interferometry (WLI) was used for the measurement of coating depth and wear mark profiling. ESPSI was used for delaminations and crack detection. For coating surface roughness measurement, a comparison was made between the results obtained from mechanical and optical measurements.

1.4 MOTIVATION OF RESEARCH

The literature covers the topic of mechanical testing and measurements of surface coatings, including thermally sprayed coatings. However, most of the mechanical testing methods are destructive and they have contact to the specimen or the component being investigated. It can be the main drawback of mechanical measurements. NDT methods will be the solution for eliminating this shortcoming.

Within the domain of NDT methods, various techniques have been used for the testing of defects of materials. These include eddy current, ultrasonic, X-ray, radiography and optical methods. Optical methods – specifically laser interferometry

methods, which normally refer to holography, ESPI and ESPSI that have been developed during the past four decades, have proved to be very useful and powerful tools in the NDT of structures and materials [13]. Of particular interest to the current study is the ESPSI method.

ESPSI, is also called shearography, has been developed over the past two decades and has proved to be a very useful tool in NDT of various applications for defect detections (e.g. structure, tyres) based on its advantages of non-contact, real time and fast full-field inspection [14-16]. Very few researcheres have considered the application of thermal sprayed surface coatings for ESPSI testing. Thermal sprayed coated products may have defects such as debonding and delaminations due to the inappropriate control of the process. Shearography would seem to be well suited for defect detection of thermal sprayed surface coatings. This research work developed and discussed a new application of shearographic interferometry technique to the NDT of thermal sprayed coating surfaces.

1.5 SUMMARY OF THE REPORT

The report is divided into seven sections. Following the introduction, chapter two is a review of literature relevant to the study. This is supplemented by journal publications and industry data. Various thermal spraying techniques are discussed, in terms of their function and performance. Different testing and characterisation methods including destructive and non-destructive methods have been discussed in terms of coating's microstructure and mechanical properties.

The theory of laser interferometry techniques are discussed and presented in chapter three. The experimental equipment utilised in the thermal spraying coating process is presented in chapter four, along with associated procedures. The chapter also includes a description of equipment used for measurement of coating properties and defect detections of the coatings.

In chapter five, experimental test results are presented and discussed. A brief list of experiments carried out in this research is shown in Figure 1.2. Chapter six summarises conclusions from the results found within the present research, and presents recommendations for future research.

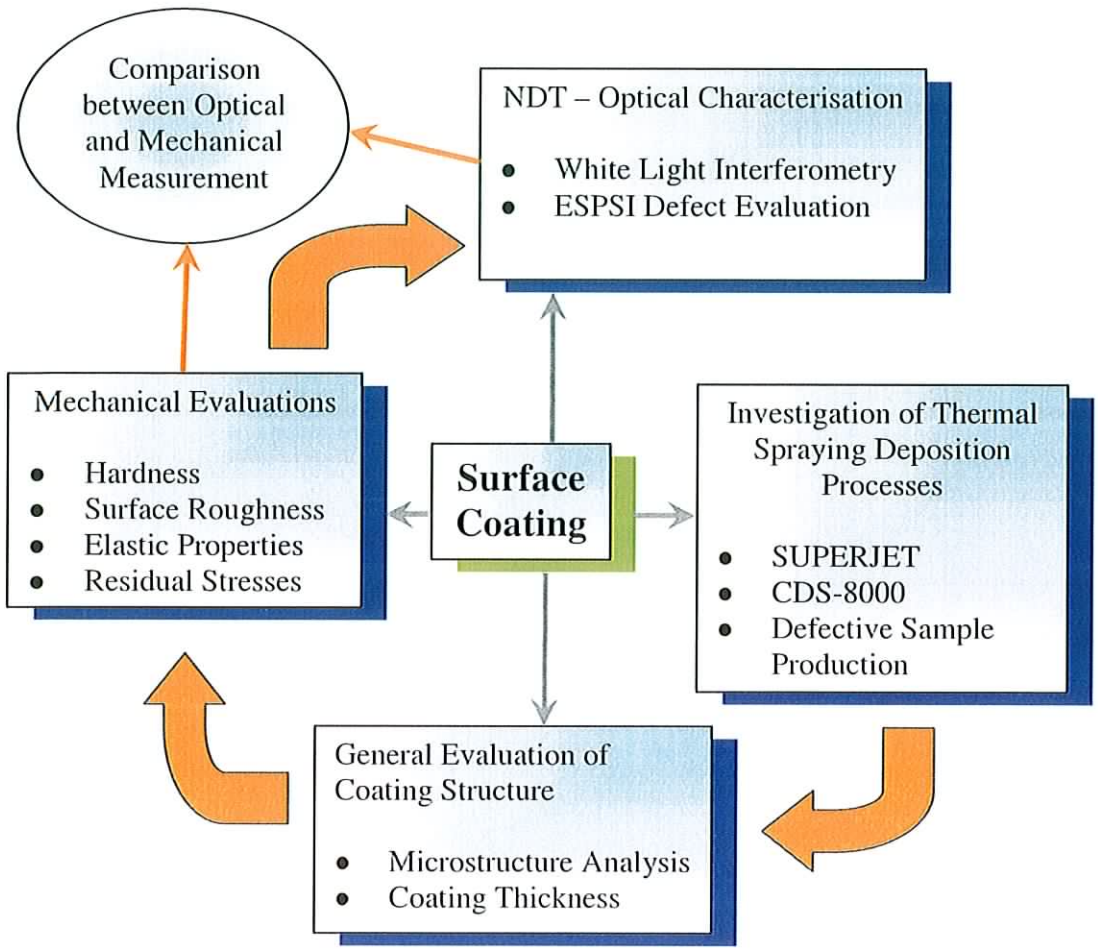

Figure 1.2. Brief List of Experimental Work Carried Out in the Current Research

Chapter 2 – Literature Survey

2.1 SURFACE ENGINEERING

Surface engineering may be defined as "the design and/or modification of a surface and substrate of an engineering material together as a system, to give a cost effective performance enhancement of which neither is capable alone" [17, 18].

The majority of engineering failures arise from deficiencies of the surface material in dealing with fatigue, friction, wear, corrosion, electrical and thermal contacts, etc. In some instances these failures are exacerbated by high surface stress due to bending and/or torsion. The surface material is the only part of any component which has to coexist with the external environment such as contacting surfaces and chemical attack [19].

Many materials have been developed to have specific bulk properties, although they have not been particularly optimised for the surface properties. Surface engineering can solve these problems by:

i. Implanting alloying atoms to different depths, thereby improving toughness and fatigue properties; (surface modification)
ii. Depositing surface layers, thick or thin, including lubricants; (surface coating)
iii. Redesigning the surface shape of the component to distribute stresses.

Since technological progress and manufacturing efficiency sometimes may be constrained by surface requirements, the choice of the surface material becomes very crucial. Functionally, a surface material requires appropriate thermal, optical, magnetic and electrical properties and sufficient resistance to wear, corrosion and degradation. However, it is often impractical, inefficient or uneconomical to manufacture components from a bulk material simply for its surface properties. A better solution will be to use a cheaper, more easily formed underlying material and coat it with a suitable high performance coating. The resulting product conserves scarce material resources, performs better than the original and may be much cheaper

to produce. Surface engineering technology provides effective solutions to extreme applications.

Surface engineering is able to offer enormous potential for improving the functionality of an existing product. Also, new coating technologies and treatment processes may create opportunities for new products which could not otherwise exist. For example, satellites could not function in the sever environment of outer space without the application of advanced surface engineering techniques. Furthermore, modern power plants could not operate safely without the applications of surface engineering.

It is of great benefit to have the technology to simplify product ranges or maintenance requirements, make mechanisms lighter, reduce noise, and enhance the value of strategically or economically advantageous materials [20]. Surface engineering also plays a considerable role in the area of environmental design [21]. In brief, surface engineering can increase performance, reduce costs and control surface properties independently of the substrate.

2.2 ENGINEERING ENVIRONMENT

When two surfaces come into contact and relative motion is generated, the contact stresses increase due to the relatively small percentage of load-supporting area. This will result in friction and wear, and possibly even lead to failure. In the high stress applications of a modern engine or gearbox, there are areas where the pressure of metal moving against metal forces away all the lubricating oil and allows heat to build up. Figure 2.1 shows a set of spiral gears in contact.

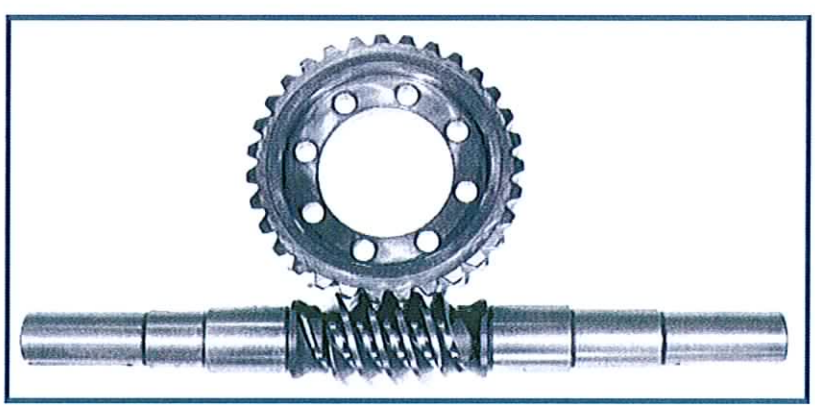

Figure 2.1. A Set of Spiral Gears in Contact

In the case of extreme pressure and friction, this heat is enough to instantaneously weld the two parts together just before they are broken apart by their movement. This constant weld and break process is destructive, and it can result in drag and wear. If the gears are the components of a spacecraft, and if the single part fails, the entire multi-million dollar spacecraft would fail. So engineered surfaces to combat friction and reduce wear is highly desirable.

Surface engineering refers to a series of techniques of dealing with friction, corrosion and wear problems. Friction, corrosion and wear are the most common factors that cause engineering failures. In industrialised countries, 7% of GNP represents the cost of friction, wear and corrosion, with the possibility of 1% of this figure being reduced through the use of efficient tribological systems, including lubricants, surface coatings, etc. On a worldwide level, 34% of all lubricants produced are consumed in Europe, with 50% of these being recycled, with a further 2.5 million tonnes being lost within the environment [17]. A deep understanding of friction, corrosion and wear is necessary for making the best choice of material selection under specified conditions.

2.2.1 Friction

Friction is the resistance to relative motion of contacting bodies. There are two modes of friction that may occur: sliding and rolling friction. Rolling friction is a complex phenomenon because of its dependence on so many factors, including inconsistent sliding during rolling, and energy losses during mixed elastic and plastic deformations. The sliding friction is due to the combined effects of adhesion between flat surfaces, ploughing by wear particles and hard asperities, and asperity deformation. The degree of friction is expressed as a coefficient of friction, μ, which is expressed as the ratio of force required to initiate or sustain relative motion, to the normal force that presses the two bodies together.

2.2.2 Corrosion

Corrosion is a surface electrochemical phenomenon which occurs when metals react with non-metallic elements of their environment. In engineering applications, corrosion is most commonly presented as the formation of metal oxides from

exposure to air and water from the environment. Anti-corrosion processes produce a surface that is less chemically reactive than the substrate material. Corrosion costs in the UK and USA are approximately £30bn and $276bn every year respectively [17, 22]. Figure 2.2 shows the basic types of corrosion.

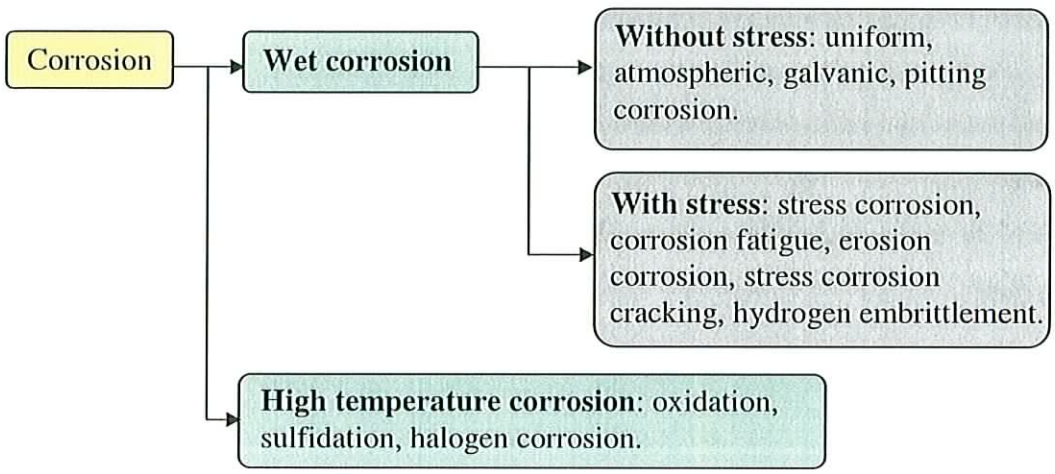

Figure 2.2. Types of Corrosion

2.2.3 Wear

Wear is a process of removal of material from one or both of the two contacting solid surfaces in solid state contact, occurring when two solid surfaces are in sliding or rolling motion together, according to Bhushan et al. [23]. Figure 2.3 shows the five main categories of wear and the specific wear mechanisms that occur in each category. Wear is an inevitable and self-generating process. It is defined as "damage caused by the effects of constant use" and is perhaps the most common process that limits the effective life of engineering components. Among the different types of wear, abrasive wear and adhesive wear normally occur more often than others. Abrasive wear is due to hard particles or hard protuberances forced against and moving along a solid surface. Adhesive wear is caused by localised bonding between contacting solid surfaces leading to material transfer between the two surfaces or the loss from either surface. Adhesive wear is a typical example of how a soft material can wear down a harder one.

The higher the hardness of a coating, the better a coating can protect a surface from wear. Hardness is a necessary but not sufficient property of a coating to protect against wear. In addition to hardness, coating surfaces should have low coefficients of friction against themselves and against other coatings or substrate materials in order to reduce wear.

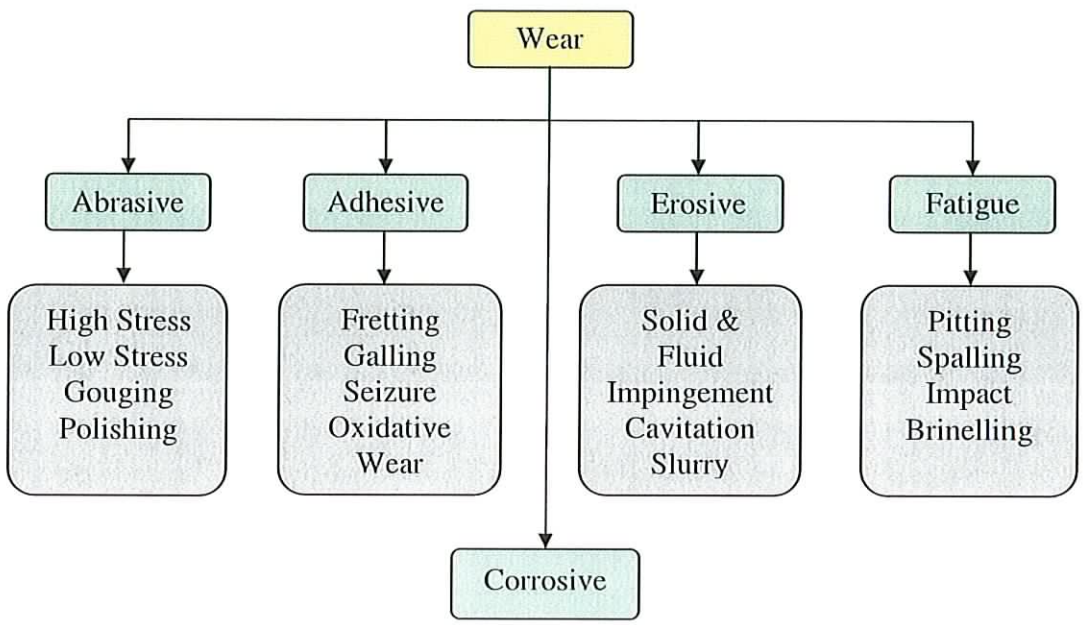

Figure 2.3. Types of Wear

Figure 2.4 demonstrates the phenomenon of abrasive and adhesive wear [123]. The use of surface engineering processes can effectively reduce the amount of wear on engineering components thereby extending the useful life of the product.

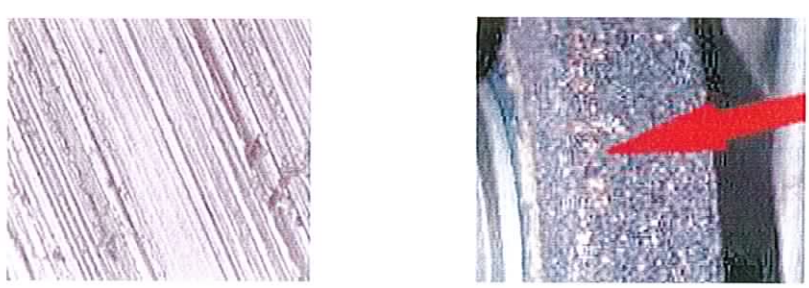

(a) (b)

Figure 2.4. Demonstration of Wear: (a) Abrasive Wear; (b) Adhesive Wear

2.3 SURFACE COATING TECHNIQUES

A coating is a material which is converted to a solid protective or functional adherent film after deposition or addition onto another material. The main purposes of all the coating techniques may be summarised as follows:

i. Aesthetic reasons, to improve the surface appearance
ii. To protect surfaces from wear, corrosion and other factors that cause engineering failure
iii. To be cost effective
iv. To simplify mechanism of structure

There are many coating deposition techniques available. The selection of the best process depends on the coating function requirements, the state of the substrate (shape, size and metallurgy), the level of adherence requirement, the cost of the equipment and the adaptability of the coating material to the process. The commonly used coating deposition processes are summarised in Figure 2.5, which is adapted from [23].

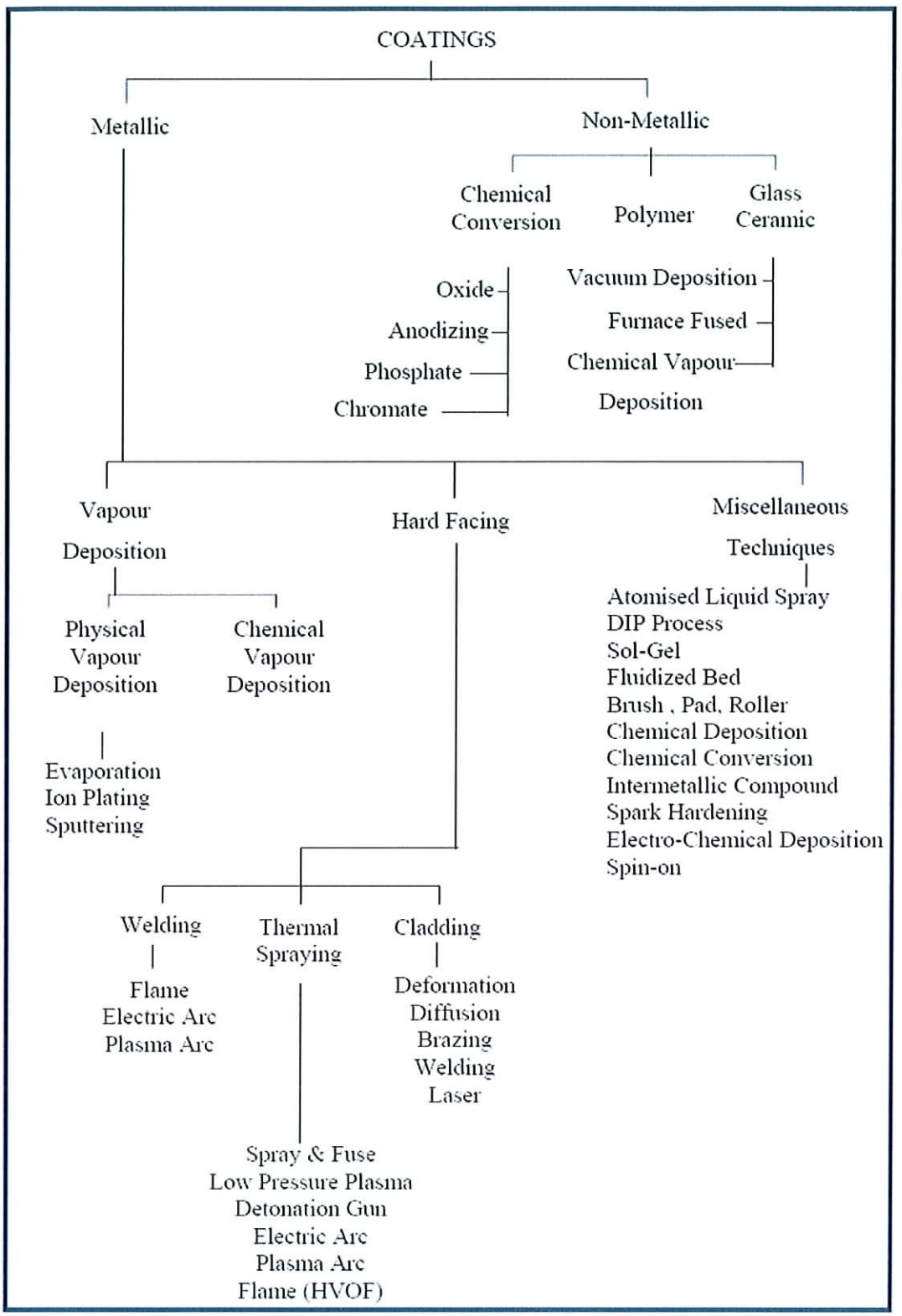

Figure 2.5. Summarised Surface Coating Deposition Techniques, Adapted from [23]

2.3.1 Thermal Spraying Processes

Thermal spraying is one of the most versatile hard facing techniques available for the application of coating materials. It is used to protect components from abrasive wear, adhesive wear, erosive wear, surface fatigue and corrosion [24].

In the early twentieth century, the thermal spray technique was invented by a Swiss inventor, Dr. Max Schoop, when he was watching his son playing with his toy cannon. Dr. Schoop noticed that the hot lead shots that were projected out of the cannon, stuck to almost any surface. This gave him the idea that if metal could be melted and projected in a spray like manner, then a surface could be built up with that material. According to Dusa [25], Schoop designed a gun which used oxygen and acetylene as the heat source and compressed air to project the molten material, as shown in Figure 2.6.

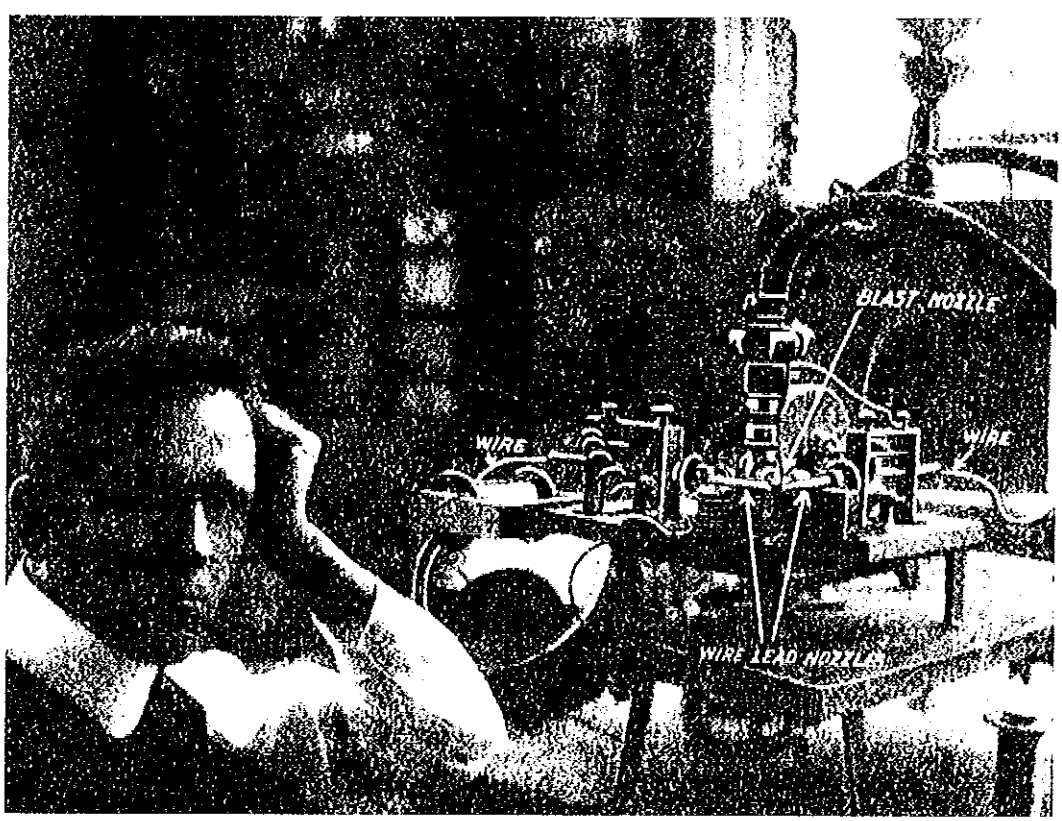

Figure 2.6. Dr. Schoop in 1914 and His First Experimental Electrically-Operated Metal-Spraying Apparatus [25]

The feedstock material, which can be in the form of powder, rod or wire, is melted and propelled in the effluent of a flame. The high temperature for melting is achieved chemically (through combustion) or electrically (through an electrical arc). The molten particles are accelerated and impinged onto the target substrate, where the material solidifies forming a deposit. Figure 2.7 depicts the impingement of a spherical particle during the thermal spraying process. The desired layer is built-up by successive impingement of these individual flattened particles or splats.

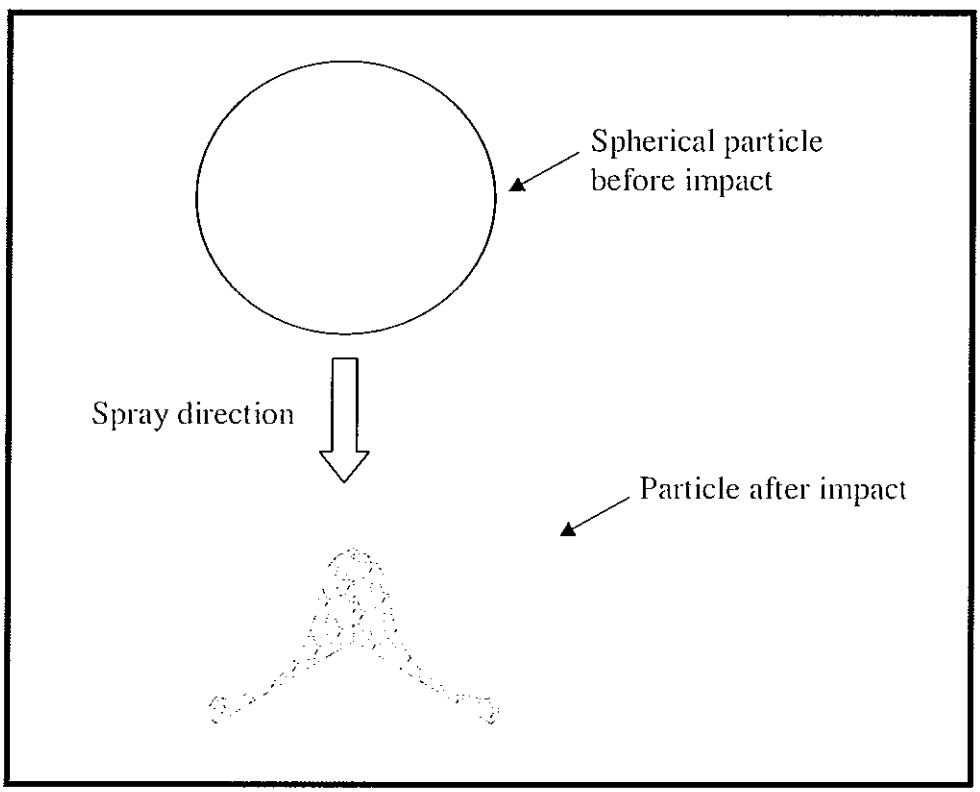

Figure 2.7. Schematic Diagram of Thermally Sprayed Spherical Particle Impinged onto a Substrate

During the thermal spray process, the particle transfers its kinetic and thermal energy to the surface [26]. The high kinetic energy leads to a plastic deformation of the droplets at the surface to be coated. Afterwards, fast cooling and shrinking make the droplets clamp onto the surface profile and allow for only partial alloying.

There are various methods that can be used for the classification of thermal spraying processes. For example, the processes can be classified based on the thermal spray source, from low velocity combustion spray to high temperature plasma jets, or

based on the method of material injection, in the form of powder, wire or rod [11]. Thermal spraying processes can also be categorised into two groups based on the energy transfers during the processes. They are the high energy process and low energy process [3].

Lower energy thermal spray processes, referred as metallising, including flame and arc spraying. They are normally used for spraying metals for corrosion resistance, for service at or near ambient temperature, on large structures and where thermal and mechanical shock or abrasive wear are small. They are normally of lower capital cost and are relatively portable.

2.3.1.1 Flame Spraying

i. Oxyfuel gas wire spraying

Oxyfuel gas wire spraying is extensively used for deposition of zinc and aluminium coatings for corrosion protection. It consists of relatively low cost equipment, lower density deposits and lower adhesion strength than arc spray.

ii. Oxyfuel gas powder spraying

Oxyfuel gas powder spraying is the most suitable flame spraying process for high alloy and self-fluxing surfacing materials. It is extensively used for wear-resistant coatings of nickel or cobalt base alloys, and the restoration of worn surfaces. This process provides lower density deposits and lower adhesion strength than arc spraying. The consumable is in the form of powder, and various materials can be used for the process (carbides, oxide ceramics, cermets, etc.). The powder may be fed either by gravity or by a more sophisticated pressurised supply. Flame sprayed coating are normally used in thickness ranging from about 50μm up to several millimetres. Flame spraying can be used to provide protection against corrosion at ambient and elevated temperatures and for salvage of worn or mismachined parts, the most prevalent use of the process is in providing resistance to wear, abrasion and erosion [27].

Spray fusing is one type of process of flame powder spraying. In spray fusing, the coating is heated after deposition and by using a torch to fuse the material into a

dense alloyed structure, a diffusion bond to the substrate is produced. In this research, the SUPERJET spray process, which is a spray fusing process, is used throughout the experiments. Figure 2.8 shows a schematic of the flame powder spray process.

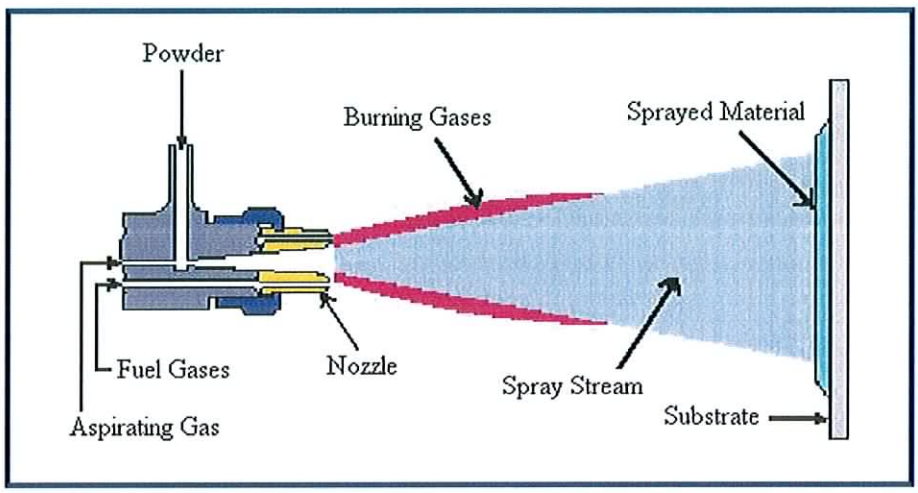

Figure 2.8. Scheme of Flame Powder Spray Process

iii. Arc Wire Spraying

Arc wire spraying is suitable for surfacing large components. A wide range of coating alloys (solid or tubular wires) can be applied. By using two different wires, composite or "pseudo-alloy" coatings can be produced. This process has lower density deposits and lower adhesion strength than the high velocity processes.

Higher energy thermal spray processes normally include plasma spraying, detonation gun and high velocity oxyfuel spraying. They are generally used for coatings which are required to have resistance to higher temperatures and to thermal and mechanical shock. However, they have higher capital cost and are normally used in fixed installations.

2.3.1.2 Plasma Spraying

Plasma spraying processes generally include air plasma spraying (APS) and vacuum plasma spraying (VPS). APS is used for the application of electrical and thermal insulating coatings, and it is used mostly for deposition of refractory high melting point materials, (e.g. ceramics, carbides and high temperature alloys). Figure 2.9 shows a schematic diagram of a plasma powder spray process. The coatings

produced have high density and are strongly bonded to the substrate. The process has low heat input to the substrate, while having higher capital cost than gas and arc spraying. VPS is normally carried out in a chamber, where the oxygen is evacuated. The coatings produced have high density and adhesion. However, the process has high capital cost, and requires fixed installation.

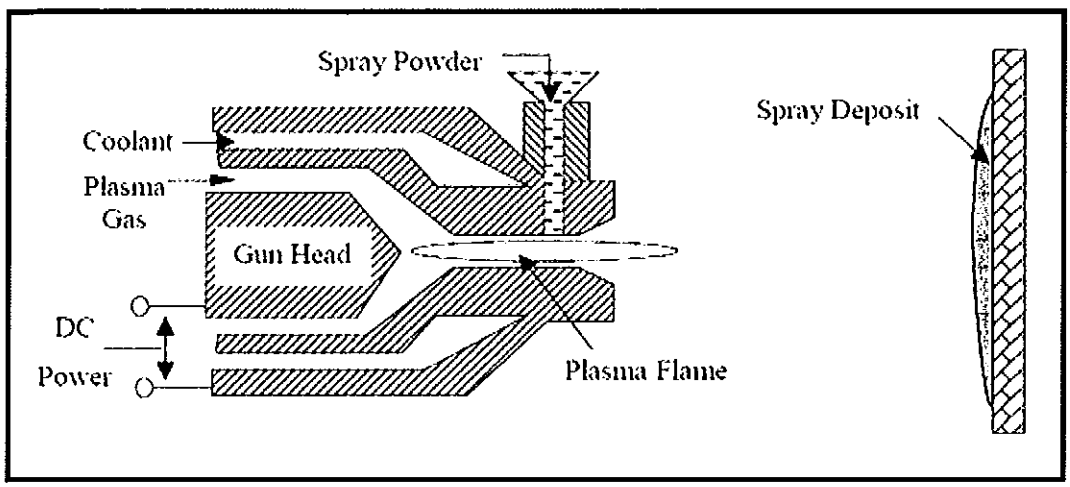

Figure 2.9. Scheme of Plasma Spray Process

2.3.1.3 Detonation Spraying

Detonation spraying is a proprietary process. A device similar to rifle barrel has powdered coating material and an oxygen/acetylene gas mixture metered into it, which is then ignited by a spark discharge. The mixture is detonated and the powder is propelled from the barrel at high temperatures and velocities up to 760m/s. The operating cycle is repeated four to eight times per second to provide a continuous deposit. It is used for protection of gas turbine engine parts against various forms of wear at high temperature. It also has applications in textile machine parts, paper and plastics industries, the nuclear industry and in cutting edges. The coatings produced have very high density and adhesion deposits.

2.3.1.4 High Velocity Oxyfuel Processes (HVOF)

The HVOF process is a popular thermal spraying technique and has been widely adopted by many industries due to its flexibility and the superior quality of coatings produced. The HVOF process is a thermal spray process that offers coatings with

higher bond strengths and hardness together with lower porosity, compared to other thermal spray techniques [24, 28-30]. The fuel gases include hydrogen, propane and propylene.

2.3.2 Summary of Thermal Spray Processes

The thermal spraying processes and equipment described are the general types used for the deposition of sprayed material. Table 2.1 shows some of the important characteristics associated with these techniques along with those of the flame powder spray technique, which is under investigation in the present study.

Characteristics	**Flame ***	**Arc**	**Plasma**	**HVOF**
Form of coating material	Powder / Wire	Wire (conductive)	Powder	Powder
Heat source	Gas combustion	Electric arc	Plasma (electrical)	Gas combustion
Propellant	Combustion flame	Compressed air	Plasma (gas expansion)	Combustion flame
Process energy level	Low	Low	High	High
Particle Velocity (m/s)	40	100	200-300	600-800
Adhesion (MPa)	<8	10-30	20-70	>70
Porosity (%)	10-15	5-10	1-8	1-2
Deposition Rate (kg/hr)	1-10	6-60	1-5	1-5
Deposit Thickness (mm)	0.2-10	0.2-10	0.2-2	0.2-2

Table 2.1. Comparison of Thermal Spraying Processes, Adapted from [3, 20]

2.3.3 Cold Spray

Cold spray is a novel method, where the particles are supersonic at or near-ambient temperatures. The process does not involve any melting and entire deposition takes place in solid state. Such differences in particles conditions affect particle/droplet flattening behaviour, solidification rates and environmental interactions of particles. This can yield different microstructures, residual stresses, physical properties and performance [11].

2.3.4 Electrodeposited Coatings

Electrodeposition or electroplating involves making the component to be coated the negative electrode or cathode in a cell containing a liquid or electrolyte which must allow the passage of electric current. Electrodeposition is not only used to apply coatings to new components to confer the required surface properties, but also to restore the dimensions of parts that have either worn excessively in service or been so over-machined as to be outside required tolerances [3].

2.3.5 Physical and Chemical Vapour Deposition

Physical vapour deposition (PVD) and Chemical vapour deposition (CVD) are two techniques confined to making thin films, thickness ranges from 2-10 microns. Both vapour processes involve treatment in a chamber – either in a vacuum chamber or in one that can withstand the high temperature and corrosive gases used in CVD. Figure 2.10 shows the schematic principle of PVD and CVD processes.

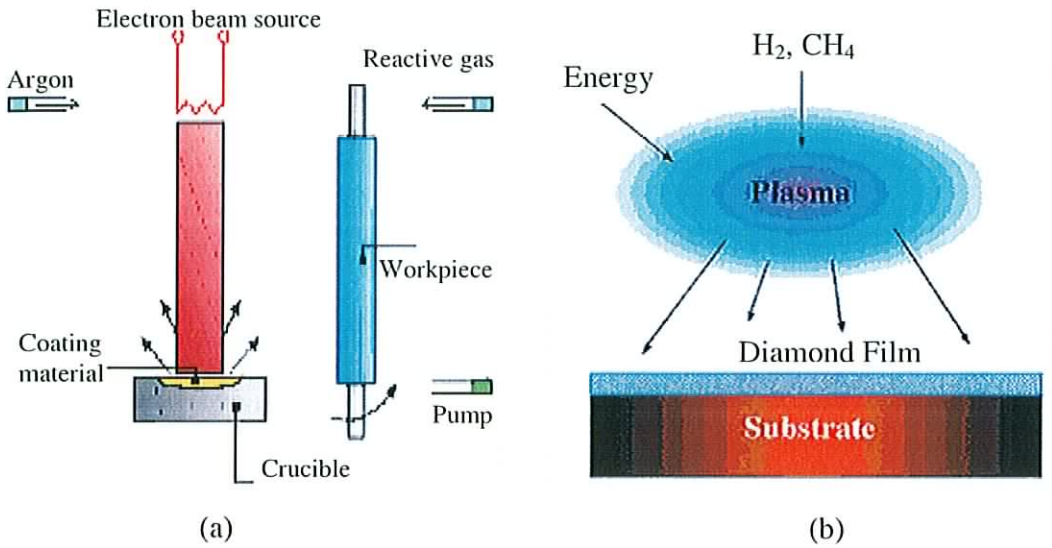

Figure 2.10. Schematic Principle of PVD and CVD Process: (a) PVD; (b) CVD.

PVD coating vapours are generated either by evaporation from a molten source, or by ejection of atoms from a solid source that is undergoing bombardment by an ionised gas (i.e. sputtering). The vapour may then be left as a stream of neutral atoms in a vacuum (vacuum evaporation) or it may be ionised to a greater or lesser extent. A partially ionised stream is usually mixed with an ionised gas and deposits on an earthed or biased substrate (ion plating and sputter coating), but a highly ionised stream that forms a plasma is attracted to a biased substrate (arc plasma evaporation). Alternatively a 100% ionised beam may be focused and accelerated to sufficiently high energies to penetrate the substrate (ion implantation).

Chemical vapour deposition (CVD) is the formation of a solid layer from the gaseous phase via a chemical reaction. It is sometimes known as gas plating [31]. The coating materials include metals, especially refractory Titanium Nitride and other compounds. The coatings are used for thin, wear-resistant films on metal and carbide dies, and tools. In general, there are three steps in the CVD reaction:

i. The production of a volatile carrier compound, e.g. nickel carbonyl
ii. The transport of the gas, without decomposition, to the deposition site
iii. The chemical reaction necessary to produce the coating on the substrate

2.3.6 Thermal Spray Coatings on Plastic Substrates

Most of the thermal spray coatings on plastic substrates are based on copper, zinc and aluminum, which are mainly used for Radio Frequency Interference (RFI) shielding and electrical conductivity where mechanical properties of the coating are not of prime importance [32].

In many applications, cheap, light and flexible plastic materials are replacing the glass and crystal optic materials. Due to the high temperature sensitivity of plastics, they can only be coated using processes running at low temperatures (<100°C). Therefore, coating deposition at low temperatures becomes very important.

The use of reinforced plastics is an attractive option over metals in some components because of the good strength to weight ratio. The disadvantage is the poor surface properties. Recent development work has indicated promise for engineering type thermal spray coatings on fibre reinforced polymers, as shown in Figure 2.11.

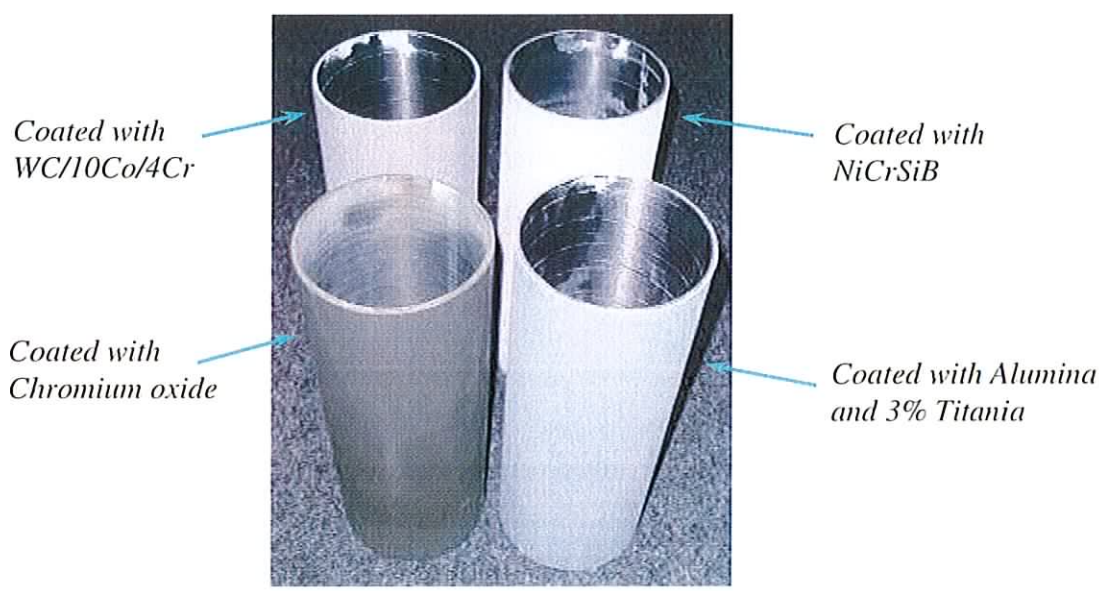

Figure 2.11. Thermal Sprayed Coatings on Carbon Fibre Reinforced Polymer Tubes

2.4 TESTING AND CHARACTERISATION OF COATINGS

2.4.1 Testing Methods

Inspection and testing are essential engineering activities at many stages in the complex process of producing engineering materials. There are many types of testing methods which are applicable to surface coating inspections, and they are generally categorised as destructive testing and non-destructive testing (NDT). Destructive testing is used to establish the properties of the material while NDT is used for determining the integrity of the material or component, and used to detect the presence of internal or surface flaws in a material, component or finished product [33]. Destructive testing is used to ensure the sample material property meet the appropriate specification and give the required performance. NDT will be undertaken to check if a product is defect-free prior to final assembly. NDT is also used for the in-service checking of components to detect deterioration or damage, for example the presence of corrosion and fatigue cracks [33].

2.4.2 Mechanical Testing

Almost all the mechanical testing methods are destructive and result in the specimen's failure. However, these tests are generally much easier to carry out, yield more information, and are easier to interpret than NDT.

Since some coatings are less dense and less homogeneous, and as adhesion tends toward mechanical rather than a metallurgical mechanism, destructive techniques such as adhesion tests and metallography is more reliable than the NDT. In some way, destructive testing on a small percentage of the component surface is acceptable where large numbers of similar articles are being processed [3].

Various mechanical testing methods are applicable to surface coating evaluation. These include hardness testing, residual stress measurement, wear, abrasion and adhesion testing, tensile and bending strength test, roughness measurement.

2.4.3 Coating Characteristics and Properties

The coating characteristics and properties that are investigated in this report include hardness, elastic modulus, roughness and residual stress. The coating hardness and coating surface roughness are especially emphasised since they are two very important parameters for determining the coating tribological behaviour [34]. These will be discussed in the following sections.

2.4.3.1 Hardness

In material science, hardness is the characteristic of a solid material expressing its resistance to penetration, and by extension its power of penetration in softer materials [3]. Hardness is also an essential tool for measuring yield stress [35].

It is known that an object made of a hard material will scratch an object made of a softer material. Pure diamond is the hardest known substance, so it will scratch any other material. Therefore, most hardness testers have been equipped with a diamond tip.

One of the main reasons for coating a substrate material is to protect a substrate against excessive wear. One of the properties of such a coating is that it must be hard. Hardness test on a coating will give a general indication of the coating quality. However, in some cases, the presence of porosity may lead to a lower hardness value compared with that of a similar solid material. Additionally, the presence of a hard substrate with a thin soft surface coating will give a hardness that is affected by deposit thickness [3].

There are some requirements for a surface which is being tested for hardness [36]. Examples include, the surface has to be smooth, with a sufficiently low roughness and without any foreign particles on the surface. Testing and bearing surfaces have to be even and parallel to each other.

Hardness tests can be made by means of indentation, scratch, abrasion and erosion tests. In indentation hardness test, the hardness is evaluated by the amount of permanent deformation or plastic flow of the material. In scratch hardness test, the

material being tested is scratched by the diamond and the scratch is compared with standard limit scratches in the microscope eyepiece [36].

Hardness measurement can be defined as Macro-, Micro- or Nano- scale according to the forces applied and displacements obtained.

i. Macro-Hardness

Macro-hardness measurement of materials is a quick and simple method of obtaining mechanical property data for the bulk material from a small sample. It is also widely used for the quality control of surface treatments processes. However, when concerned with coatings and surface properties of importance to friction and wear processes for instance, the macro-indentation depth is too large relative to the surface-scale features. Many standards and reports outline how these tests are carried out [37, 38].

Where materials have a fine microstructure, are multi-phase, non-homogeneous or prone to cracking, macro-hardness measurements will be highly variable and will not identify individual surface features. However, micro-hardness measurements will be appropriate for these situations.

ii. Micro-Hardness

Micro-hardness is determined by forcing an indenter such as a Vickers or Knoop indenter into the surface of the material under 1 to 1000gf load. Micro-hardness is evaluated by measuring the area of the indentation rather than the depth [36]. Most micro hardness testing is typically performed on samples that have been metallographically mounted and polished. The ideal surface finish is a high-quality metallographic polish. Micro-hardness testing is appropriate for many coating measurements but it must be measured with a microscope. There are many standards that outline micro-hardness tests to evaluate the hardness of a coating, including the standard ISO 4516 [39].

iii. Nano-Hardness

Nano-indentation tests measure hardness by applying very small penetration forces of a few μN up to 5mN, which result in very small indentation depths in the material investigated [40]. Nano-indentation can extract more information from the indentation procedure by means of a dynamic measuring principle by recording a set of data of the penetration depth with increasing load up to a maximum force value and then with a decreasing force. The plastic and the elastic parts of the indentation can be separated from analysis of the depth–force curves [41]. This leads to the concept of universal hardness, which is defined slightly differently to that of conventional Vickers hardness.

2.4.3.2 Hardness Measurement Methods

The hardness measurement is to determine the resistance of the test piece to the penetration of a non-deformable ball or cone, under a given load, within a specific period of time. There are five types of methods that are commonly used for hardness measurement: Brinell, Rockwell, Vickers, Knoop and Shore hardness test. Vickers type hardness test was used throughout this research to measure the hardness of the coating samples.

Vicker's hardness testing method was devised in the 1920s by a group of engineers from Vickers Ltd. in United Kingdom. Vicker's hardness is a measure of the hardness of a material, calculated from the size of an impression produced under load by a pyramid-shaped diamond indenter. This pyramid hardness test permitted the establishment of a continuous scale of comparable numbers that accurately reflected the wide range of hardness found in steels. The Vickers test is reliable for measuring the hardness of metals, and it is also used on ceramic materials.

The indenter employed in the Vickers test is a square-based pyramid whose opposite sides meet at the apex at an angle of 136°. The depth of indentation is about 1/7 of the diagonal length. The diamond is pressed into the surface of the material at loads ranging up to approximately 120 kilograms-force, and the size of the impression (usually no more than 0.5mm) is measured with the aid of a calibrated microscope. The Vickers number (HV) is calculated using Equation 2.1 [36]:

$$HV = 2P\sin\frac{(\theta/2)}{D^2} = \frac{1.8544P}{D^2}$$ Equation 2.1

Where P = Applied load (kgf)

D^2 = Area of the indentation (mm^2)

θ = The angle between opposite faces of the indenter (136°)

2.4.3.3 Microstructure Analysis

Microstructure analysis of thermal sprayed coatings is important in this research work. Optical microstructural characterisation techniques have become standard testing methods in surface coating development. There are numerous optical techniques available for microstructure analysis, including the Optical Microscope (OM), Scanning Electron Microscope (SEM) and X-ray Diffraction (XRD). Microstructure analysis is able to provide information such as chemical composition, grain morphology and orientation, coating porosity percentage and coating thicknesses. Also, mechanical properties such as micro-hardness, tensile strength, fracture strength, elastic modulus, toughness, and wear resistance can all be identified using optical techniques [42].

2.4.4 Surface Roughness

2.4.4.1 Surface Topography

Surface topography is important in specifying the functions of a surface. A significant proportion of component failure begins from the surface due to either the manufacturing discontinuity or the gradual deterioration of the surface quality. One of the most important parameters describing surface integrity is surface roughness. According to the British Standard BS EN ISO 4287:2000 [43], surface can be assessed by the procedure shown in Figure 2.12.

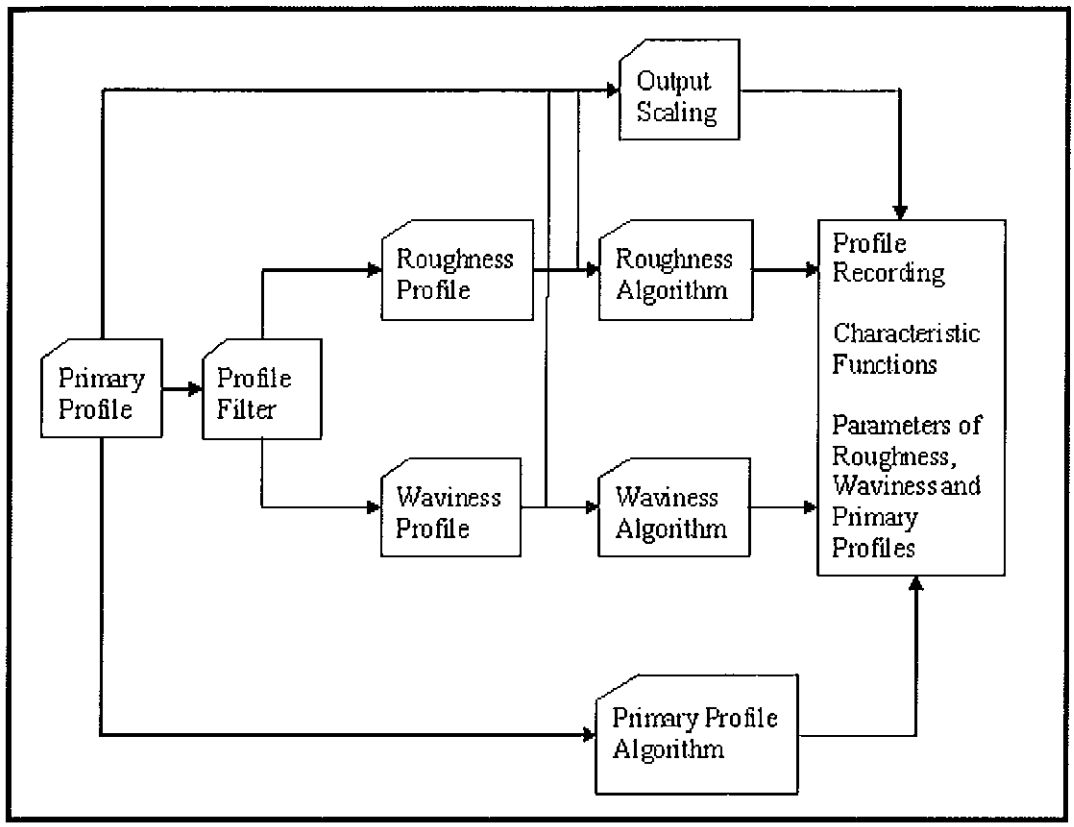

Figure 2.12. Flowchart for Surface Assessment [43]

Surface roughness is the deviation of the actual surface topography from an ideal atomically smooth and planer surface. Figure 2.13 shows the surface characteristics such as waviness and roughness [44]. Measurement of surface roughness enables one to determine the magnitude of the geometric deviations of the shape of surface patterns and of their distribution, and it can be used to predict how the contact surface will change as the height of the asperities changes [20]. In the manufacturing industry, surface roughness must be within certain limits. Also, surface roughness is an important factor determining the adhesion strength of the coatings to the surface [10].

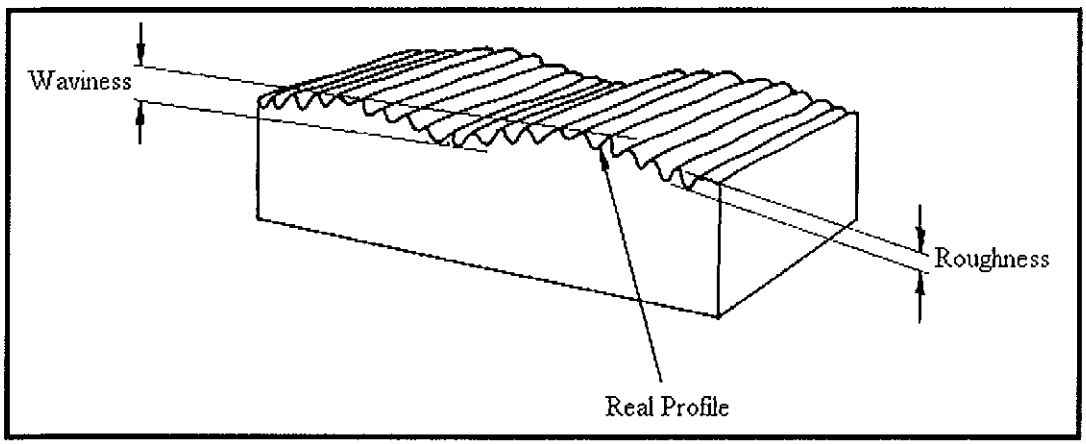

Figure 2.13. Surface Characteristics – Waviness and Roughness, Adapted from [44]

Typical roughness measurement techniques include stylus profilers, scanning probe microscopes, confocal microscopes and non-contact optical profilers.

2.4.4.2 Surface Roughness Measurement

Inspection and assessment of surface roughness can be carried out by means of different measurement techniques. Current techniques for surface roughness measurements can be classified into the following types:

i. Direct measurement methods

Direct methods assess surface finish by means of stylus type devices. Measurements are obtained using a stylus drawn along the surface to be measured: the stylus motion perpendicular to the surface is registered. This registered profile is then used to calculate the roughness parameters. Stylus type profilers are widely used for surface roughness measurement. However, it has disadvantages such as low lateral resolution due to the tip geometry and may cause surface damage due to high forces exerted on the surface.

ii. Comparison based techniques

Comparison techniques use specimens of surface roughness produced by the same process, material and machining parameters to the surface to be compared. Visual and tactile senses are used to compare a specimen with a surface of known surface

finish. Because of the subjective judgment involved, this method is useful for surface roughness; R_q is larger than 1.6 micron.

iii. Non-contact methods

The studies of non-contact techniques for the assessment of surface roughness have been reported in many literatures. Roberts and Briggs [45] have used several techniques such as the acoustic emission and incident X-ray scattering for the characterisation of surface roughness and sub-surface damage. Bilgen and Rose [46] theoretically analysed and discussed the problem of the signal noise of back scattering generated by rough surface using modelled techniques. Hilton [47] used two orthogonally polarised laser beams to produce two independent speckle patterns that are imaged and auto-correlated to deduce the roughness of the surface being illuminated.

Optical techniques for surface roughness measurements are generally based on the light scattering measurement method [48-50]. In this method, the surface roughness height information is obtained from the average intensity scattered in the defined direction, while the autocorrelation function of surface height is determined from the average intensity scattered away from the defined direction. The general upper limit of the measurement is less than 2μm. However a roughness up to 5μm has been successfully measured [51].

Another optical method for roughness measurements is the speckle pattern contrast measuring method [52, 53]. In this method, the test surface is normally illuminated by a collimated laser beam. The surface roughness can be obtained from the average contrast of the resulting speckle pattern. This method is only applicable for very smooth surfaces with roughness less than 0.3μm and the test pieces are mainly transparent plates and glass.

The speckle pattern correlation method has also been developed for surface roughness measurement [54, 55]. In this method, by altering the illuminating angle of an unexpanded laser beam on the surface, two speckle patterns are recorded on the same film. The fringes are observed by placing the developed film in a converging laser beam. The surface roughness is determined subsequently from the contrast of

the fringes. This method is applicable to various surfaces with roughness values in the range of 1-30μm.

Léger *et al* [54, 55] describe a theory and method for the measurement of the roughness of metallic surfaces by angular speckle decorrelation. They compared the measured fringe visibility with their theory for three metallic surfaces of known roughness, and they concluded that the method could easily determine the roughness and that the method seemed to be independent of the material being measured. Hertwig [56] measured the surface roughness of milled *Rugo* test surfaces by using an improved speckle contouring technique.

2.4.5 Residual Stress

A very important characteristic of a thermally sprayed coating is residual stress. Knowledge of residual stress profiles allows optimising the spraying techniques. In thermal spraying, residual stresses will be generated during the deposition process and during cooling after the deposition. In the deposition stage, quenching stress arises due to rapid cooling and solidification of the molten particles upon impact. As the solidified particles adhere to the substrate, they cannot contract freely and tensile quenching stress develops.

The residual stresses may be caused by thermal or elastic mismatch. Residual stresses originate from misfits between different regions and also they can arise from sharp thermal gradients [57]. In natural or artificial multiphase materials, residual stresses can arise from differences in thermal expansivity, yield stress, or stiffness [57]. Residual stresses will exist in a component at rest in the absence of any inertia or external force, and they are present in most surface coatings. This is a consequence of misfit strain arising during deposition and/or subsequent attainment of equilibrium.

Residual tensile stresses may influence characteristics such as the resistance of the coating to wear and fatigue crack propagating, and cause flaws in the component, such as microcracks, porosity and spalling. Residual stresses also may promote debonding and spallation of the coating, since detachment will normally allow a reduction in the stored elastic stain energy [58]. In many cases, unexpected failure

has occurred due to the presence of residual stresses which have combined with the service stresses to seriously shorten component life.

2.4.5.1 Residual Stresses Measurement Techniques

Residual stress measurement techniques include mechanical stress measurement methods, stress measurement by diffraction, measurement of transformation strains and other methods.

Mechanical stress measurement methods rely on the monitoring of changes in component distortion, either during the generation of the residual stresses or by deliberately removing material to allow the stresses to relax [57]. Mechanical methods for residual stress measurement include followings:

i. Curvature: curvature measurements are frequently used to determine the stresses within coatings and layers [59]. Curvature can be measured using contact methods (e.g. profilometry, strain gauges) or without direct contact (e.g. video, laser scanning, grids, double crystal diffraction topology), allowing curvatures down to about 10 μm to be routinely characterised. Stress field is not uniquely determined unless the technique is used incrementally [57].
ii. Hole drilling: the principle of this method is obtaining data from machining the sample for back-calculation of residual stress. It is a semi-destructive method that measures in-plane stresses. Since the undisturbed regions of a sample containing residual stresses will relax into a different shape when the locality is machined. The machining operation involves drilling a hole around which the strain is measured using either a rosette of strain gauges; moiré interferometry; laser interferometry based on a rosette of indentations; or holography. It has been used to assess the levels of stress in coatings. It is not really practical for thin (<100 μm), or for brittle coatings [57, 60].
iii. Compliance methods: the crack compliance method involves cutting a small slot to monitor the relaxation of stress in the vicinity of the crack using strain gauge interferometry [61].

Stress measurement methods by diffraction refer to the measurements using electron diffraction, laboratory X-ray diffraction, neutrons or hard X-rays. Other methods

include magnetic and electrical techniques, ultrasonic, piezospectroscopic effects, thermoelastic methods, photoelastic methods and optical techniques [57].

A method for residual stress measurement that combines optical techniques and hole drilling technique was explored during the 1980s. The objective was to replace the function of strain gauge rosettes with optical determination of surface displacements produced by localised stress relief associated with the introduction of a hole. This method eliminates some practical disadvantages of using stain gage rosettes in the hole drilling method, which include intensive surface preparation, time consuming and costs, and requirement of high accuracy of drilling a hole.

McDonach *et al.* has used moiré interferometry to relate in-plane displacements from hole drilling to residual stresses [62]. The feasibility of utilising holographic interferometry with hole drilling was also investigated [63-65]. Furthermore, shearography technique combined with surface indentation was used for residual stress determination instead of hole drilling [66].

2.4.5.2 Residual Stresses within the Thermal Sprayed Coatings

Residual stress is one of the major concerns in the production of thermal sprayed surface coatings. During the stress development, both mechanical effects and thermal effects are relevant and influential to the final state of the coatings.

In the thermal spraying system (i.e. flame spray, plasma spray and HVOF), individual molten or semi-molten particles impinge a substrate or a pre-existing material at a speed. The effect of the mechanical impact of the particles striking a surface will cause deformations to the pre-existing material [67]. These deformations will lead to the residual stress development within the material.

In addition to the mechanical effects of impact, thermal effects such as temperature effects and coefficient of thermal expansion are also very relevant to the stress development. Temperature effects include the influences from both local and global temperature changes. During the thermal spraying process, each particle is heated in the combustion chamber of the spray gun, and is projected towards a receiving substrate. On impacting the substrate, the particles deform into lamella that cool down to their melting point and solidify. The deposition temperature at the substrate

(about 450°C) is much lower than the fusing temperature of the SUPERJET process, which is about 1000°C [12]. Therefore, the temperature decrease that the particles experienced is enormous. This leads to the formation of quenching stresses in the individual lamella. The introduction of microcracks in the deposit material or debonding from the substrate will abate these stresses.

2.4.5.3 Defect in Surface Coatings Caused by Residual Stress

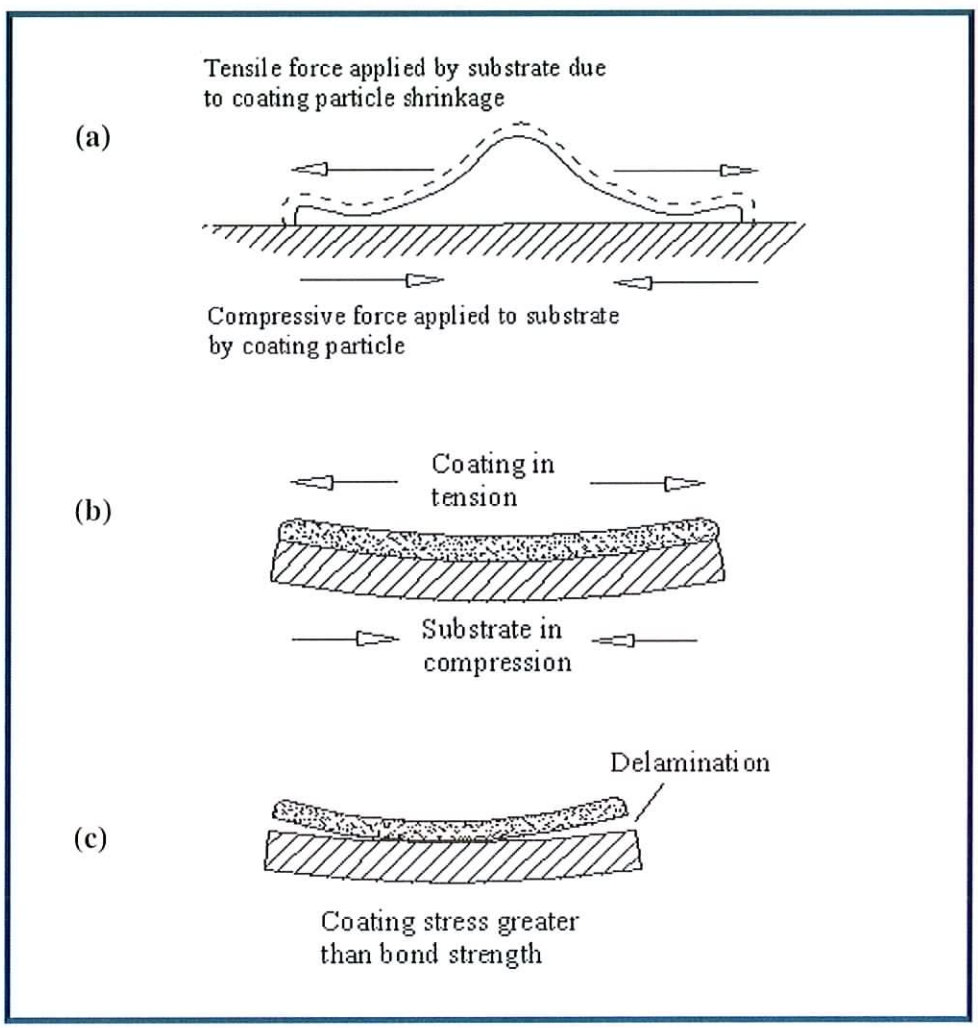

Figure 2.14. Coating Defect Caused by Residual Stresses, Adapted from [32]

When the coating material particles impact the substrate during the spraying, a tensile stress will be generated within the particle and a compressive stress will be generated within the substrate surface. The tensile stresses within the coating will be built up according to the coating thickness increase. These tensile stresses could exceed that of the bond strength or cohesive strength limit as the coating thickness

reaches some level, in this case the coating failure will occur, such as delamination and cracks, as shown in Figure 2.14 [32].

2.5 NDT OF SURFACE COATING DEFECTS

2.5.1 NDT Methods

Thermal spray deposition involves the quasi-continuous rapid deposition and solidification of molten droplets. This process results in highly defected microstructures, including porosity. It is necessary to have reliable methods for detecting the presence of the defects at the manufacturing stage and for detecting and monitoring the rate of growth of defects during the service life of a component or assembly. The main non-destructive methods include visual inspection, liquid penetrant, magnetic particle inspection, electrical testing, ultrasonic testing, radiography and optical inspection [33].

In visual inspection, examinations are carried out by the naked eye and by using a hand lens or stereoscopic microscope. Liquid penetrant inspection is used to indicate the presence of defects such as cracks, delaminations, laps and zones of surface porosity in a component. The liquid penetrant inspection system is used in the aerospace industries by both producers for the quality control of production and by users during regular maintenance and safety checks [33].

Magnetic particle inspection is a method of locating surface and sub-surface defects in ferromagnetic components. The methods are suited to the inspection of castings and forgings and components such as crankshafts, connecting rods, axles, shafts and underwater pipes.

The principle of electrical test methods is that electrical eddy currents and/or magnetic effects are induced within the material or component under test. This technique can be used for the routine in-service inspection of many components in aircraft, railway tracks, and accurate determination of thickness, including measurement of the thickness of surface coatings on metals [33].

Ultrasonic techniques are widely used for detection of internal defects in materials and detection of small surface cracks [33]. Ultrasonic testing is used for the routine inspection of aircraft and road and rail vehicles in the search for incipient fatigue cracks, and it is also used for evaluating adhesive strength of thermal sprayed coating and measuring coating thickness [68]. Radiography is very well suited for the inspection of electrical and electronic component assemblies to detect cracks, broken wires, missing or misplaced components and unsoldered connections [33].

However, the NDT methods to assess general coating quality only have limited success with sprayed coatings. Crack detection by magnetic or dye penetrant techniques often fails to detect isolated defects in the general presence of porosity. Eddy current and ultrasonic inspections are little used for sprayed coatings, which tend to be heterogeneous and give a high noise-to-signal ratio [3].

2.5.2 Optical Methods

The demand for greater quality and product reliability has created a need for better techniques of non-destructive evaluation, in particular, for online inspection. Optical interferometric methods such as speckle pattern and speckle pattern shearing interferometry possess the advantages of being full field and non-contacting. In the mechanical domain, laser interferometry techniques such as Holography, ESPI and ESPSI, developed since the beginning of the sixties, have revealed themselves as extremely useful tools providing essential information on vibration, stress and strain analysis, and NDT of structures and mechanical components [69].

These methods have advantages in comparison with other classical techniques for metrology and experimental stress analysis. They are fully non-destructive methods, in as much as there is no need for any physical contact with the specimen surface. They have a very high degree of sensitivity, allowing for the measurement of displacements with an order of magnitude of the light wavelength or even lower, and they do not require any special object surface preparation either. They also present the additional advantage of providing a global image of the displacements field over the object surface, making it easier to quickly identify stress concentrations or displacement gradients zones [69].

2.5.2.1 Electronic Speckle Pattern Interferometry (ESPI)

Generally speaking, electronic speckle pattern interferometer serves as a displacement transducer since it gives direct measurements on displacements whereas shearography serves as a strain gauge since it gives direct measurements on displacement gradients. Main feature of ESPI is that it enables real-time correlation fringes to be displayed directly upon a television monitor without recourse to any form of photographic, plate relocation etc. This allows the technique to be extended to complex problems of shape measurement and deformation analysis [70]. ESPI detects the deformations in the sub-micrometer range, of the surface of a stressed object and is therefore ideal for measuring microstrain [71].

The ESPI system could be affected by the noise that is induced by thermal currents or object drift. Also, ESPI fringes could be affected by optical noise that is caused by the presence of speckle [72]. These noises may introduce unwanted path length changes during the time of recording of each speckle pattern or in between the recordings of the pair of speckle patterns that are to be compared for relative displacement information, thus degrades the quality of the interferograms. This makes vibration isolation and stabilisation systems necessary, which restricts these techniques to their use in the laboratory environment [73]. Another problem of ESPI system is the inability to distinguish between deformation fringes and fringes caused by rigid body motion [74].

2.5.2.2 Electronic Speckle Pattern Shearing Interferometry (ESPSI)

ESPSI (shearography) measures a full-field deformation gradient and it is mainly used for defect detection of the structure. Defects in objects induce strain concentration. Shearography reveals defects with strain anomalies, and this is much easier than detecting deformation anomalies. When an object is loaded and investigated shearographically, the strength of the structure is decreased and the strain concentrations are created at the area where the defects locate. A rigid-body motion does not produce strain, thus, shearography is relative insensitive to such motion [75].

Using the phase shifting technique, experimental data processing can be strongly facilitated such as quantitative measurements with numerical calculation of phase distribution [69].

Shearography has many advantages for industrial application, due to its relative insensitivity to environmental disturbances. The main reason why the shearography systems are preferable to ESPI system is that ESPI system can only directly measure displacement, but shearography system enables direct measurements of displacement derivatives to be made. Therefore, shearography measures strain information directly. Shearography does not require an additional reference beam for generating an interferogram as in holography and speckle pattern interferometry, since the light rays are "self-referencing" owing to the shearing effect [76]. This feature makes shearography setup very easy to be carried out. Also shearography has advantages such as real time, fast inspection, full-field and usable with multi-laser diodes for illumination.

However, shearography also has limitations such as it is still sensitive to ambient noises, big rigid-body motion and thermal air currents, and it is difficult to measure a flaw located deep far from the object surface [75].

2.5.2.3 Applications of Interferometric NDT

With ESPI, measurements can be made using static or dynamic loading. Applications using static analysis include areas such as stress analysis, object contouring, NDT, and optical component testing [77]. In NDT, different means of applying stress to the object under test along with phase stepping have been employed to detect defects [77]. Static and dynamic measurements at high temperature have successfully detected debonds [78]. The advantages of high-temperature studies include the extraction of both mechanical and thermal properties and the enhancement of the detection of defects and cracks [77]. Microscopic evaluation of crack tip displacements in the application of composite material has proven to be an aid of NDT. Subsurface defects in composite material applications and debonds in honey-comb structures and overlap shear joints have been detected with ESPI [79]. ESPI also can be used to determine the shape of complicated objects [77].

Various optical methods such as holography, shearography, and moiré have been used for NDT of composite materials in recent years. Shearography is more practical than other methods in NDT. It has a simple optical setup because of its self-referencing optical system, can be used with a laser diode for illumination, and it is insensitive to slight rigid-body motions. Shearography detects defects in objects by correlating the anomalies of displacement derivatives, which is usually easier than by correlating the anomalies of displacement itself, as in holography [76].

Shearography as a laser interferometric technique used in conjunction with digital imaging processing has the potential for identifying defects in both small and large structures. Shearography has shown its applicability in the automotive and aerospace industry for NDT of composites, e.g., GLARE (metal-glass fibre laminates) panels, honeycomb structures, and glass or carbon fibre-reinforced plastics (GFRP or CFRP) [76]. Shearography has currently been used in the rubber industry routinely for evaluating tires [80].

As shearography is sensitive to displacement gradients, it is well adapted to detect defects in the structures which can lead to localised displacement gradients at the surface, such as is the case of debonds and delaminations in composite materials [69]. The technique has found a wide use in aerospace industry for non-destructive evaluation of spacecraft structures [81].

Shearography has been proved to be a practical tool in the field of NDT of composite materials in automotive and aerospace industries [16]. One of the first industrial installations of laser shearography in Europe was a fully automatic inspection system for helicopter rotor blades, and the complete rotor blades were inspected within 10 minutes on delaminations and the debonds in the composite structure [82]. Mayer *et al.* [83] have described the assessment of the quality of chemical fibre reinforced aircraft components after the production using a stationary shearography measurement unit. Other applications are shearography inspection systems for abradable seals in jet engines and portable shearography inspection systems for maintenance and repair inspection in the field [82].

Shearography was used for non-invasive inspection of large-scale structures for identifying cracks and strain anomalies. However, one of the major problems was the

existence of large rigid body motions. Maji *et al.* [84] have characterised the speckle pattern obtained from typical civil structures as a function of the illumination and imaging system. They quantified speckle decorrelation as a function of object motion and instrumentation characteristics. The obtained results were used to define the parameters of a structural inspection system based on shearography for field applications.

Hung and Shi [85] have reported an application for rapid evaluation of hermetic seals of microelectronic packages using shearographic technique. With the pressure change maintained in the package, the lid of a perfectly sealed package will remain deformed while a leaky package will not hold the deformation, which can be monitored by shearography. They also reported that this testing method could be extended to testing pharmaceutical packages and food packages.

Sirohi *et al.* [13] demonstrated that phase-shift digital shearography could be used to identify the presence of defects, having the form of localised thinning in a plate structure. They presented an idea that the thickness could be obtained by the measurement of the slope of the deflection gradient curve obtained from shearography.

Silva Gomes *et al.* [73] described an application of two laser interferometry techniques (ESPI and ESPSI) to the NDT of thermal barrier coatings. Interfacial disbond between the coating and substrate was detected.

2.5.2.4 White Light Interferometry (WLI)

Light is a form of energy which can be considered of travelling from one place to another in the form of electromagnetic sinusoidal waves. The wave length λ determines the colour, and the amplitude a determines the intensity of the light [86]. White light is a combination of all the colours of the visible spectrum (red, orange, yellow, green, blue and violet) and each colour band consists of a group of similar wavelengths. White light is not suitable for length measurement by interferometry since it is a combination of light of all colours and is a combination of all the wavelengths of the visible spectrum [86]. However, WLI is a suitable method for height profile measurement of objects.

The important advantage of WLI is that it can be used for measurement of objects with rough surface even in the case of speckle imaging. Also, it has advantages such as high resolution and speed, non-contact and able to give complete profiling of surface.

Chapter 3 – Theory

3.1 OPTICAL TECHNIQUE

3.1.1 Laser Light

Laser is the acronym of "Light Amplifier by the Stimulate Emission of Radiation". Visible electromagnetic radiation has a frequency of ~10^{15} Hz, and the radiation produced by a laser approximates quite close to a plane wavefront, the divergence of a laser beam is typically ~10^{-3} radians [70].

The output of a laser is in the form of an approximately plane wavefront whose diameter is of the order of millimetres. To illuminate an object larger than this, the beam must be expanded by a lens. The shorter the focal length the greater the angle subtended by the expanding beam at the focus, and the hence the greater the expansion of the beam at a given distance [70].

A plane wave front covering an area considerably larger than the diameter of the laser beam is frequently required in speckle and holographic interferometry. This can be done by placing a second lens of focal length f_1 so that its focus coincides with that of the first lens of focal length f_2. The output beam is then a plane wavefront; the ratio of the diameters of input to output beam is given by f_2/f_1 [70].

3.1.2 Interference

Any pair of wavefronts of the same frequency which are added together will give rise to interference. To obtain interference effects, the light must be monochromatic (single frequency) or very nearly so, this is why interference experiments are easier to perform with laser than with conventional light sources [70].

The distance L between equivalent points in the intensity variation is given by

$$L = \lambda / 2\ Sin\theta \qquad \text{Equation 3.1}$$

This intensity variation is known as an interference fringe pattern, the two plane wavefronts of intensities I_1 and I_2 are superimposed, the intensity varies sinusoidally

between a maximum value $[I_1 + I_2 + 2(I_1I_2)^{1/2}]$ and a minimum value $[I_1 + I_2 - 2(I_1I_2)^{1/2}]$. It will exist as long as the beams overlap. The fringe pattern is in the form of a series of planes of uniform intensity which are parallel to the plane that bisects the angle between the two beams and is perpendicular to the plane defined by the two propagation vectors [70].

3.2 SPECKLE METROLOGY

3.2.1 Coherent Light

Coherence is the property of a light beam that allows the formation of interference fringes or other manifestations of interference [87]. A beam that produces highly contrasty interference fringes is said to be highly coherent, and a beam that produces moderately contrasty interference fringes is said to be partially coherent. In order to produce high-quality interference fringes in any interference experiment, the light is required to be completely coherent. When the light is incoherent, it is not possible to detect interference effects. However, in general, except certain laser sources, the light from most sources is incoherent or partially coherent. Laser light emits a beam that is almost completely coherent in space and time.

A laser beam will have the plane wavefront extends to infinity both in time and in space and it has a single frequency which does not change, approximate to a sine wave of fixed frequency over a distance, the distance is known as the Coherence Length of the laser [70].

Coherence has two phenomena named as spatial coherence and temporal coherence [88]. Spatial (transverse) coherence is the coherence of a wave field at two points in space. Temporal (longitudinal) coherence is the coherence between two wave fields at one point in space.

3.2.2 Speckle Effect

When a light beam strikes a smooth surface, such as a mirror, glass or polished surface, all rays reflect in the same way. This is referred to as regular reflection. When light strikes an optically rough surface, which the height variation of the

surface is of the order of, or greater than the wavelength λ of the illuminating light [70], diffuse reflection occurs, as shown in Figure 3.1. While each ray of light obeys the law of reflection, they all reflect in different directions. These scattered waves will interfere and form an interference pattern consisting of dark and bright spots or speckles which are randomly distributed in space, these granular appearance of such a surface is known as the speckle effect [70]. Speckle phenomenon is a distinctive tool of measuring displacements and other parameters like surface roughness and shape [77].

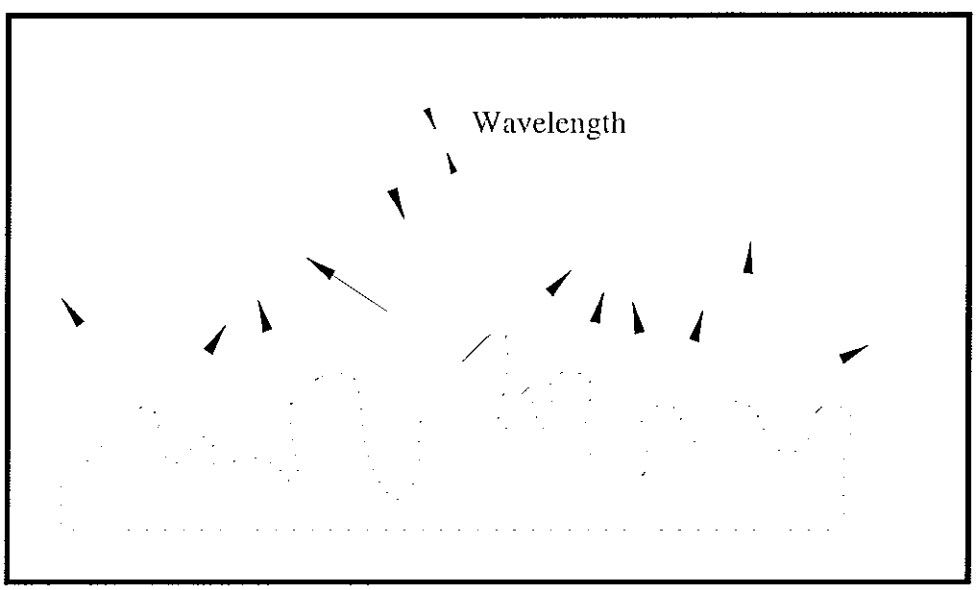

Figure 3.1. Light Scattering from a Rough Surface

3.2.3 Speckle Pattern

The self-interference of a large number of random coherent waves scattered from a rough object surface or propagated through a medium of random refractive index fluctuations results in a granular structure known as speckle pattern [77]. The speckle pattern arises because the object is locally very rough and causes a random phase to be superimposed on the amplitude distribution of the coherent wave. The speckle pattern is a sort of diffraction pattern of a random diffracting screen and is thus a random distribution of intensity [87]. Speckle pattern carries information corresponding to the surface topography of the test object [69]. Each speckle in the image plane corresponds to a point on the object surface. If that point is displaced in

the same plane, the speckle will be displaced in the imaging plane by a corresponding amount.

Speckle which is formed on the retina and moves when the eye moves is called subjective speckle [87]. From the Figure3.2, it can be seen that when laser light illuminated on an area of cross section D, the objective speckle pattern is observed on a screen S at a distance Z from the scattering surface. The period of this pattern is a measure of the smallest objective speckle size σ_0 which is

$$\sigma_0 = \frac{\lambda z}{D} \qquad \text{Equation 3.2}$$

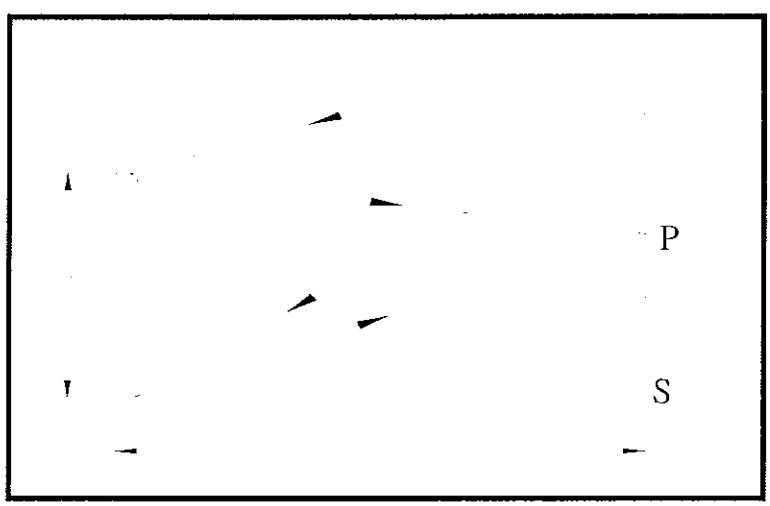

Figure 3.2. Objective Speckle Formation

Speckle that can be projected onto a screen is called objective speckle [87], as depicted in Figure 3.3. When the scattering surface is imaged on to a screen by means of a lens L, the calculation of the size of the resulting subjective speckle is analogous to the calculation of the objective speckle size. The subjective speckle size σ_s therefore is given as

$$\sigma_s = \frac{\lambda b}{D} \qquad \text{Equation 3.3}$$

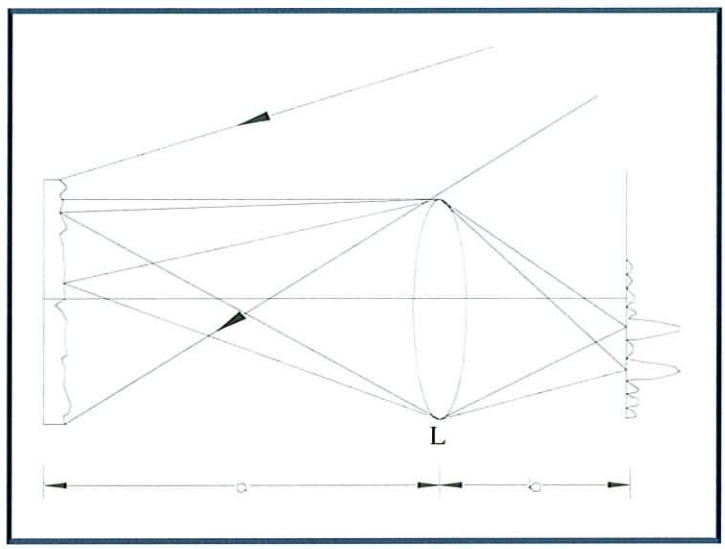

Figure 3.3. Subjective Speckle Formation

3.3 WHITE LIGHT INTERFEROMETRY (WLI)

White light interferometer is in the principle of Michelson interferometer. The only variation from it is the measured object is placed in one arm of the Michelson interferometer instead of one of the mirrors, as shown in Figure 3.4.

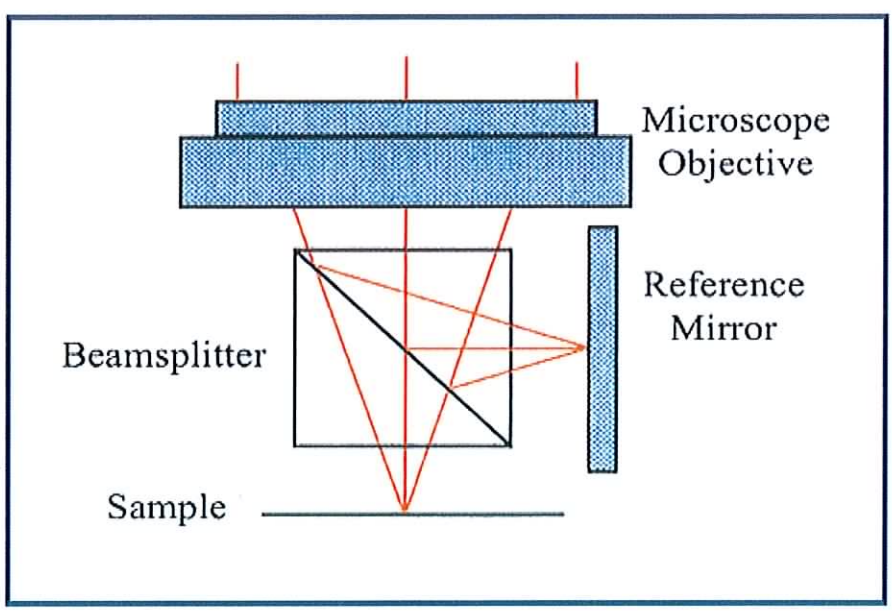

Figure 3.4. Schematic Diagram of the WLI Profiler

A light beam of short coherence length (typically 1μm) is split into two parts by a beamsplitter so as to illuminate both the surface and a reference mirror. On recombination of the beams at the beamsplitter, interference effects are obtained only if the optical path difference in the interferometer is less than the coherence length. As the mirror is translated parallel to itself, the surface is imaged by a CCD camera and the images are captured and passed to a personal computer. As the path length of the reference beam changes, different regions of the objects surface meet the coherence condition and the light intensity at the corresponding CCD pixels is modulated. By noting where the reference mirror is when each pixel is modulated a profile of the surface can be progressively built up.

3.4 ESPI

This research work concerns two laser interferometry methods, ESPI, and ESPSI. Therefore, an introduction and discussion of both techniques is necessary.

ESPI is a speckle interferometry technique that is based on the coherent addition of a speckle field scattered by an object and a reference field [89]. A speckle pattern is formed by illuminating the surface of the object to be tested with laser beam, and this speckle pattern is allowed to interfere with the reference wave. When the object has been deformed or displaced, the resultant speckle pattern changes owing to the change in path difference between the wave front from the surface and the reference wave. The second resultant speckle pattern is transferred to the computer and subtracted or added from the stored pattern and the result rectified. A CCD camera imaged this pattern and then transferred it to a frame grabber on board of a host computer, saved in memory, and displayed on a monitor [71, 90, 91]. The resulting interferogram is displayed on the monitor as a pattern of dark and bright fringes, called correlation fringes.

As the object deforms, the frames are continuously grabbed and added to or subtracted from the reference frame. Therefore, it is possible to observe the fringes form and change as the deformation continues. These fringes represent the movement of the surface during deformation. The spacing between neighbouring fringes is inversely proportional to the displacement and the fringes are aligned perpendicular to the direction of the displacement [71].

The intensity of the beam before and after the deformation can be represented as followings [70]:

$$I_{TB} = I_o + I_r + 2\sqrt{I_o I_r}\cos\psi \qquad \text{Equation 3.4}$$

$$I_{TA} = I_o + I_r + 2\sqrt{I_o I_r}\cos(\psi + \Delta\phi) \qquad \text{Equation 3.5}$$

Where I_o and I_r are the average intensities of the object and the reference beam respectively, ψ is the phase difference between the two beams. $\Delta\phi$ is the phase change due to the displacement on the test object surface.

The subtraction between Equation 3.4 and 3.5 is given by

$$I_{TA} - I_{TB} = 2\sqrt{I_o I_r}[\cos(\psi + \Delta\phi) - \cos\psi] \qquad \text{Equation 3.6}$$

When $\Delta\phi = 2n\pi$, where n is an integer, I_{TA} and I_{TB} have maximum correlation and the resultant intensity is zero. When $\Delta\phi = (2n+1)\pi$, the minimum correlation occurs and the resultant intensity is maximum. Therefore, Equation 3.6 represents a fringe pattern in which the bright fringes represent areas where a phase-change of $2n\pi$ occurred between the fields before and after deformation.

Optimum fringe quality is obtained when the reference beam brightness is set at a value only slightly higher than the average speckle brightness and the speckle resolved by the CCD camera [77].

ESPI can be used to measure both in-plane and out-of-plane displacements. The distinction between these two arrangements is made by a simple change in the optical set-up [92]. Single-beam illumination ESPI is used to measure of out-of-plane displacement while dual-beam illumination is sensitive to the in-plane displacement component [78].

The basic arrangement that gives fringes which are sensitive to in-plane displacement is shown in Figure 3.5 [70]. The in-plane ESPI system uses two independent speckle patterns as each of the two illuminating beams generates its own speckle pattern. The in-plane ESPI technique measures only the displacement along a vector direction that

lies normal to the line of sight of the system and is in the plane of the two beams. Therefore, it is generally used for surface strain measurement.

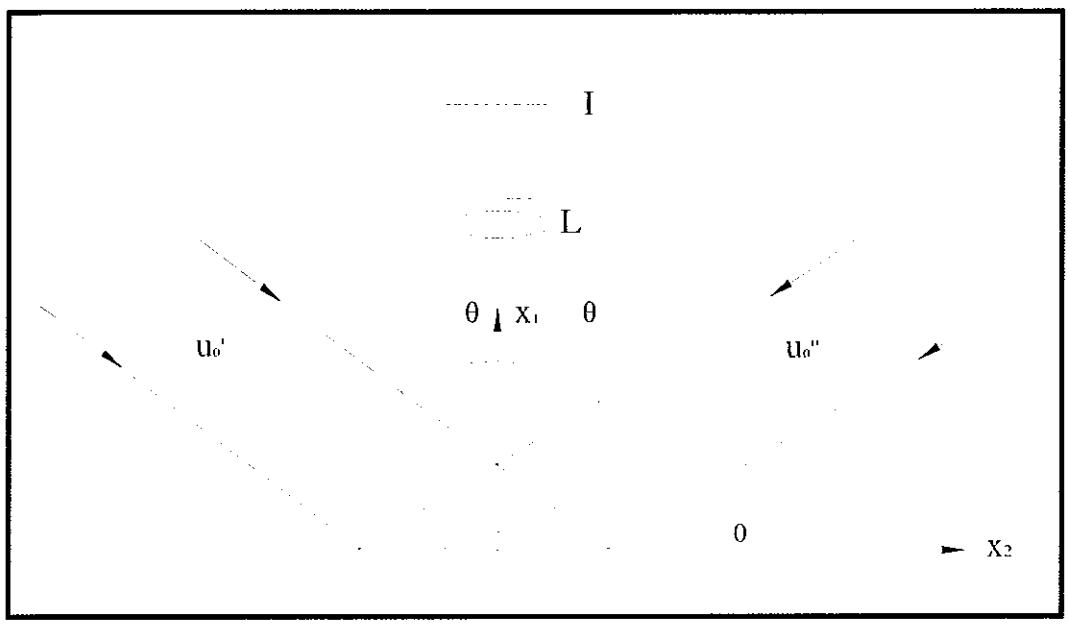

Figure 3.5. In-Plane Displacement Arrangement of ESPI

$U_0^{'}$ and $U_0^{''}$ are the two plane wavefronts that inclined at equal and opposite angles θ.

The centre of the viewing lens aperture lies on the x_1-axis. When an element is displaced by a distance d (d_1, d_2, d_3) the relative phase change between the two beams is given by

$$\Delta\phi = \frac{4\pi}{\lambda} d_1 \sin\theta \qquad \text{Equation 3.7}$$

Where θ is the angle of the illumination beam to the x_1-axis surface-normal, λ is the wavelength of the laser. This form of interferometer therefore allows in-plane displacement distributions to be observed independently in the presence of out-of-plane displacement.

In the out-of-plane system, the object is illuminated by the object beam at an angle and the image is formed by the lens at image screen. A diverging spherical reference wave is added to the image by the beamsplitter. Figure 3.6 shows the arrangement of an out-of-plane ESPI.

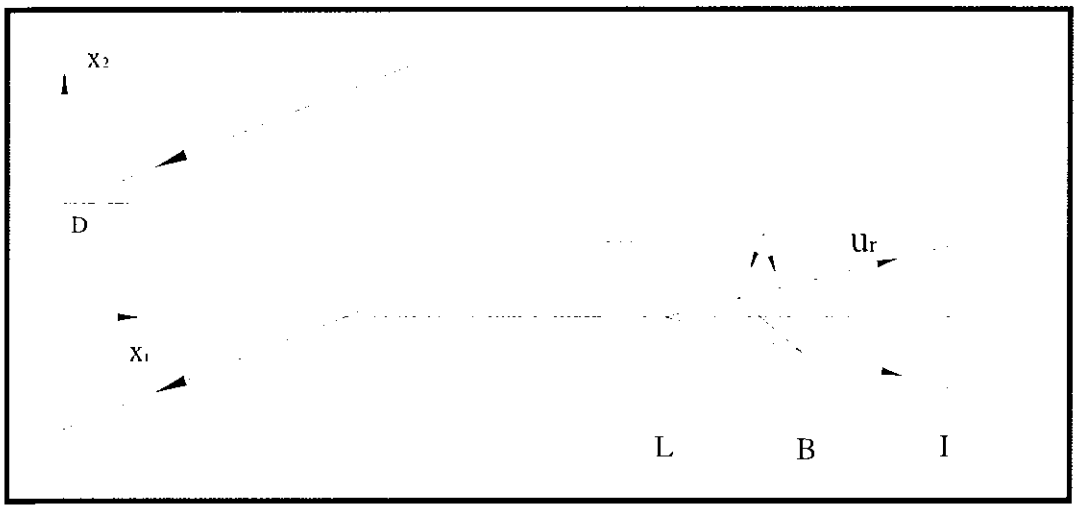

Figure 3.6. Out-of-Plane Displacement Arrangement of ESPI

The general form of fringe pattern of in-plane as well as out-of-plane displacement is

$$\Delta\phi = \frac{2\pi}{\lambda}(n_0 - n_s)\cdot d \qquad \text{Equation 3.8}$$

Where

n_0 =illumination direction

n_s =viewing direction

The optical head of the ESPI system can be configured in several different ways depending on whether the problem at hand concerns the measurement of displacement components (interferometry) or spatial derivatives of displacement components (shearography) [81].

3.5 ESPSI

In ESPSI, the interferometric superposition of the two slightly sheared images creates an interferogram, called a speckle interferogram. Therefore, this technique is also called shearography. It is a coherent-optical measuring and test method that is similar to holography interferometry.

In normal speckle interferometers, the object surface is compared with a reference beam from a mirror or a scattered beam from a diffuse object. While in speckle shearing interferometers, the object surface is compared with a speckle reference beam arising from the same object [77]. ESPSI technique compares the information before and after loading by means of a digital technique, and presents the results directly on a monitor. In this technique, wet processing and optical reconstruction are not required.

In the shearographic process, interference occurs between two speckle patterns corresponding to a pair of images of the same surface, displaced across a given shear direction. The obtained interference pattern represents the out-of-plane displacement gradient across the direction of shear, its sensitivity being conditioned by the magnitude of the shear displacement. [69]

Conventional Shearography uses a speckle-shearing camera, in which a thin glass wedge covers one half of the lens [76]. The object under study is illuminated by laser light, and a shearing device produces two sheared images that interfere with each other. When the object is deformed, the speckle pattern changes. High-resolution film is exposed before and after the object is deformed. The two speckle patterns interfere to produce a fringe pattern that depicts the surface gradient of the deformed object. The fringe pattern is only visible using a high-pass Fourier filtering technique [76].

The difference between shearography and holography can be included as that holography measures the out-of-plane deformation directly, but shearography measures the first derivative of the deformation in the shearing direction directly. The deformation can be observed in holography is not only at the position of the defect but over the whole surface of the object as well, but in shearography

interferometry, only the position of the defect appears as a fringe pattern, generally owing to the nonlinear deformation gradient with respect to strain concentration, as shown in Figure 3.7. Thus, in the shearogram the fringes appear only at the position of the defect caused by the basic deformations, and they can be detected easily and unambiguously [76].

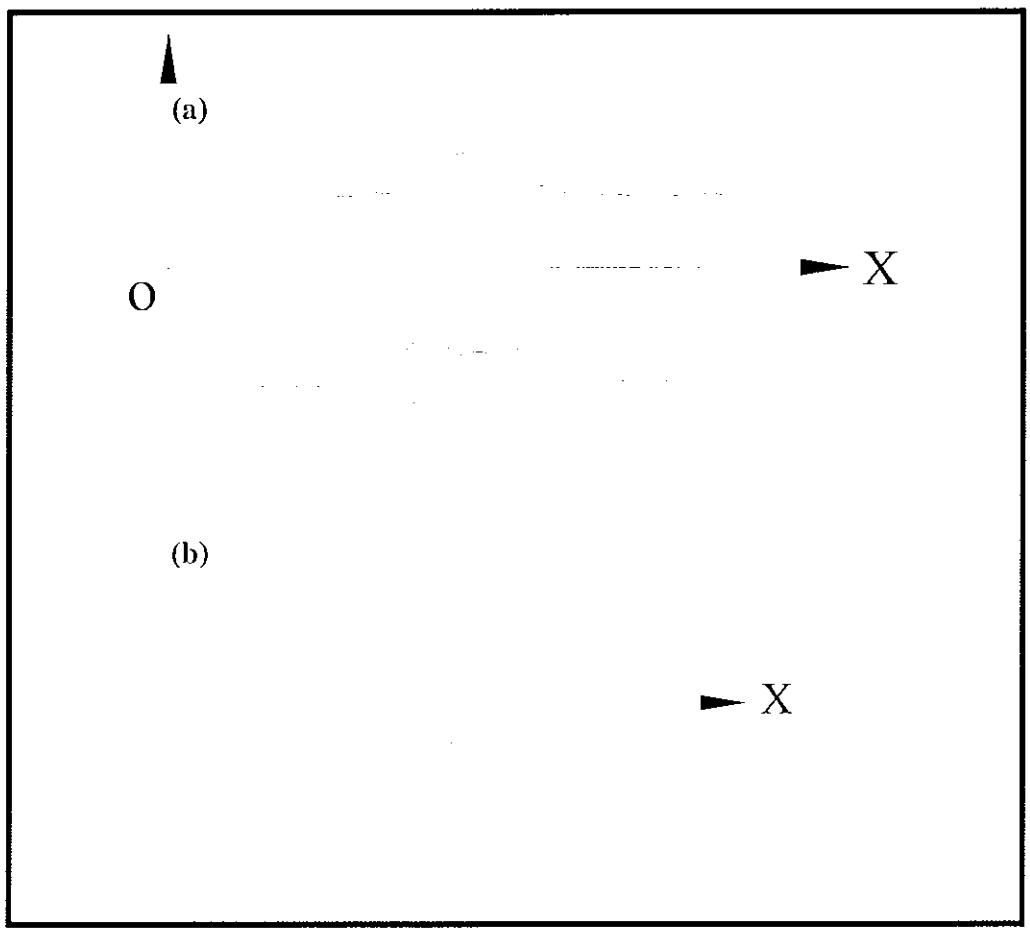

Figure 3.7. Difference between Holographic and Shearographic Testing of Material: (a) Defect Detected by Holographic Method; (b) Defect Detected by Shearographic Method.

3.5.1 Theory of ESPSI

Shearography measures the relative deformation between two points separated by a defined shearing amount. The reading of the measurement shows the mathematical difference ratio of the deformation or the gradient of the deformation. The sensitivity of the shearography for defect identification can be adjusted by the selection of the

shearing amount. Usually the sensitivity increases with a higher amount of shearing. For a qualitative analysis such as NDT, the shearing amount can be relatively large, e.g., 10% to 15% of the measurement range. The shearing direction determines the direction of the gradient, and different results are available in different shearing directions. When measuring the deformation gradient created by defects, the sensitivity of shearography depends on the amount of the shearing as well as its direction [76].

The components of shearography system include laser, shearing device, frame grabber and CCD camera. The laser for shearography usually has a coherence length with several decades of millimeters or even a few millimeters. A simple laser diode doesn't have a long coherent length, but its size is very small, and as much lends itself particularly well to being added into a portable shearographic sensor.

The shearing device can be any device which is able to bring light scattered from two points on an object surface into one point on the image plane, e. g. optical glass wedge, a bi-angle prism, a double-refractive prism and a modified Michelson Interferometer (Figure 4.25), etc. Frame grabber delivers a corresponding library that is beneficial to a software development of shearography. For CCD camera, the spatial resolution (pixel number) and whether it is suitable for a commercial frame grabber are two specifications for CCD camera selections [75].

When two light waves interfere, the following equations [70] relate their relative phase ϕ at a location to their relative geometrical path length L.

$$\phi = \frac{2\pi}{\lambda} nL - \beta, \qquad \text{Equation 3.9}$$

Where λ is the wavelength of the laser light, n is the refractive index of the media through which the laser light is transmitted, and β is a constant phase. The change in the relative phase $\Delta(=\delta\phi)$ or phase change, which manifests as visible fringes, can be effected by an incremental change in any one of the three parameters λ, n, and L. Thus,

$$\Delta = \frac{\partial\phi}{\partial\lambda}\delta\lambda + \frac{\partial\phi}{\partial n}\delta n + \frac{\partial\phi}{\partial L}\delta L = -\frac{2\pi Ln}{\lambda^2}\delta\lambda + \frac{2\pi L}{\lambda}\delta n + \frac{2\pi n}{\lambda}\delta L \qquad \text{Equation 3.10}$$

Where $\delta\lambda$, δn, and δL denote, respectively, the incremental change in wavelength, in refractive index, and in relative geometrical path length of the interfering waves.

If the same wavelength is used and the test environment is still air (n = 1), only the δL term in Equation 3.10 is nonzero, resulting in the following equation for phase change:

$$\Delta = \frac{2\pi}{\lambda}(A\delta u + B\delta v + C\delta w), \qquad \text{Equation 3.11}$$

Where u, v, and w are the displacement components of point P (x, y, z). δu, δv, and δw are the displacement components of the neighboring point Q ($x+\Delta x$, y, $z+\Delta z$) relative to point P on the test surface; and A, B, and C are sensitivity factors that are related to the optical arrangement.

For small image shearing δx, the displacement terms in Equation 3.11 can be expressed in terms of partial derivatives:

$$\Delta = \frac{2\pi}{\lambda}(A\frac{\partial u}{\partial x} + B\frac{\partial v}{\partial x} + C\frac{\partial w}{\partial x})\delta x. \qquad \text{Equation 3.12}$$

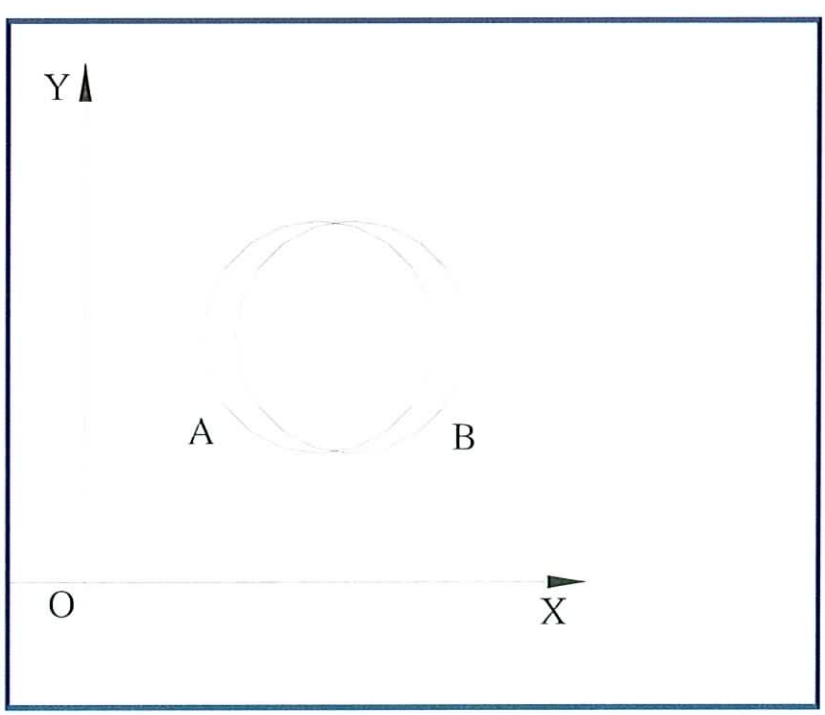

Figure 3.8. Two Wavefronts Sheared in the X Direction

The relationship between the mechanics of components and the relative phase change Δ is:

When the derivation of object plane is small and the amount of the shearing is δ_x, as shown in Figure 3.8, then the relative displacement approximates the derivatives of displacements. Thus in the x-direction:

$$\Delta_x = (A\frac{\partial u}{\partial x} + B\frac{\partial v}{\partial x} + C\frac{\partial w}{\partial x})\delta x \quad \text{, or} \quad \Delta_x = (K_s e_x \frac{\partial u}{\partial x} + K_s e_y \frac{\partial v}{\partial x} + K_s e_z \frac{\partial w}{\partial x})\delta x$$

Equation 3.13

There is an analogous result for a shearing in the y-direction:

$$\Delta_y = (A\frac{\partial u}{\partial y} + B\frac{\partial v}{\partial y} + C\frac{\partial w}{\partial y})\delta y \quad \text{, or} \quad \Delta_y = (K_s e_x \frac{\partial u}{\partial y} + K_s e_y \frac{\partial v}{\partial y} + K_s e_z \frac{\partial w}{\partial y})\delta y$$

Equation 3.14

Which A, B and C are the sensitive coefficients.

Where K_s is the sensitivity vector at the surface point, e_x, e_y and e_z are the unity vectors the in the x-, y- and z-directions.

These equations describe the whole-field interference fringes of a shearogram as lines of the first derivative of deformation instead of constant lines of deformations as in a hologram. For this reason the shearogram depicts the strain concentrations directly and it is therefore suitable for NDT.

3.6 ESPSI FOR DEFECT DETECTION

A successful application of ESPSI for NDT of a defect depends on: the depth and type of the defects, type of materials, shearing amount and direction, manner of loading and the laser illumination [75].

Assuming that a specimen has a delamination, a sufficient loading (e.g. by a thermal or a vacuum loading), will cause buckling on the sample surface. According to elasticity theory, the maximal deflection appears at the center of the delamination [75].

Holography detects a flaw by looking for displacement anomalies induced by the defect, and the anomaly area looks like a circular fringe pattern. Shearography detects a flaw by looking for strain anomalies induced by the defect and the anomaly area looks like a butterfly pattern [75].

3.7 FRINGE ANALYSIS

3.7.1 Displacement of a Point of the Object per Fringe

This intensity variation is known as an interference fringe pattern, the fringe pattern is in the form of a series of planes of uniform intensity which are parallel to the plane that bisects the angle between the two beams and is perpendicular to the plane defined by the two propagation vectors [70].

When the surface is displaced the phase of the light scattered from each point on the surface to each point in the viewing plane is altered. The phase ψ of the light scattered from a given point in the undisplaced object to a given point in the viewing plane is related to the phase ψ' of the light scattered from the same point in the displaced object to the same point in the viewing plane by [70]:

$$\psi' = \psi + (2\pi/\lambda) * (n_o\text{-}n_s) * d \qquad \text{Equation 3.15}$$

Where d is the displacement of the object point and n_o and n_s are the directions of illumination and viewing of that point.

$$\phi_p = (2\pi / \lambda)[(n_o - n_s) \cdot d_p] \qquad \text{Equation 3.16}$$

Where ϕ_p is the phase change associated with the displacement of the pth scattering point.

If the value of ϕ_p is constant across the resolution element, the value of I at a point is given by

$$I = 2n_0^2 n(1 + \cos\phi_p) + \text{cross-terms} \qquad \text{Equation 3.17}$$

If Equation 3.17 is averaged over many speckles along a line in the viewing plane for which ϕ_p is constant both across the resolution elements and for all the points along the line, then the mean value of I is given by

$$\langle I \rangle = 2u_0^2 n(1+\cos\phi_p) \qquad \text{Equation 3.18}$$

The mean value of intensity has a maximum value of $4u_0^2 n$ when $\phi_p = 2n\pi$ and a minimum value of zero when $\phi_p = (2n+1)\pi$. The value of ϕ_p across the resolution element can be seen to be constant only when the following conditions are satisfied:

i. The illumination is a plane wavefront so that n_0 is constant;

ii. The viewing plane is in the focal plane of the lens so that n_s is constant;

iii. The body undergoes a rigid body translation so the d is constant.

3.8 PARAMETERS OF SURFACE ROUGHNESS

Many parameters have been used for the description of surface roughness, and they can be categorised as statistical and extreme-value parameters.

i. Statistical parameters refer to those giving average behaviour of the surface height. For example, average roughness R_a and the root mean square roughness R_q;

ii. Extreme-value parameters refer to those giving maximum values of surface profile. For example, the maximum peak height R_p, the maximum valley height R_v and the maximum peak to valley height R_{max}.

A few parameters that used in the project to calculate the coating surface roughness are discussed at the following section.

3.8.1 R_a – Average Roughness

Among these parameters, the average roughness value R_a is the most effective and commonly adopted one in general engineering practice, since it gives a good general description of the height variations in the surface. Figure 3.9 shows the arithmetical mean deviation of the profile R_a. The earliest analogue roughness measuring

instruments measured only R_a by drawing a stylus continuously back and forth over a surface and integrating to find the average electronically.

The average roughness is the area between the roughness profile and its mean line, or the integral of the absolute value of the roughness profile height over the evaluation length [44]:

$$R_a = \frac{1}{l}\int_0^l |r(x)|dx \qquad \text{Equation 3.19}$$

or approximately

$$R_a \approx \frac{1}{n}\sum_{i=1}^{n}|Y_i| \qquad \text{Equation 3.20}$$

Where l is the sampling length;

y is the profile departure; n is the number of the profile departures.

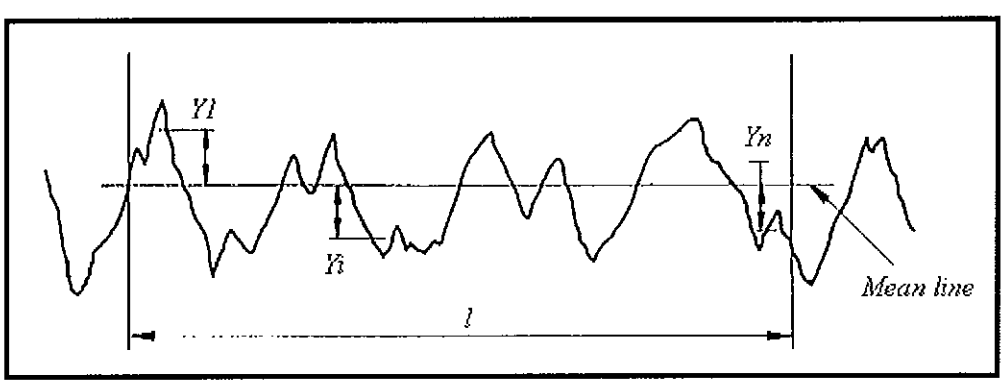

Figure 3.9. Arithmetical Mean Deviation of the Profile (R_a), Adapted from [44]

3.8.2 R_q – Root-Mean-Square Roughness

The root-mean-square (rms) average roughness of a surface is calculated from another integral of the roughness profile [44]:

$$R_q = \sqrt{\frac{1}{l}\int_0^l r^2(x)dx} \qquad \text{Equation 3.21}$$

For a pure sine wave of any wavelength and amplitude R_q is proportional to R_a. Old instruments made use of this approximation by calculating R_a with analogue electronics and then multiplying by 1.11 to report R_q. R_q has now been almost completely superseded by R_a in metal machining specifications. However R_q still has value in optical applications where it is more directly related to the optical quality of a surface.

3.8.3 R_t, R_p, and R_v

The peak roughness R_p is the height of the highest peak in the roughness profile over the evaluation length. Similarly, R_v is the depth of the deepest valley in the roughness profile over the evaluation length. The total roughness, R_t, is the sum of these two, or the vertical distance from the deepest valley to the highest peak, as shown in Figure 3.10 [44].

$$R_v = \left|\min[r(x)]\right|, \quad 0 < x < l \qquad \text{Equation 3.22}$$

$$R_p = \left|\max[r(x)]\right|, \quad 0 < x < l \qquad \text{Equation 3.23}$$

$$R_t = R_p + R_v \qquad \text{Equation 3.24}$$

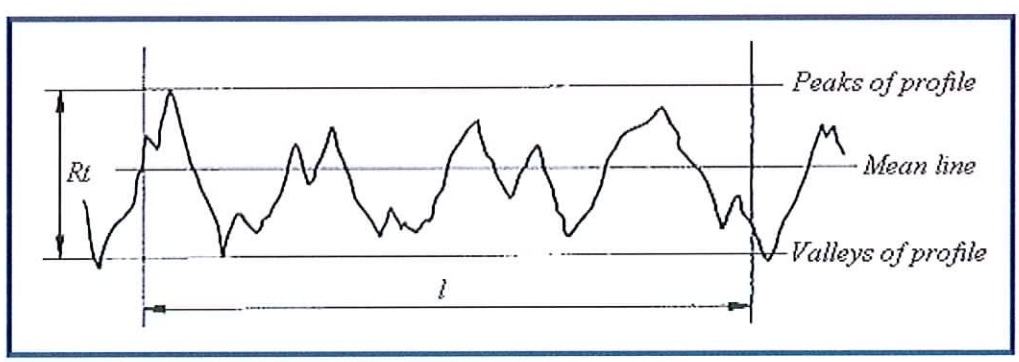

Figure 3.10. Maximum Height of the Profile (R_t), Adapted from [44]

3.9 QUENCHING STRESS

When a molten droplet of coating material impinges on a substrate during the spraying deposition, it tends to spread into a pancake-like splat, which will quickly solidify and cool to the substrate temperature. Due to the coefficient of thermal expansion of the coating material, a contraction of the splat will be followed as it cools. During this cooling, the substrate has a trend to against this thermal contraction of the splat, thus a stress is generated in the splat. The state of the stress in the coating is tensile and its magnitude depends on the thermal expansion coefficient of the sprayed material and the final temperature of the splat will reach to match the substrate temperature. Since splats are typically a few microns in thickness, it can always be assumed that they are on a massive substrate and the misfit strain associated with the contraction is entirely accommodated within the splat. The stress developed in this way is termed as quenching stress, or known as the intrinsic stress [93]. The magnitude of the quenching stress is independent of the substrate material, though it has shown a dependence on the substrate temperature. The quenching stress relaxation mechanisms are shown in Figure 3.11.

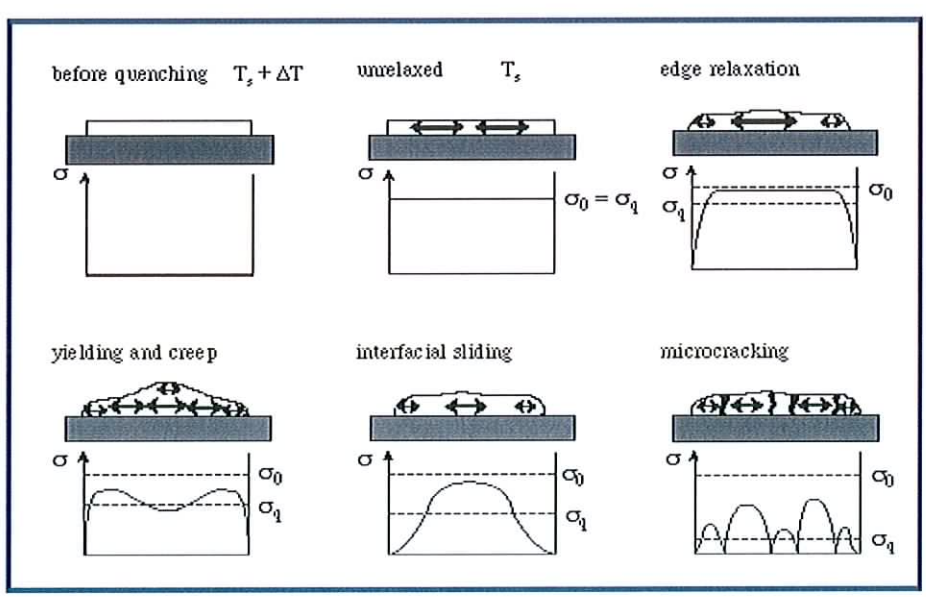

Figure 3.11. Quenching Stress Relaxation Mechanisms [94]

High tensile quenching stresses will be generated in the individual lamella as the lamellae solidify, contract and are constrained by each other and the substrate. According to the literature [95], 5 to 15 lamellae may exist in a single pass of spray

depending on initial powder particle size. The quenching stress can be estimated by the expression of:

$$\sigma_q = E_c \varepsilon \qquad \text{Equation 3.25}$$

and the thermal strain is given by

$$\varepsilon = \frac{\Delta L}{L_0} = \alpha_c \Delta T \qquad \text{Equation 3.26}$$

therefore,

$$\sigma_q = \alpha_c (T_L - T_S) E_c \qquad \text{Equation 3.27}$$

where,

σ_q = quenching stress

E_c = elastic modulus of the coating material

ε = thermal strain

ΔL = change in length due to the increase/decrease in temperature

L_0 = original length

α_c = coefficient of thermal expansion of the coating

ΔT = change in temperature

T_L = the temperature of the individual lamella at impact with substrate

T_S = the temperature of the substrate

Cooling stresses will be generated when the deposition process is ceased or interrupted. These stresses are mainly due to the mismatch of the thermal expansion coefficients of the substrate (α_s) and the coating (α_c). The state of the cooling stress

in the coating depends on the relative comparison between these expansion coefficients. When $\alpha_s < \alpha_c$, the contracts in the coating is greater than in the substrate, a tensile stress will be generated in the coating as the temperature decreases. This may lead to adhesion loss and cracking of the coating. Contrarily, the resulting cooling stress will be compressive when the coating contracts less than the substrate ($\alpha_s > \alpha_c$). If the two expansion coefficients are equal ($\alpha_s = \alpha_c$), then there will be no cooling stress generated.

The final stress at the coating surface is obtained by adding the quenching stress result to the cooling stress result [96]. Therefore, the nature of the overall residual stress may be determined by superimposition of the cooling stress upon the tensile quenching stress [95], result as:

If, $\alpha_s < \alpha_c$ Stresses in the coating are tensile,

$\alpha_s = \alpha_c$ Stresses in the coating are tensile,

$\alpha_s > \alpha_c$ Stresses in the coating may be either tensile or compressive.

Chapter 4 – Experimental Work

4. 1 THERMAL SPRAYING PROCESS AND EQUIPMENT

4.1.1 SUPERJET System

In this research, a flame spraying facility was used to produce coating samples. This facility consists of three main parts:

1. Spraying gun
2. Coating powders
3. Gas system

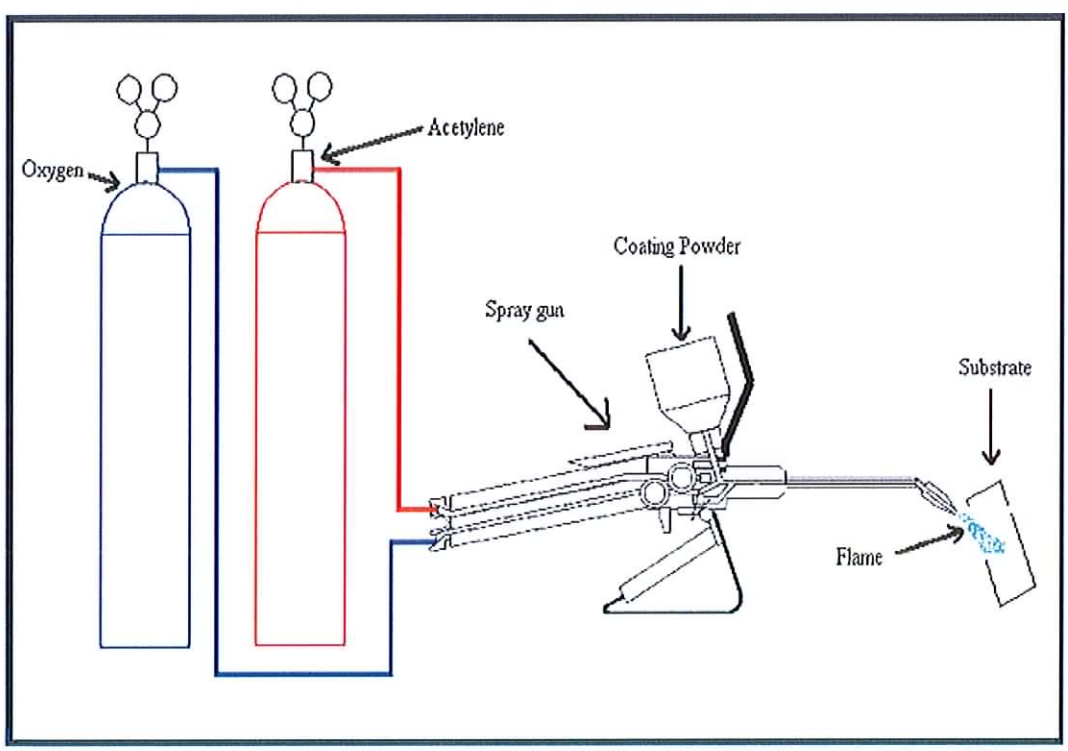

Figure 4.1. Schematic Diagram of the SUPERJET Spray Unit

The spraying system used for the research is called SUPERJET EUTALLOY, which is produced by Castolin Eutectic. Figure 4.1 showed a schematic diagram of the layout of the facility. In order to layout a complete flame spraying coating system, equipment such as a sand blasting machine and an extraction unit were introduced in

addition to the introduction of the equipment used for the coating production. These facilities integrate together for producing coatings and thermally sprayed engineering components.

4.1.2 SUPERJET Torch and Flame

Unlike the high pressure system that is used in the ordinary welding torch, the SUPERJET torch works on low pressure. Whereas, the high pressure system relies on equal gas pressures, the low pressure system, which is the SUPERJET spray system employed, works with high pressure oxygen and relatively low pressure acetylene.

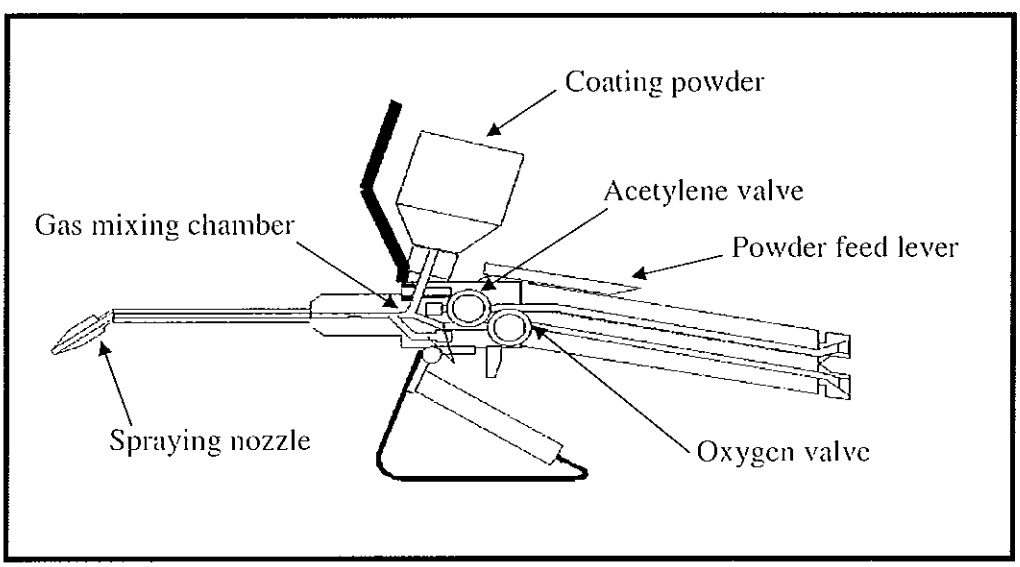

Figure 4.2. SUPERJET EUTALLOY Spray Torch

The SUPERJET torch is designed for small area spray application which is aided by a handle. The torch also comprises a powder feed lever, a replaceable spraying nozzle, a body frame, a coating powder container and two adjustable valves for controlling flow rates of the gases (oxygen and acetylene). The schematic diagram of the SUPERJET spray torch was shown in Figure 4.2.

The principle of operation of the SUPERJET torch is that oxygen and acetylene are directed separately by needle valves for ensuring precise flame adjustment. Each gas can be manually controlled from the torch by the control valves. The oxygen flows through the injector which then draws the powders into the system by aspiration. At

the same time, the acetylene gas is carried separately until it reaches the mixer assembly. At this point both gases are mixed, carry the powder through the system until they reach the spray tip and finally enter into the flame which is ignited by a flint lighter. The powder feed is controlled by the powder feed lever. Depressing the lever allows the powder alloy to flow into the oxygen stream. There are three types of flame setting on the SUPERJET torch: carburising, neutral and oxidising. Figure 4.3 depicts the type of SUPERJET flame settings [12].

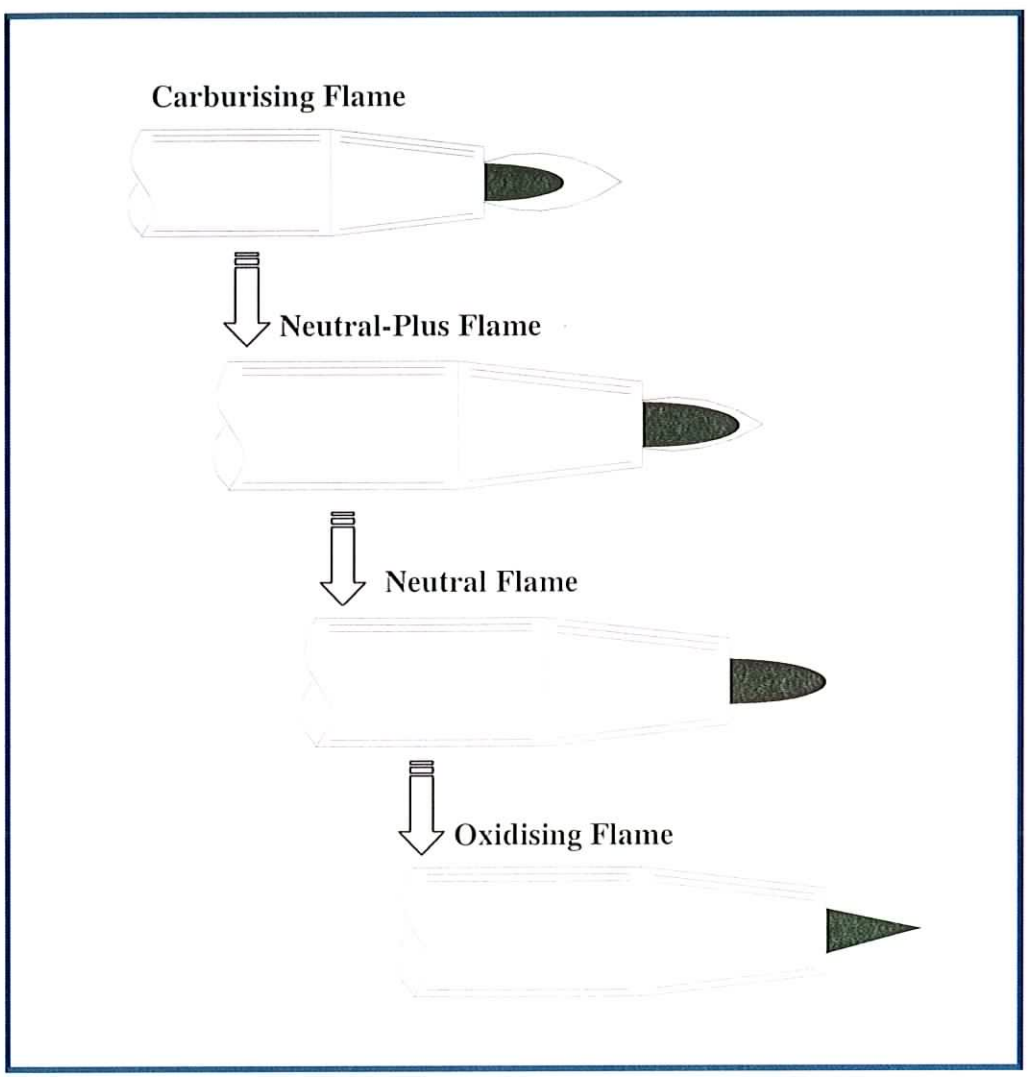

Figure 4.3. Flame Settings of SUPERJET Spraying Process

Carburising is used for wear surfacing operations, while the oxidising flame setting is used for the fusion welding of brass and bronzes. The neutral flame setting can be categorised into neutral and neutral plus. Neutral plus is mainly used for general welding operations. Neutral flame will become slightly oxidising when spraying and this reduces the presence of surface oxides since most powders contain the metallic fluxing agents.

4.1.3 Coating Powders

The essential requirements for the SUPERJET coating powder alloys are firstly, the melting point must be lower than that of the base metal and secondly, the coating exhibits self-fluxing characteristics thus being able to bond efficiently to the base metal [12].

The SUPERJET process uses atomised powders which have been atomised in a jet stream to make the powders spherical. This character not only makes the powders pass more easily through the torch, but also prevents the powders oxidising when they pass through the oxy-acetylene flame.

In the research, the coating powders used for the SUPERJET spray process are supplied by Castolin Eutectic. The powders that were used for the research are usually nickel based, alloyed with chromium, boron and silicon which lower the solidus temperature to approximately 1000°C. Boron and silicon also have a higher affinity for oxygen compared with nickel or iron at the operating temperature and this promotes a self fluxing action. Nickel-based coatings are used as uniform layers providing oxidation protection or in the form of bond coats, serve as part of a duplex thermal barrier coating [11].

Table 4.1 introduces the influence of some alloying elements [3, 12]:

Element	Characteristics and Influences
Boron	• Reducing element, deoxidises molten pool and interface • Makes molten alloy more fluid • Forms hard phases during boronation
Silicon	• Lowers melting temperature • Deoxidises molten pool • Increases fluidity • Increases deposit's resistance to high-temperature oxidation
Chromium	• Forms carbides with the carbon • Increases hardness of the deposit thus, increases the abrasion resistance • Very prone to oxidation • Resists heat
Nickel	• Resists corrosion • Easily machined • Resists scaling • Tends to gall when running against some metals
Cobalt	• Low friction coefficient • High wear resistance when alloyed with Tungsten • High resistance to softening at elevated temperatures
Carbon	• Forms carbides with certain metals (e.g. Nickel)
Copper	• Electricity conductive • Resistant to fretting corrosion

Table 4.1. The Characteristics and Influences of Some Coating Alloying Elements

A spread sheet with physical property data, characteristics and applications of the coating powders for the SUPERJET spray process have been listed, as shown in Table 4.2 [12]:

Product Number	**Characteristics**	**Sample Applications**
BroTec 10009	Good resistance to corrosion, erosion and abrasion under light load, with a hardness of 55-60 HRc.	Resurfacing of cams, decanting screw, steam gate components, pushers and stops.
TungTec 10112	Excellent resistance to erosion and abrasion by fine to coarse sized abrasives, with a hardness of 59-63 HRc. Consists of 60% W.	Coating of machine parts and equipment used in transport, handling and processing of minerals: transport screws, dies, turbine and fan impeller and wipers.
Bronzochrom 10185	Suitable for metal-on-metal chaffing. Hardness ranges from 350-390 HV30.Excellent corrosion resistance.	Recoating of shafts, bearing, and eccentrics. Coating of cast iron and steel molds for plastic material and glass.
ChromTec 10680	Good resistance to shocks and oxidation while is hot. Hardness ranges from 200 to 240 HV30.	Repair of gears, cast iron valve seats, keyways and bearing seating. Correction of machining errors.
CocalTec 10092	Good corrosion resistance to a wide range of chemical media. Hardness ranges 446-513 HV.	Exhaust valves, die casting moulds, impeller parts and cam.

Table 4.2. Powder Alloys Used for SUPERJET Spray Process

These coating powders all have self-fluxing characteristics since they are nickel based alloys which contain a proportion of boron and silicon [3]. Table 4.3 lists the chemical compositions of the alloy coating powders [12].

	Element % (weight)										
Powder	C	Si	B	Fe	Cr	Ni	Co	W	Cu	Sn	WC
10185	0.1	3.2	2.15	0.5	0.5	bal	-	-	-	-	-
10680	0.05	2.25	1.3	0.5	0.5	bal	-	-	-	-	-
10092	1.5	1.2	1.5	0.5	23.5	bal	37.5	4.2	-	-	-
10009	0.75	4.2	3.3	3.7	15.5	bal	-	-	-	-	-
10146	-	-	-	-	-	2.1	-	-	bal	8.1	-
10112	0.1	4.55	3.1	6.1	7.2	bal	-	-	-	-	60

Table 4.3. Chemical Compositions of Alloy Coating Powders

4.1.4 SUPERJET Spray Process

The SUPERJET process is a means of depositing a wide range of alloy powders through a specially designed oxy-acetylene torch. The SUPERJET EUTALLOY process is designed for protective coating of machine parts and tools subject to a variety of wear phenomena.

Oxyfuel gas powder spraying is classified into two types: cold spraying and hot spraying. SUPERJET is an example of hot spraying. SUPERJET is a low heat input process which affects a bond with the base metal by solid phase diffusion. Bonding is achieved by diffusion of the alloys in the base metal.

The nozzle of the torch is designed to operate at a particular gas pressure, and it can be removed or replaced. There are various sizes of nozzle tips available, and the size chosen depends on the coating application. Size's range from 1.00mm~2.85mm [12]. The heating capacity of the flame can be adjusted by using the gas control valves on the torch. The distance between the end of the inner cone of the flame and the surface of the work-piece was varied according to the ease with which the different powders were being laid down.

Parameters	Values	Unit
Delivery rate	0.5 ~ 5	kg/h
Oxygen flow	90 ~ 1200	NI/h
Acetylene flow	80 ~ 1100	NI/h
Operating pressure of oxygen	1.5 ~ 2.5	Bar
Operating pressure of acetylene	0.5 ~ 0.6	Bar
Temperature of pre-heating	150	°C
Temperature of the flame for spraying	2000	°C
Temperature of the flame for fusing	3000	°C
Temperature of fusing on the coating	700 ~ 1000	°C
Distance of spraying	25 ~ 30	mm
Distance of fusing	6 ~ 20	mm

Table 4.4. Parameters Suggested by Castolin Eutectic for Spray Fuse Process

Depending on the coating powders used, the SUPERJET spray process can be conducted through a one-step process or via a two-step process. The one-step process refers to spraying only, whereas the two-step process consists of two stages: spray and fuse. The two-step spray fuse process was developed to improve the strength of bond between coating and substrate which is completed with a normal thermal spraying process, and takes advantage of the typical smoothness and uniformity of the coating at the same time [3]. The standard operation parameters are shown in Table 4.4 [12].

The complete two-step SUPERJET spray fuse process is described sequentially in the following sections as: surface preparation, pre-heating, spraying and fusing process.

4.1.4.1 Surface Preparation

The finish and integrity of the substrate surface are crucial for the application of thermal-sprayed coatings [97]. The adhesion of a coating on the substrate is directly related to the cleanliness of the substrate surface. Surfaces for thermal spraying have to be chemically and mechanically well prepared for a good adhesion. Increasing the roughness of the surface is a well-known effective method for surface cleanliness,

and this also can increase the bond strength between a coating and the adjoining substrate. Among the various methods for surface preparation, grit (sand) blasting is an efficient way to produce cost-effective and reproducible results [10]. Sand blasting is one of the types of grit blasting, and it is a process of removing the rust, grease, oxides, debris and impurities from the surface using a jet of sand. A sand blasting unit was used to prepare substrate surfaces for the research.

The unit has an eye visor which enable visibility while maintaining safety standard over the entire work area. The system included a hand held blasting gun, a large cabinet and a sand collector. The sand is collected into a compressed air stream by a vacuum effect, and propelled out of the gun onto the substrate surface. The impinging sand falls down through a grid into the sand collector for recycling. The roughness of the substrate surface may be controlled by varying the air pressure, yielding roughness in the range of 6 to 15μm.

4.1.4.2 Preheating

Preheating was carried out by igniting the SUPERJET gun and heating the substrate with the gun flame up to a desired temperature prior to the deposition, as shown in Figure 4.4. Preheating of the substrate is to take the chill out of the base metal and prevent the hot powder from contracting and lifting off. It also removes the moisture built up on the substrate surface by exposing the surface to a high temperature. The preheating temperature for a steel substrate is usually within the range of 90°C ~ 150°C [19]. Before the preheating treatment starts, all safety clothing and ventilation facilities must be in place. The suitable nozzle for the application is cleaned and assembled on the SUPERJET gun. A treatment of preheating the substrate surface to a temperature of 150°C was conducted. Under the preheating of this temperature, the substrate surface should have a slightly brown appearance. It should be noticed that when the substrate surface turns "blue", it means that an oxide film had formed, which is undesirable.

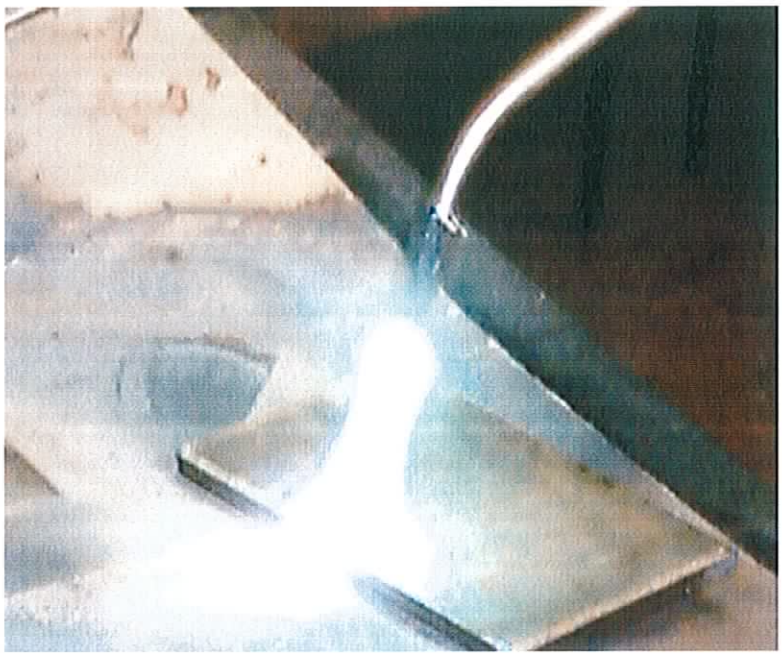

Figure 4.4. Preheating of the Substrate during SUPERJET Spray Process

4.1.4.3 Spraying

Spraying parameters vary depending on the thermal spraying process used and the type of material being sprayed. In the case of SUPERJET spray process, as Castolin Eutectic have outlined recommended spraying parameters for the deposition of a series of self-fluxing alloy powders materials, as shown in Table 4.4.

The Eco-Pak, which is a container with required coating powders, is installed on the torch. The switch on the oxygen bottle is opened and the pressure is set to a value as shown in Table 4.4. Then the acetylene gas is turned on and set to the proper pressure. By pressing the powder feed lever, the coating powders are carried by the gases and propelled out of the nozzle. The distance of spraying is kept approximately at 20mm and the movement route of spraying is recommended as a "Z" shape. Figure 4.5 demonstrates the spraying process.

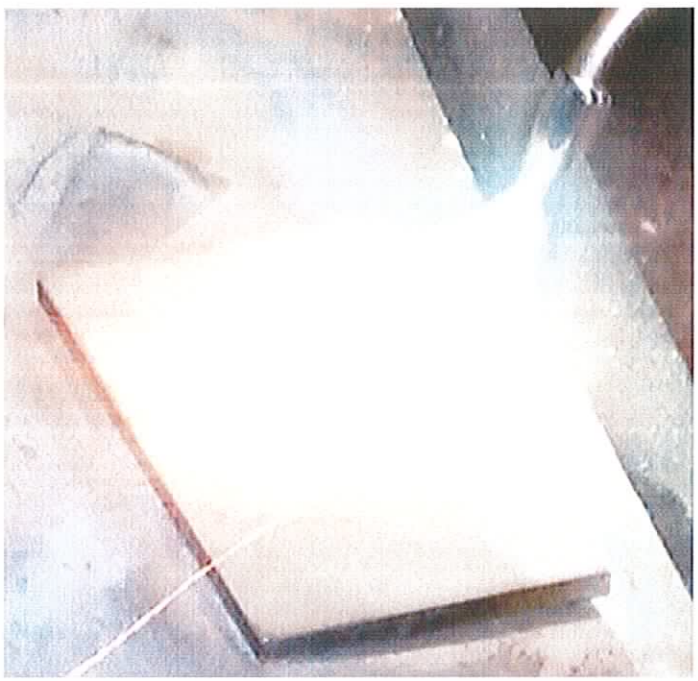

Figure 4.5. Spraying during SUPERJET Spray Process

4.1.4.4 Fusing

Fusing is an operation that involves heating the coating together with the substrate to a temperature between the solidus and liquids of the coating alloy. After the spraying, a wet-out process which is called fusing was carried out in succession. The fusing process is to promote the bonding between the coating and the base metal, and to eliminate the oxide formed during spraying. This process also develops a metallurgical structure in the coating and a bond with the substrate, which in mild steel has a strength of 380 ~ 550MPa, depending on the coating alloy [3]. Fusing in the SUPERJET process is carried out by moving the spray torch towards the part to a distance as stated in Table 4.4, and as shown in Figure 4.6. After the fusing, allowing the part to cool in room temperature.

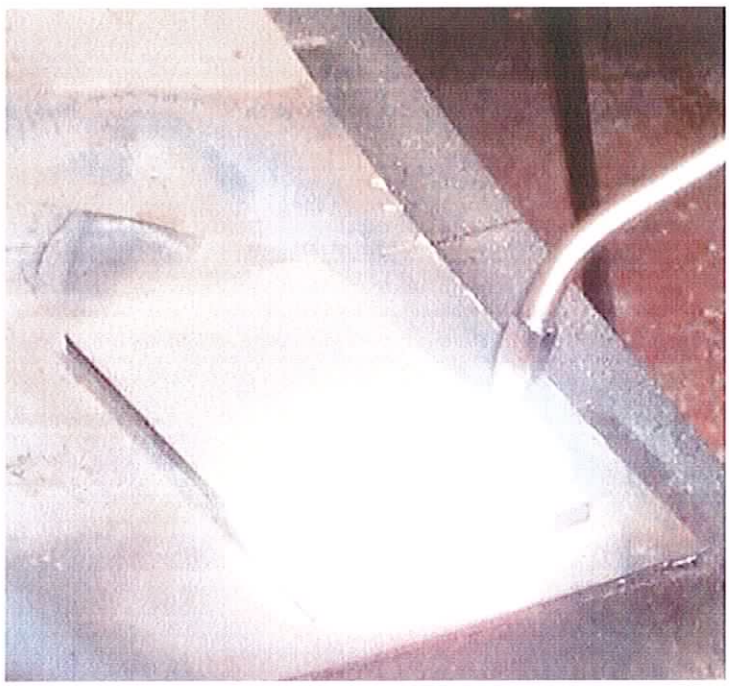

Figure 4.6. Fusing during SUPERJET Spray Process

4.1.4.5 Advantages and Applications of SUPERJET Process

SUPERJET spray process uses standard oxy-acetylene hoses and this makes the process easier to be carried out. Also, this process is able to produce coatings with a minimum thickness of 80μm and doesn't cause dilution to the base metal. The hardness of the coatings that are produced by SUPERJET process ranges from 15-64RC.

The main applications of SUPERJET process are:

i. Mould reclamation or finished machining errors
ii. Finish machining errors of tool and die work
iii. Joining and building up of metallic components
iv. Any surfacing or overlaying operation of where mild steel is substituted for a higher grade or more expensive steel
v. Overlaying stainless steels and bronzes including phosphor bronze

4.1.2 CASTODYN DS 8000 Equipment and Process

CASTODYN DS 8000 (CDS 8000) is an advanced modular oxy-acetylene thermal spray system. It is designed to spray a wide range of alloys and other materials (e.g. polymers, ceramics) for many different applications with or without remelting. It can be integrated into automated installations for mass-production applications [12].

Figure 4.7 shows the CDS 8000 spray process system. The principle of the CDS 8000 system is similar to SUPERJET spray process (Chapter 4.1.4), except it has an additional connection for compressed air, as shown in Figure 4.8. CDS 8000 spray process is more powerful than the SUPERJET process in terms of flow rate and velocity of the coating powders.

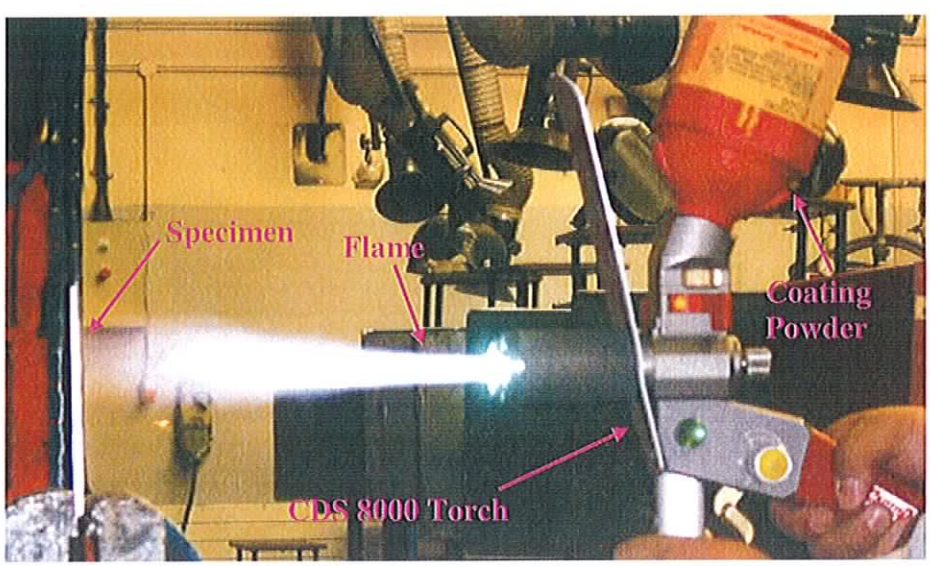

Figure 4.7. CDS 8000 Spray Process System

There are four sets of standard spray modules (SSM) available for the CDS 8000 process, from SSM 10 to SSM 40. Each SSM consists of a powder injector and a spray unit comprising a power module and a flame nozzle. A compressed air pressure control gauge (Figure 4.8 (a)) is utilised in the system, with one end connecting to the compressed air supply unit (Figure 4.8 (b)) and the other end connecting to the back of the spray gun next to the air and acetylene valve (Figure 4.8 (c)). Table 4.5 shows the parameters that were suggested by Castolin Eutectic for the CDS 8000 process [12].

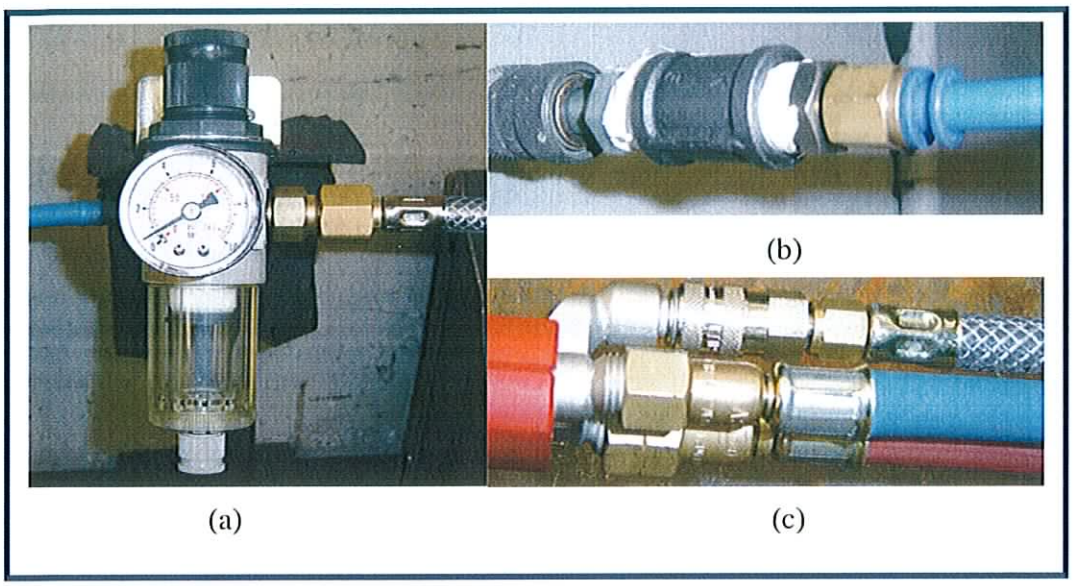

Figure 4.8. Compressed Air Valve and its Connections

Parameters	**Values**	**Unit**
Delivery rate	1 ~ 8	kg/h
Oxygen flow rate	500 ~ 2000	NI/h
Acetylene flow rate	400 ~ 1800	NI/h
Operating pressure of oxygen	4.0	Bar
Operating pressure of acetylene	0.7	Bar
Operating pressure of compressed air	0 ~ 6	Bar

Table 4.5. Parameters Suggested by Castolin Eutectic for CDS 8000 Process

4.1.3 Safety and Protection

Thermal spraying process produces dust and fume. The build up of some metals in the form of dust can lead to fire and explosions, especially of concern are aluminium and zinc powders. An extraction unit is used to remove this dust and fumes from the working environment.

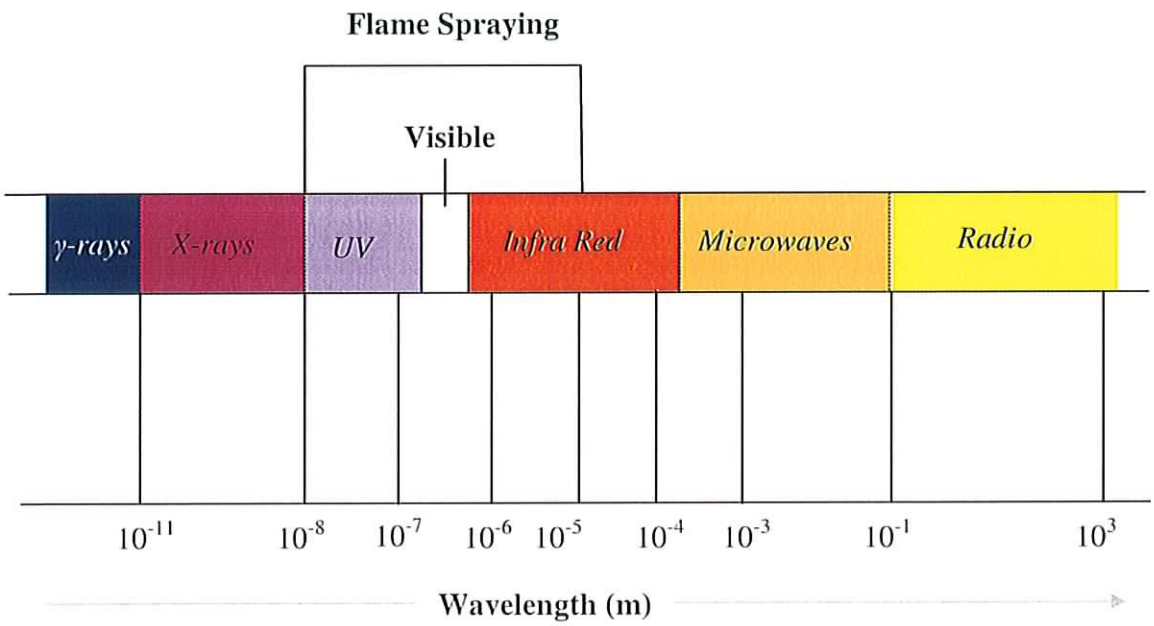

Figure 4.9. The Wavelength of Various Radiations

During the spray process, caution and care must be shown. Any potential ignitable and explosive items should be kept away from the flame. Pressurised gas cylinders should be handled carefully to avoid any accidents. The gas cylinders should be stored in a location which is out of the reach of direct sunlight and extreme temperature. Protective equipment must be worn, such as protective eye glass and ear plugs. The eye and ear protection is especially important due to the presence of ultraviolet and infrared radiation, as shown in Figure 4.9. Directly receiving the radiation of the flame is harmful to the eyes and skin. Also, ear protection equipment should be wearing since thermal spraying processes generate high noise levels. In the research, safety goggles and foam ear plugs were used for protection.

4. 2 HARDNESS MEASUREMENT

There are three methods for measuring the material hardness which are generally used, namely; static indentation, dynamic indentation and the scratch method. In the research, the static test method was used to obtain hardness values of the surface coatings. In the static test, a ball or a diamond cone or a pyramid shaped indenter is forced into the material.

First, the hardness was measured at the cross sections of the coatings, by the Vickers test method using the *BUEHLER MICROMET II* micro hardness tester, as shown in Figure 4.10 (a). For the hardness measurement of the coating surface, an *INDENTEC* hardness tester was used, as shown in Figure 4.10 (b).

(a) (b)

Figure 4.10. Hardness Testers: (a) Microhardness Tester for Cross Sections of Coatings; (b) Tester for Coating Surface Hardness Measurement

The indentation was observed using a microscope at a magnitude of 50X and the indentation width was measured (Figure 4.11). The force P applied to cause the indentations was 300gf and 30kg in two measurements respectively (micro hardness measurement and macro hardness measurement). The arithmetic mean of the two

separately measured diagonals d (in millimeters) is given in the following equation:

$$d = \frac{d'+d''}{2} \qquad \text{Equation 4.1}$$

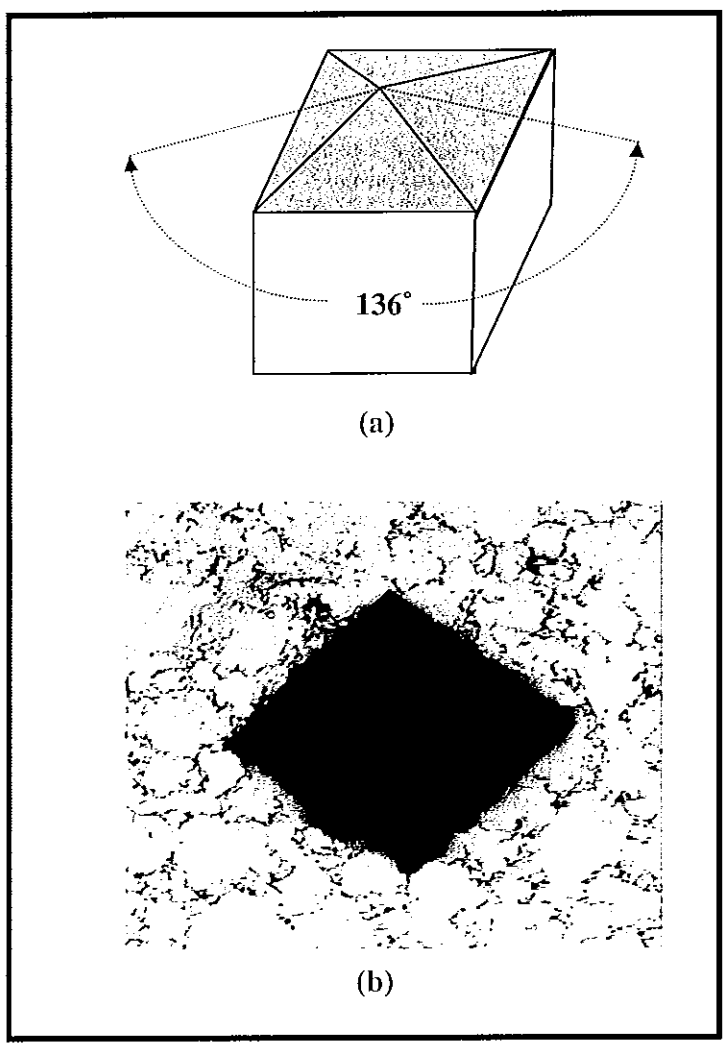

Figure 4.11. Vicker's Hardness Test, a) Indenter; b) Indentation

4.3 TEMPERATURE MEASUREMENT

Continuous temperature measurement is essential to monitor the deposited material temperature while spraying. For example, for calculating the residual stresses in the coating by using curvature methods, knowing the temperature value of the sample during the process is compulsory.

A thermocouple is attached on the sample surface and the temperature is measured for individual process (preheating, spraying and fusing). The thermocouples were connected to a *Cole-Parmer DIGI-Sense* thermocouple thermometer and *K* type thermocouple to obtain the temperature values.

4.4 MICROSTRUCTURE ANALYSIS

There were a number of coating samples prepared for optical microstructure analysis. Some of the samples that were examined focused on the cross sections of the coating, whereas some samples obtained more information from the coating surface. Observation of the cross section of the coating (perpendicular to the coating surface) provided information about the surface of the substrate and the changes that occurred in the microstructure through the deposit. Examinations along the coating surface provided more information about the coating appearance.

To optimise the quality of the microscopic observation, the coating sample must be prepared metallographically. Care has to be taken to ensure the proper grinding and polishing procedure is chosen. Poor preparation will result in scratches, deformation, smearing, edge rounding, pull-out, cracks, contamination, embedded abrasive, lapping tracks and staining [98].

Metallographic specimen preparation is a valuable process for the characterisation of thermally sprayed coatings. In the experiments, the preparation process consisted of three steps: sectioning, mounting, and grinding and polishing of the surface of the sample. Etching is required for some cases to obtain images with good contrast.

4.4.1 Sectioning

Since the coating samples will be investigated using SEM, the size of the sample must be in the limit of 25mm × 25mm × 15mm in length, width and height respectively. Samples with various thickness and different coating materials were prepared.

4.4.2 Mounting

There are two mounting techniques: cold-castable mounting and hot-compression mounting. Cold-castable mounting involves curing an epoxy, mixed with a fluorescent dye and leaving in the room temperature for over eight hours. Hot-compression mounting involves setting a sample in a thermoplastic or thermosetting resin, subjected to an elevated temperature (from 140 to 200°C) and high pressures (from 20 to 40MPa) for 7 to 10 minutes. The difference between these two mounting techniques is that in hot-compression mounting, there is very little penetration of the mounting compound in the voids, resulting in abrading and smearing of the coating's surface during the grinding, hence the porosity in such coatings may be covered off, as found by Glancy [98]. In cold-castable mounting, the epoxy protects the voids during grinding and the fluorescent dye helps the metallographer identify such pores. Glancy [99] states that where possible, cold-castable mounting techniques should be used to determine the true structure of thermal spray coatings. In this research, the cold-castable mounting procedure was utilised.

4.4.3 Grinding and Polishing

Figure 4.12. The METASERV Polisher-Grinder Used in the Research

In the stage of grinding, a *METASERV* polisher-grinder, as shown in Figure 4.12, was used. Throughout the preparation process, Silicon-carbide (SiC) papers are used to grind the samples, since SiC papers are very effective on materials up to approximately 1000HV. The procedure moves from a coarse paper up to a fine abradable paper, as outlined in Figure 4.13. The grinding parameters are shown in Table 4.6. Each abrasive size is used for five minutes in turn, starting at P160 working towards P1200.

Equipment	**METASERV polisher-Grinder**
Abrasive format	Silicon Carbide papers
Abrasive size	P160 – P1200
Time	5 minutes (each paper)
Rotation	Complementary
Cooling	Water

Table 4.6. Parameters for Grinding

Polishing is carried out since the light optical microscopy requires that a specimen be both flat and highly reflective. Polishing also removes the deformation induced during fine grinding, as well as removing all smears from the surface of the specimen. A *BUEHLER* diamond suspension polisher was used in the research.

Diamond abrasives are very effective during the polishing stage. The most commonly used diamond particle sizes are 3 and 1 micron. Some variables may influence the final results, such as the polishing cloth, lubricant, force, revolutions per minute and time. Table 4.7 shows the parameters used for the diamond polishing. Each abrasive size is used for five minutes in turn, starting at 3μm and finishing at 1μm.

Equipment	The BUEHLER STRUERS Specimen Preparation Unit
Abrasive	Polycrystalline Diamond
Abrasive size	3, 1μm
Time	5 minutes (each size)
Platen rpm	250
Rotation	Complementary
Cooling	Water

Table 4.7. Parameters for Polishing

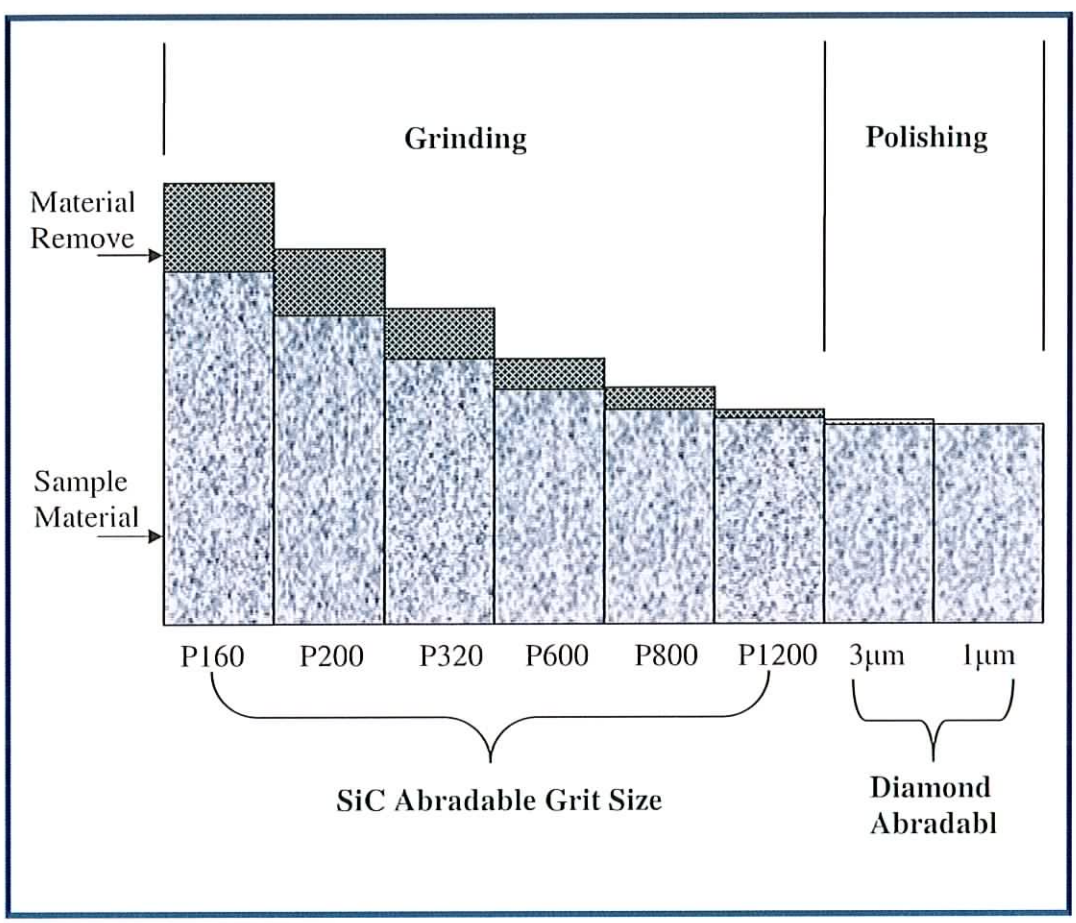

Figure 4.13. Grinding and Polishing of Metallographical Preparation of Samples

In general, a polished specimen will not exhibit its microstructure since the incident light is uniformly reflected [100]. The final polished sample surface was examined under a microscope with bright-field illumination, where features such as pits, pores or cracks may be observed. However, in the case of those small differences in the

microstructure that cannot be recognised, the image contrast must be increased. Therefore, chemical etching is used in the research to optimise the imaging contrast in the optical microscopic investigations. The etching solution that was used is a mixture of 100ml Ethanol and 3ml Nitric acid.

4.4.4 Optical Microscope

The optical light microscope is a powerful tool for examining and evaluating the microstructure of various materials. The instrument has a resolution of 250nm with a similar depth of field and is capable of revealing polished and etched material specimens. However, as with any visual technique, the information derived depends critically upon the metallographic preparation procedure.

In the research work, the coated samples were prepared metallographically following the procedures as stated in the Chapter 4.4.1-4.4.3. In the terms of coating microstructure analysis, the optical microscope can be used to analyse the fraction and size of the melted and unmelted particles in the coating, reveal the size and fraction of pores and voids in the coating, and present the substrate deformation near the coating area. The *Olympus U-CMAD-2* optical microscope, as shown in Figure 4.14, was used in the research work.

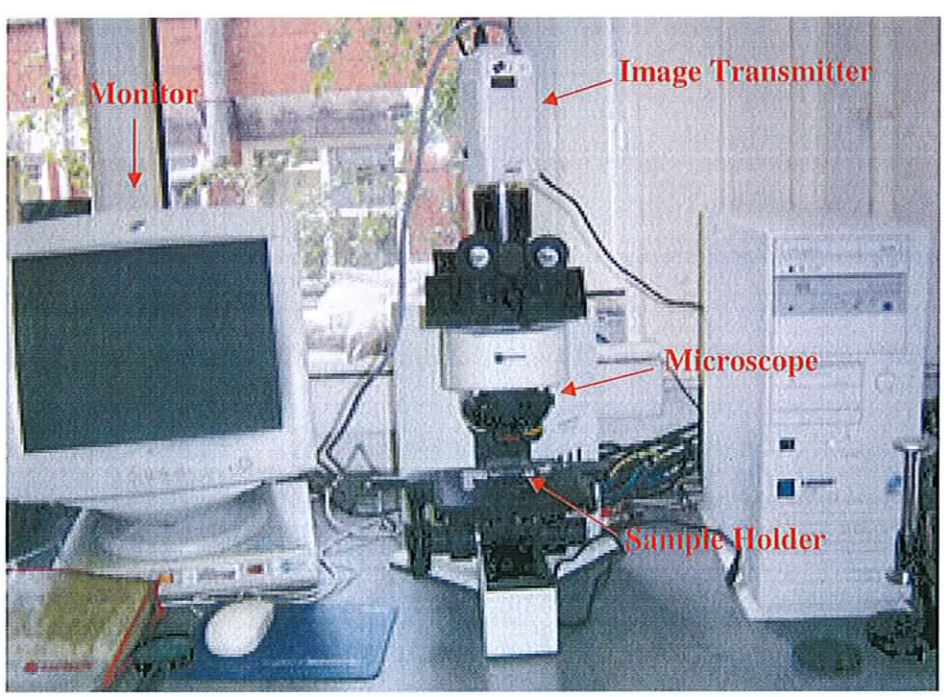

Figure 4.14. The Olympus U-CMAD-2 Optical Microscope

The optical microscopic study offers a basic and quick observation of the microstructure of the material, before viewing a microstructure on more advanced observation instruments, such as SEM.

4.4.5 Scanning Electron Microscope

A *Jeol 8600 electron microprobe* has been used for coating microstructure and element analysis in the research, as shown in Figure 4.15. The electron microprobe consists of three main parts:

i. Electron gun and a system of electromagnetic lenses for producing a focused beam and scanning coils
ii. Specimen stage with X-Y-Z movement
iii. Detection system

The microprobe functions as a scanning electron microscope. The SEM images the surface (topography) of virtually any solid material or biological sample, and images from secondary electrons (SEI) and back scattered electrons (BSI) can be produced. Also, hard copy and digital imaging can be produced using the *Semafore* digitiser attached which gives high quality digital images making it easy to store and retrieve images from a database.

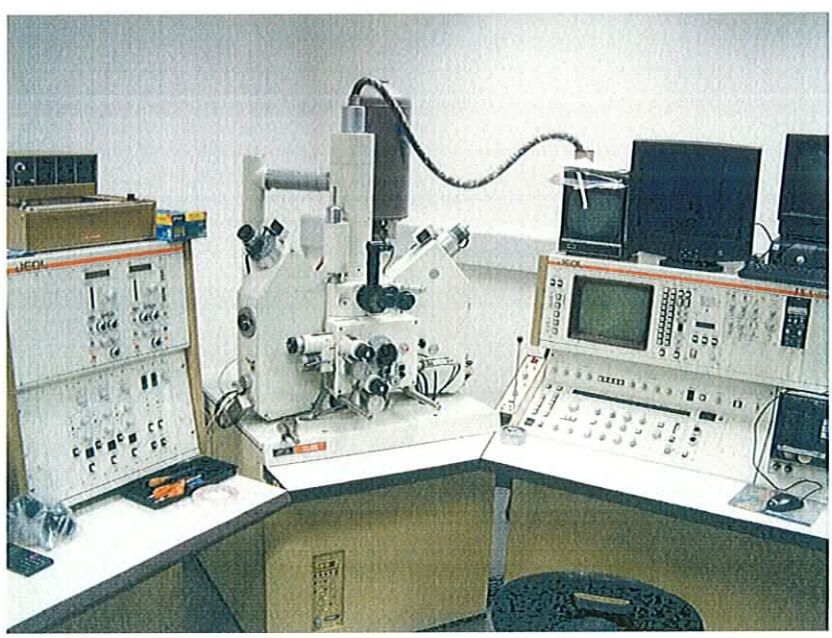

Figure 4.15. A Jeol 8600 Electron Microprobe System

In addition to the microstructure imaging capability, *Jeol 8600 electron microprobe* can also be used for elemental analysis. Electron probe microanalysis is used for chemical analysis of micro-volumes at the surface of polished solid specimens utilising a fine beam of electrons to bombard the surface of the specimen. The electron beam generates x-rays whose wavelength or energy is a characteristic of the elements present in the sample. The intensities of the x-ray are a measure of the proportions of the elements present. The attached EDS system allows any element to be mapped onto the specimen.

During the SEM investigations, flare may be observed on the areas of examination. This phenomenon will critically affect the quality of the images. To eliminate flare, the mounted samples were coated with evaporated carbon using a *JOEL JEE 4B* coating unit. This deposited a very thin layer of carbon to make the sample conductive over the surface.

4.5 COATING THICKNESS MEASUREMENT

Coating thickness measurement is an important procedure in the research. Two methods have been used in the current work: dial gauge method and microscopic method. The dial gauge method is based on the comparison between the measurement of thickness of the sample before and after coating deposition process. The microscopic method includes measurement by using an optical microscope and a SEM.

4.5.1 Dial Gauge Method

The dial gauge that was used in the experiments is a *Mercer* type gauge which yields thicknesses within ±10μm. The gauge is set up on a mount resting on a flat surface, as shown in Figure 4.16. Initially the substrate without the coating was placed on the flat surface and the dial gauge was zeroed to exclude the thickness. After the deposition, the component with the sprayed coating was placed on the flat surface and the dial gauge measured the displacement. The gauge has moved from its initial position to its new height, hence the coating thickness was deduced.

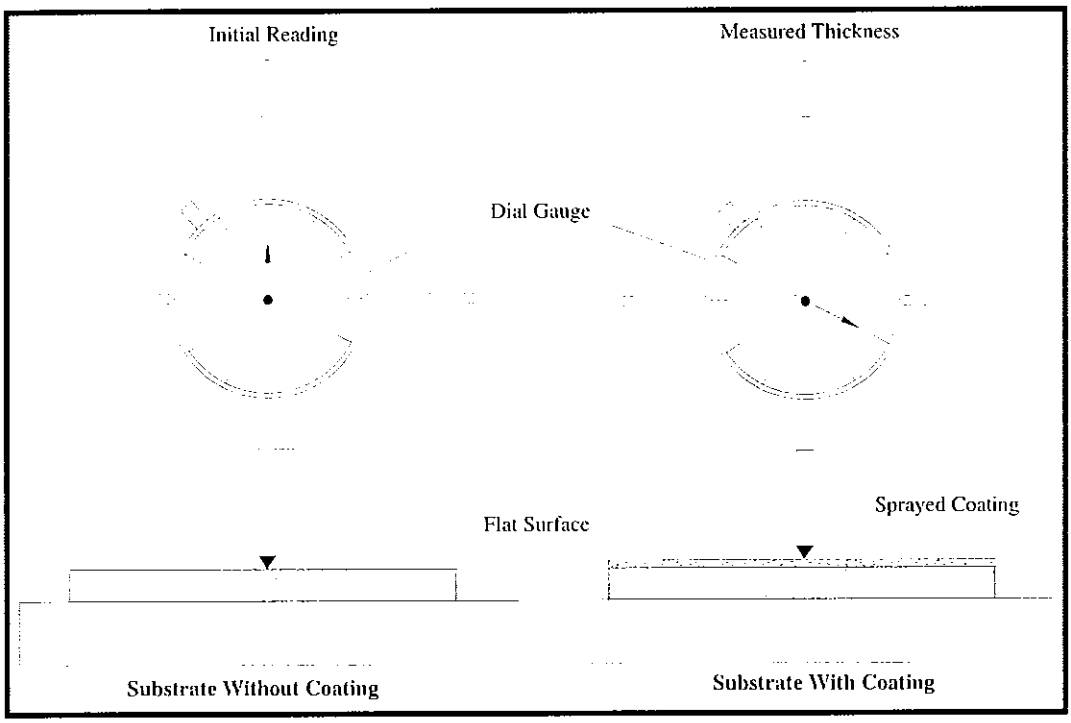

Figure 4.16. Dial Gauge Method for Coating Thickness Measurement

4.5.2. Microscopic Measurement

In the microscopic measurements, the optical microscope and the SEM were used respectively to measure the average thicknesses of the coatings. This process involves sectioning, mounting, grinding and polishing the sample. In some cases etching was required to show the difference between the substrate and the coating. A number of distributed measurements were made along a deposit's length in the study and then averaged to determine the coating thickness.

4.6. SURFACE ROUGHNESS MEASUREMENT

4.6.1 Mechanical Method

The roughness is defined as the ratio of true surface area to apparent or projected surface area. It may be measured absolutely by adsorption or capacitance techniques which measure the true surface area. However, the stylus traverse method is more practical [101].

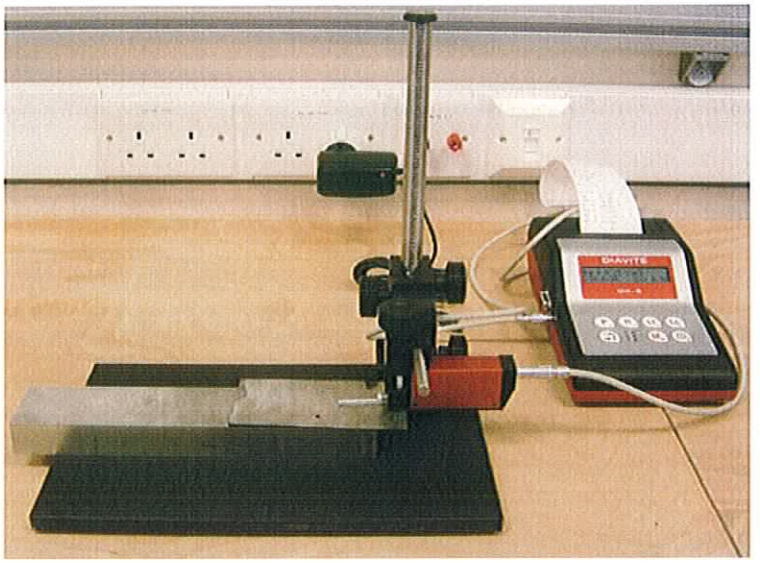

Figure 4.17. DIAVITE DH-6 Surface Roughness Tester

The *DIAVITE DH-6* model surface roughness tester was used in the measurements, as shown in Figure 4.17. Three statistical surface roughness descriptors or parameters that give the average behaviour of the surface height of the machine surface asperities were recorded at L_c = 0.8 mm and L_t = 4.8 mm. These surface parameters are: the arithmetic average roughness R_a, the root mean square roughness R_q, and the peak-to-valley height or roughing depth R_t. The parameters measured are the most effective surface roughness measures, and are the most commonly and widely used in general engineering practice. Figure 4.18 shows the *Taylor-Hobson* surface roughness tester that is also used in the investigation.

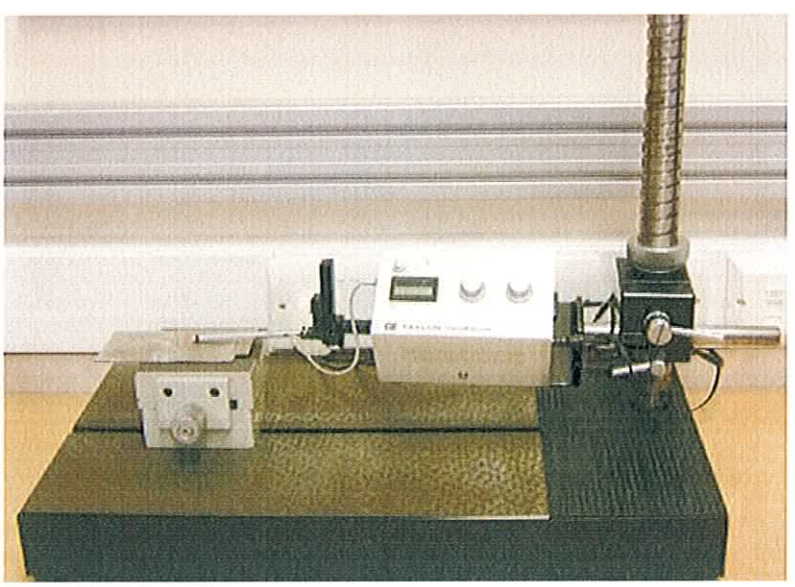

Figure 4.18. Taylor-Hobson Surface Roughness Tester

4.6.2 Optical Method

The optical profiler *MicroXAM S/N 8038*, as shown in Figure 4.19, measures roughness, finish and texture of surfaces ranging from highly polished optics, wafers and disk media to relatively rough surfaces such as rolled steel and aluminium, paper, plastics and ceramics. However, this optical profiler is not suitable for measuring the surface features of very rough surfaces, as its vertical scan range is limited to 100 microns [102].

The *MicroXAM S/N 8038* optical profiler has following measurement features:

i. Digitised resolution: 384×244 or 512×488 or 752×480 pixels;
ii. XY translation stage range: 100×100mm;
iii. Vertical scan range: 100 microns;
iv. R-θ stage range: 100 mm in y direction;
v. Tip-tilt range: ± 7 degrees;
vi. Data acquisition time: up to 7.2 μm/s

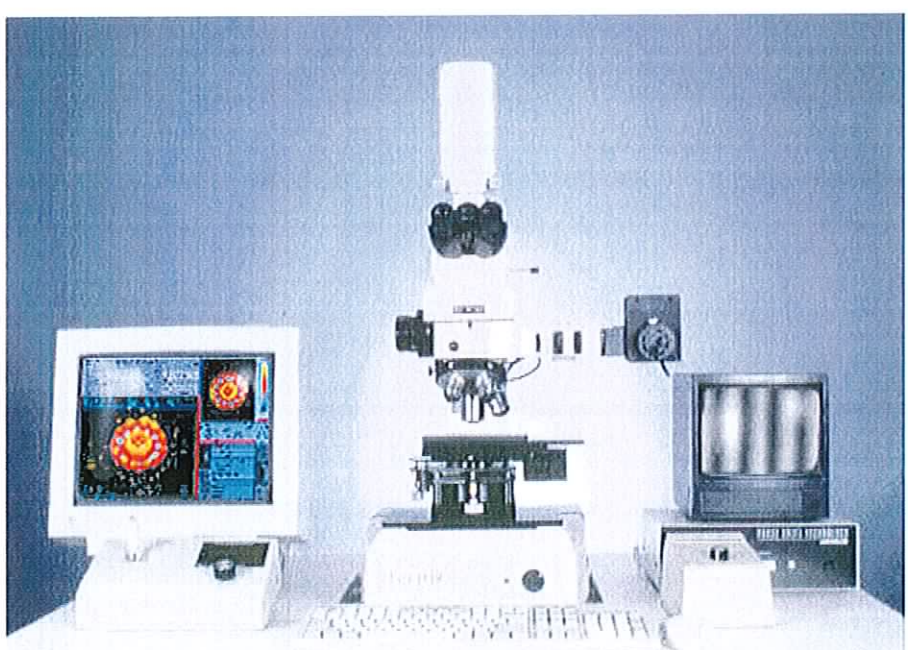

Figure 4.19. MicroXAM S/N 8038 Optical Profiler having Optical Resolution of 0.5 μm and Vertical Resolution of 1 nm

4.7 MEASUREMENT OF YOUNG'S MODULUS OF COATING

The elastic modulus, also known as Young's modulus and Poisson's ratio are two key mechanical properties of materials. To measure the residual stresses of a coating, the elastic modulus (E_c) and Poisson's ratio (ν_c) for a coating are required, hence determination of these properties is crucial for the project.

The elastic moduli of a coating and the stresses at which material failure occurs are very important to determinate a coating's reliability. The determination of a coating's Young's modulus is difficult, as generally the coating is attached to a substrate. However, there are many types of techniques that are applicable to the calculation of Young's modulus of coatings. They are commonly classified into five categories [103-106]: indentation; beam bending; vibration; ultrasonic surface wave and scanning acoustic microscope. In the research, only the beam bending method was proposed and utilised.

4.7.1 Cantilever Beam Method

One of the methods using bending theory to measure the stiffness and Poisson's ratio of the coating is the cantilever beam method, which is described by Rybicki *et al* [107]. An adapted experimental setup which is used to measure the Young's modulus and Poisson's ratio for thermal sprayed coatings is shown in Figure 4.20. Two uniaxial strain gauges are longitudinally and transversely placed on the coating surface. Another two strain gauges are placed directly opposite on the substrate side. One side of the beam is clamped, and a force is applied to the other end of the substrate. A dial gauge is mounted at the end where the load is applied. All the strain gauges are connected to a multi channel strain indicator to give individual readings. The strain is measured to yield the two properties using "Laminate Plate Theory".

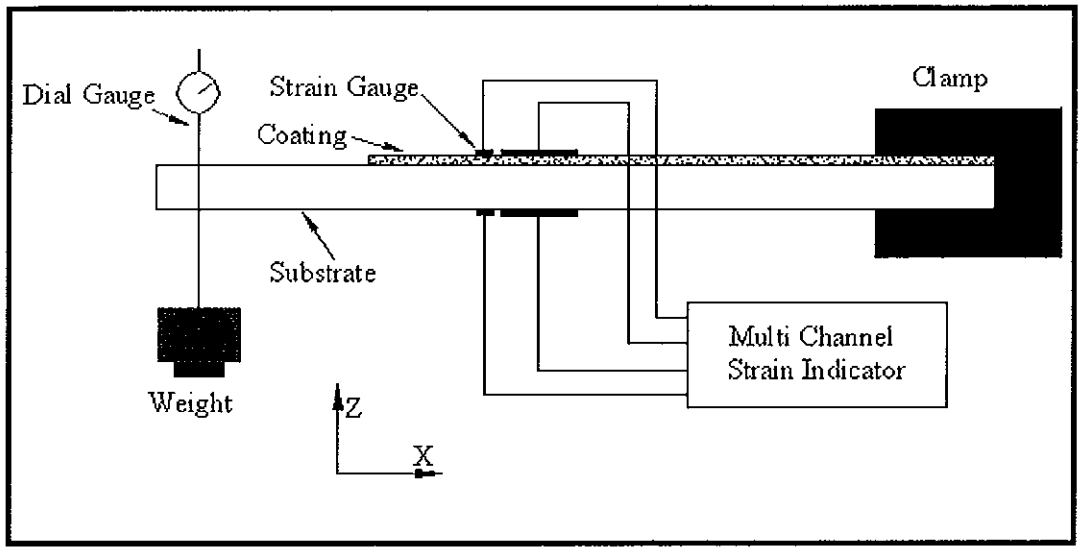

Figure 4.20. Experimental Setup of the Cantilever Method for Coating Stiffness Measurement

The laminate plate theory is used in the cantilever beam method to relate the unknown E_c (coating stiffiness) and ν_c (coating Poisson's ratio) to the loading of the gauge sections. This theory assumes a linear strain distribution through the thickness of the coated cantilever beam, and the plane stress conditions. Figure 4.21 shows a schematic diagram of the stress and strain distribution for a coated cantilever with a load applied.

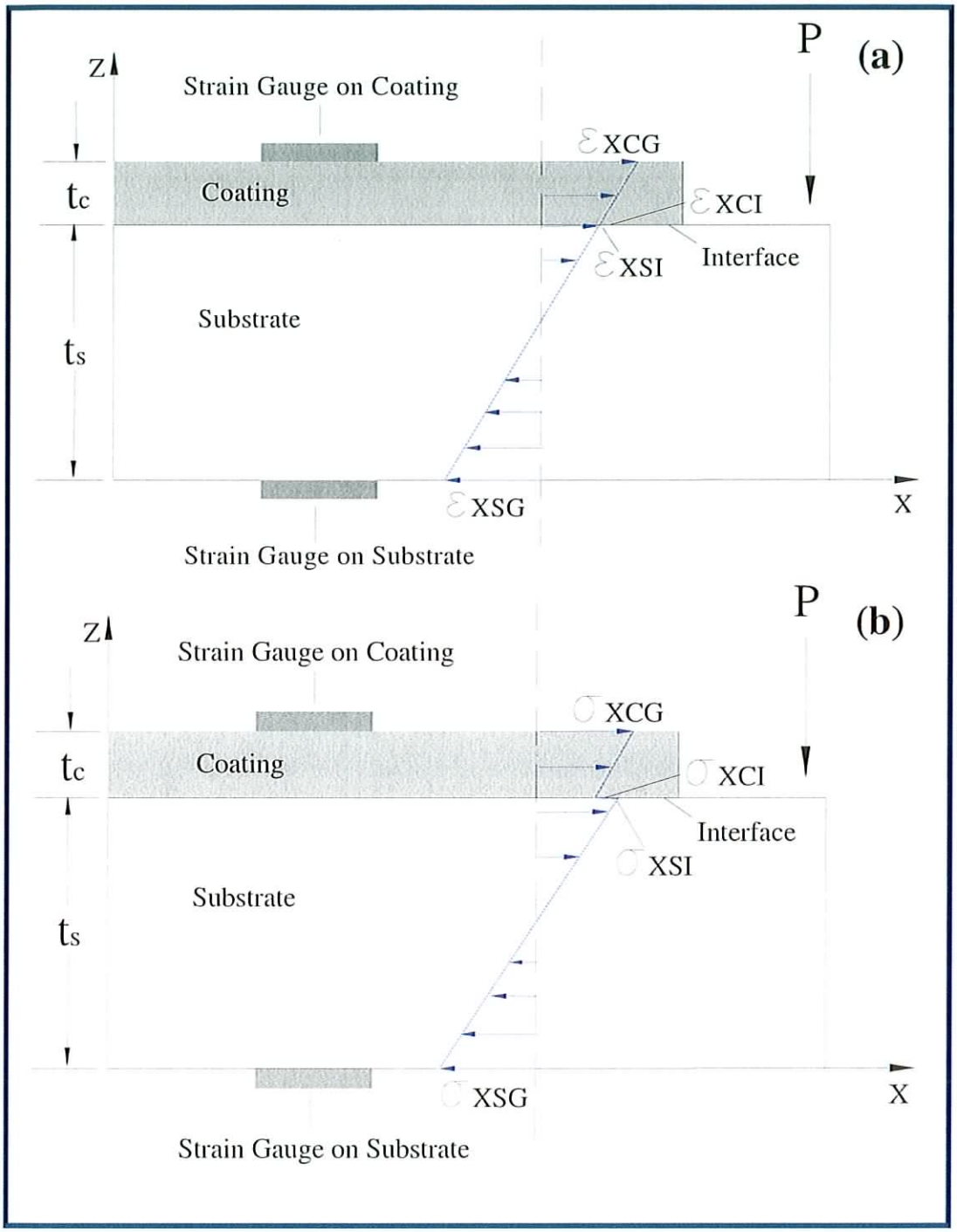

Figure 4.21. Sketch of Stress and Strain Distribution of a Coated Cantilever Beam, (a) Strain, (b) Stress

Rybicki *et al* [107] have discussed the equilibrium equations for the coated beam. The stresses (σ_x in the x-direction, σ_y in the y-direction) are related to the forces (F_x in the x-direction, F_y in the y-direction) and moments (M_x in the x-direction, M_y in the y-direction) by:

$$0 = F_x = \iint \sigma_x dz dy \qquad \overline{M}_x = M_x = \iint \sigma_z z dz dy \qquad \text{Equation 4.2}$$

$$0 = F_y = \iint \sigma_y dz dy \qquad 0 = M_y = \iint \sigma_y z dz dy \qquad \text{Equation 4.3}$$

For the coated beam,

$$F_x = w(\sigma_{XSI} + \sigma_{XSG})\frac{t_s}{2} + w(\sigma_{XCI} + \sigma_{XCG})\frac{t_c}{2} \qquad \text{Equation 4.4}$$

$$M_x = w[\sigma_{XSG}\frac{t_s^2}{2} + (\sigma_{XSI} - \sigma_{XSG})\frac{t_s^2}{3}] + w[\sigma_{XCI}(t_c)(\frac{t_s}{2} + \frac{t_c}{6}) + \sigma_{XCG}(t_c)(\frac{t_s}{2} + \frac{t_c}{3})] \qquad \text{Equation 4.5}$$

$$F_y = w(\sigma_{YSI} + \sigma_{YSG})\frac{t_s}{2} + w(\sigma_{YCI} + \sigma_{YCG})\frac{t_c}{2} \qquad \text{Equation 4.6}$$

$$M_y = w[\sigma_{YSG}\frac{t_s^2}{2} + (\sigma_{YSI} - \sigma_{YSG})\frac{t_s^2}{3}] + w[\sigma_{YCI}(t_c)(\frac{t_s}{2} + \frac{t_c}{6}) + \sigma_{YCG}(t_c)(\frac{t_s}{2} + \frac{t_c}{3})] \qquad \text{Equation 4.7}$$

Where w is the width of both the coating and substrate, $\overline{M}$ is the bending moment at the gauge location resulted by the applied load P, t_s and t_c are the thickness of the substrate and the coating respectively, ε_{XCG} and ε_{YCG} are the longitudinal and respective traverse strain gauge readings on the coating, ε_{XSG} and ε_{YSG} are the longitudinal and respective traverse strain gauge reading on the substrate, ε_{XCI} and ε_{YCI} are the longitudinal and respective traverse strain at the coating interface, ε_{XSI} and ε_{YSI} are the longitudinal and respective traverse strain at the substrate interface,

σ_{XCG} and σ_{YCG} are the longitudinal and respective traverse stress gauge reading on the coating, σ_{XSG} and σ_{YSG} are the longitudinal and respective traverse stress gauge reading on the substrate, σ_{XCI} and σ_{YCI} are the longitudinal and respective traverse stress at the coating interface, σ_{XSI} and σ_{YSI} are the longitudinal and respective traverse stress at the substrate interface.

The surface stresses, σ_{CG} and σ_{SG} are related to the strains and the mechanical properties of the coating and substrate from the following:

$$\sigma_{XCG} = \frac{E_c}{(1-\nu_c^2)}(\varepsilon_{XCG} + \nu_c \varepsilon_{YCG}) \qquad \text{Equation 4.8}$$

$$\sigma_{XSG} = \frac{E_s}{(1-\nu_s^2)}(\varepsilon_{XSG} + \nu_s \varepsilon_{YSG}) \qquad \text{Equation 4.9}$$

where ν_s and ν_c are the Poisson's ratio for the substrate and coating respectively, E_s and E_c are the Young's modulus for the substrate and coating respectively, the surface strains, ε_{XCG}, ε_{YCG}, ε_{XSG} and ε_{YSG} are measured with the strain gauges. The interface stresses can be calculated from:

$$\sigma_{XCI} = \frac{E_c}{(1-\nu_c^2)}(\varepsilon_{XCI} + \nu_c \varepsilon_{YCI}) \qquad \text{Equation 4.10}$$

$$\sigma_{XSI} = \frac{E_s}{(1-\nu_s^2)}(\varepsilon_{XSI} + \nu_s \varepsilon_{YSI}) \qquad \text{Equation 4.11}$$

Where the interface strains, ε_{XCI}, ε_{YCI}, ε_{XSI} and ε_{YSI} can be found from the assumption of a linear strain distribution from the surface strains, see Figure 4.21. Tests were carried out on coated (NiCrSiB) mild steel substrates, then two of the four equilibrium equations were used to solve the stiffness and Poisson's ratio of the coating.

4.7.2 Other Methods

There are other techniques used to measure the stiffness of a coating, such as the three or four point bend test, indentation test or the curved specimen deflection test. However none of these tests were used in the research. In the three/four point experimental bend test, the coated or free-standing sample is placed on two knife edges and force is applied through a third knife edge (three point test) or two knife edges (four point test). The bend test can be monitored acoustically to detect the crack formation (especially for brittle ceramic coatings) [108]. The elastic modulus is found from the applied load and the deflection measured when the deposit fails.

The indentation test and the curved specimen deflection test are two Young's modulus measurement techniques, used to determine the parameter in both the perpendicular and parallel directions respectively [109]. The indentation test involves, drawing a diamond hemispherical indentor with known radius across the coating surface. After scratching under various loads, the depth of scar is measured by a stylus (used to measure surface roughness). The radius of contact between the indentor and the coating surface, together with Hertz's contact theory, calculates the Young's modulus perpendicular to the coating plane [109]. The measurement process for Young's modulus parallel to the coating plane, involves spraying a cylindrical stand-alone component. The component is compressed in the radial direction where the load is measured. Using this technique, the Young's modulus is measured in accordance to the deflection of a curved beam theory.

4.8 RESIDUAL STRESS

4.8.1 The Hole Drilling Method

Residual stress may be measured using the hole-drilling method, which is one of the most widely used modern techniques. This method [110, 111] involves evaluating residual stresses near the surface of a specimen by drilling a small hole and measuring the relieved strains in the surrounding material.

The procedures of the hole-drilling residual stress measurement operation are listed as [111]:

i. A special strain gage rosette (three grids) is bonded at the point where residual stresses are to be determined;
ii. Each grid is connected to a switch-and-balance unit and strain indicator;
iii. The RS-200 Milling Guide is attached to the test part and centred over the rosette;
iv. A precision hole is introduced at the centre of the rosette;
v. Readings of the relaxed strains (residual strain) are recorded;
vi. Residual stresses are computed.

The hole drilling method is "semi-destructive" as localised damage is made to the coating surface and the small hole drilled does not significantly affect the structural integrity of the specimen. In the experiments, the strains are measured with a three-element strain gauge rosette EA-06-062RE-120, which has been shown in Figure 4.22.

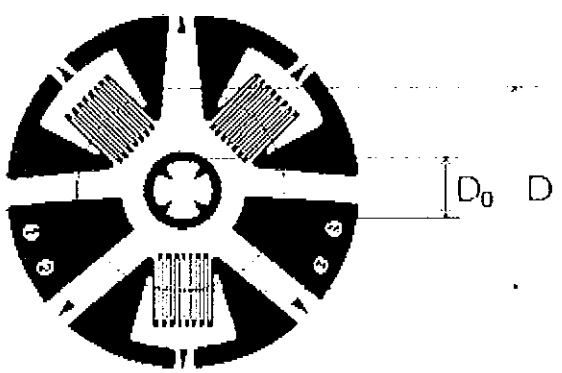

Figure 4.22. Strain Gauge Rosette for the Hold Drilling Method

This rosette consists of three precision strain gauges, which are constructed of self-temperature-compensated foil on a flexible polyimide carrier and incorporate a centering target for use with a precision milling guide. Their characteristics are listed in Table 4.8.

Characteristics	Values
Resistance in Ohms at 24 °C	120.0 ± 0.2%
Nominal gauge factor at 24 °C	2.09 ± 1.0%
Temperature range	–75 °C ~ +175 °C
Strain limits	3%

Table 4.8. Characteristics of the Strain Gauge Rosette for the Experiments

The rosette strain gauge measures strain in three directions, 0°, 45° and 90° (or 0°, 60° and 120°), as described in ASTM E1561 [112] while the central region is cut away.

The rosette consists of three radially oriented gauges with their centres at the strain gauge circle with diameter D. The rosettes have the grid center line diameter of 5.13mm and the length of each strain gage is 1.57mm. The diameter of the drilled hole, D_0, should be related to the diameter of the gauge circle by

$$0.3 < \frac{D_0}{D} < 0.5$$

Milling was carried out until the depth of the milled hole was equal to a distance of 0.4 of the mean gauge circle diameter (D), to ensure total relaxation of residual stress, or through the thickness, where the total thickness is less than $1.2D$.

Residual stress was calculated using Kirsch's Theory [113]. In order to accurately measure the strain, some hypotheses have been made:

i. The milled hole is concentric with the rosette
ii. The coating is an isotropic and linear elastic material
iii. The main tension direction is constant along its depth, and the tension which is perpendicular to the surface is assumed to be negligible

The equations (4.12 ~ 4.14) that were used to calculate residual stress in the material are specified by ASTM E837-96 [110]. The strain values ε_1, ε_2 and ε_3 were measured from the gauge 1, 2 and 3 respectively.

$$\sigma_{\min}, \sigma_{\max} = \frac{\varepsilon_3 + \varepsilon_1}{4A} \pm \frac{\sqrt{(\varepsilon_3 - \varepsilon_1)^2 + (\varepsilon_3 + \varepsilon_1 - 2\varepsilon_2)^2}}{4B} \quad \text{Equation 4.12}$$

Where

$$A = -\frac{1+\nu}{2E} \times \bar{a} \quad \text{Equation 4.13}$$

$$B = -\frac{1}{2E} \times \bar{b} \quad \text{Equation 4.14}$$

and

$$\tan 2\alpha = \frac{\varepsilon_3 + \varepsilon_1 - 2\varepsilon_2}{\varepsilon_3 - \varepsilon_1} \quad \text{Equation 4.15}$$

E and ν are the Young's modulus and Poisson's ratio respectively for the coating. $\bar{a}$ and $\bar{b}$ are dimensionless, material-independent coefficients, which depend on the depth of drilling Z. Value of $\bar{a}$ and $\bar{b}$ can be found from Figure A6 in Appendix I.

The coating surface was thoroughly prepared before the gauge is attached on the test piece. Preparations included thoroughly degreasing the gauging area with diluted hydrochloric acid and dry abrading the coating surface with a fine silicon-carbide paper to remove any surface contaminations, followed by *RS 180-803* solvent cleaner to do the final cleaning. An adhesive was then used to bond the gauge to the surface. The soldering points on the gauge surface were then rubbed away the attaching film and also to ensure the solder adheres the surface. The test is then carried out by connecting the strain gauge to a strain-recording instrument. The hole is drilled through the coating/deposit via the central region of the strain gauge to relax the residual stress in the material being measured.

The RS-200 Milling Guide [111] was used in the experiment. It is a high precision instrument for residual stress analysis by the hole drilling method. A tungsten carbide precision cutter, powered by a high-speed air turbine unit (up to 400,000rpm), was used to mill the hole. Before drilling, a microscope was installed to align the device

visually. After a precision hole is introduced at the centre of the rosette and the readings of the relaxed strains are recorded, residual stresses are calculated.

4.8.2 Curvature Method (Clyne's Analytical Method)

In most of the coating processes, residual stresses arise from two main sources: in addition to the stresses caused by thermal contraction, there are the quenching stresses developed during the deposition process. Since the interest in the research lies in the stress level which are generated within the surface coating, it is necessary to consider the situation in terms of misfit strains. In the literature, Tsui and Clyne [114] used an analytical method which considers a pair of plates bonded together with a misfit strain $\Delta\varepsilon$ in the x-direction as shown in Figure 4.23. The stress distributions were found for misfit strain of the two-layer system, which only composed of the coating and the substrate, using the following expressions [114, 115]:

Stress at the top of the coating:

$$\sigma_c \mid_{y=h_c} = -\Delta\varepsilon\left(\frac{E'_c h_s E'_s}{h_c E'_c + h_s E'_s}\right) + E'_c k(h_c - \delta) \qquad \text{Equation 4.16}$$

Stress at the bottom of the coating:

$$\sigma_c \mid_{y=0} = -\Delta\varepsilon\left(\frac{E'_c h_s E'_s}{h_c E'_c + h_s E'_s}\right) - E'_c k\delta \qquad \text{Equation 4.17}$$

Stress at the top of the substrate:

$$\sigma_s \mid_{y=0} = \Delta\varepsilon\left(\frac{E'_c h_c E'_s}{h_c E'_c + h_s E'_s}\right) - E'_s k\delta \qquad \text{Equation 4.18}$$

Stress at the bottom of the substrate:

$$\sigma_c \mid_{y=-h_s} = -\Delta\varepsilon\left(\frac{E'_c h_c E'_s}{h_c E'_c + h_s E'_s}\right) - E'_s k(h_s + \delta) \qquad \text{Equation 4.19}$$

Where σ_c and σ_s are the respective stresses in the coating and substrate, h_c and h_s are the thickness of the coating and the substrate. k is the curvature of the beam and δ is the overall deflection of the beam. $\Delta\varepsilon$ is given as:

$$\Delta\varepsilon = (\alpha_s - \alpha_c)\Delta T \qquad \text{Equation 4.20}$$

Where α_c and α_s are the respective coefficients of thermal expansions for the coating and substrate, and ΔT is the difference in temperature during cooling. E'_c and E'_s are given as follows:

$$E'_c = \frac{E_c}{(1-\nu_c)} \qquad \text{Equation 4.21}$$

$$E'_s = \frac{E_s}{(1-\nu_s)} \qquad \text{Equation 4.22}$$

Where E_c and E_s are the respective coating and substrate stiffnesses. ν_c and ν_s are the respective Poisson's ratios of the coating and the substrate.

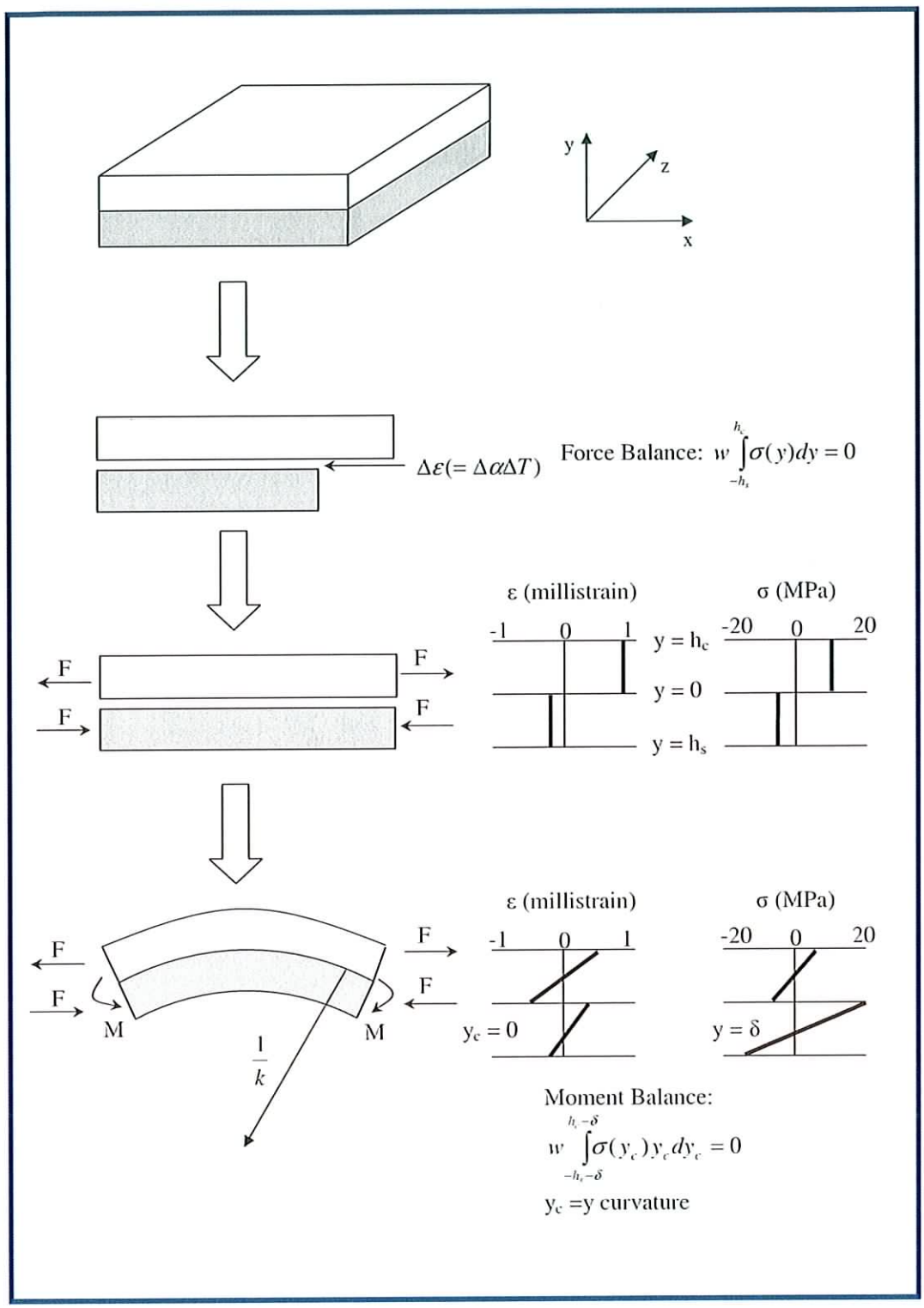

Figure 4.23. Schematic Description of the Generation of Curvature in a Flat Bi-material Plate as a Result of Misfit Strain, Adapted from [114]

In the research, this curvature method – Clyne's method was used to measure residual stress in the coating, as it is a fast measurement method compared with other techniques such as X- ray diffraction and hole drilling method.

In the Clyne's method, a mild steel plate sample is deposited with NiCrSiB using the standard procedures that were presented in Chapter 4.1.4. After the coating process, the deflection of the sample was measured using the dial gauge method that was presented in Chapter 4.5.1, and as shown in Figure 4.16. The distributed stresses were deduced by using Equations 4.16 to 4.19.

4.9 ESPSI SYSTEM SETUP

4.9.1 ESPSI System with Michelson Type Shearing Device

The shearography technique registers the speckle interferences by a CCD camera. It compares the information before and after loading by means of a digital technique, and presents the results directly on a monitor. Figure 4.24 shows a schematic diagram of a shearography system.

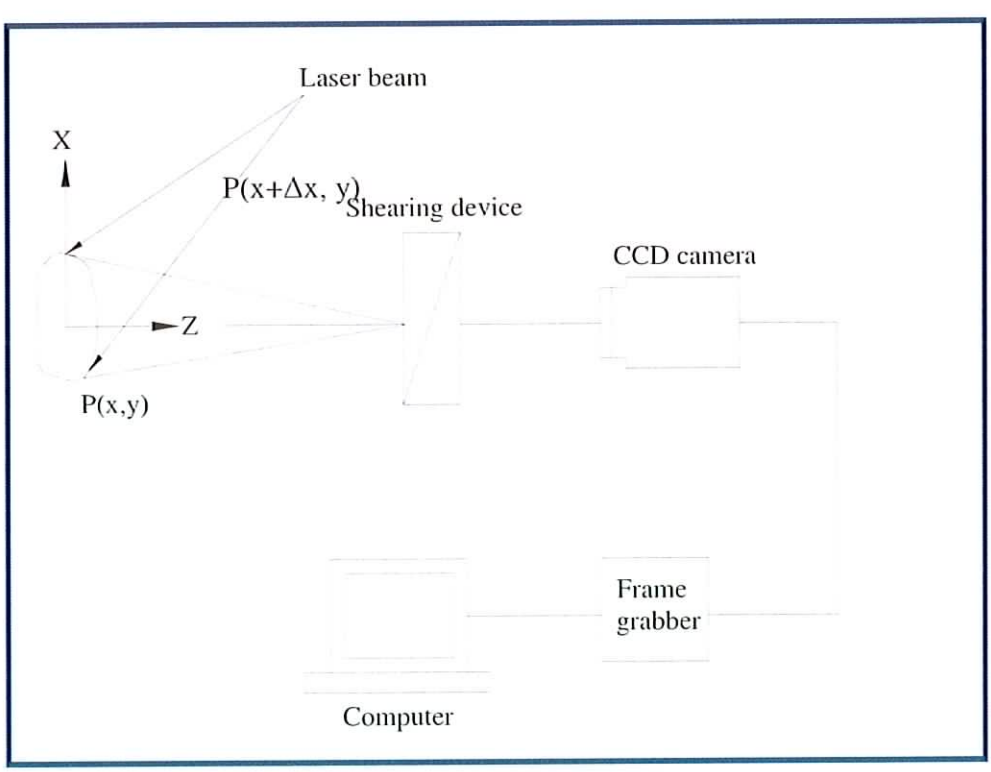

Figure 4.24. Schematic Diagram of a Shearography System

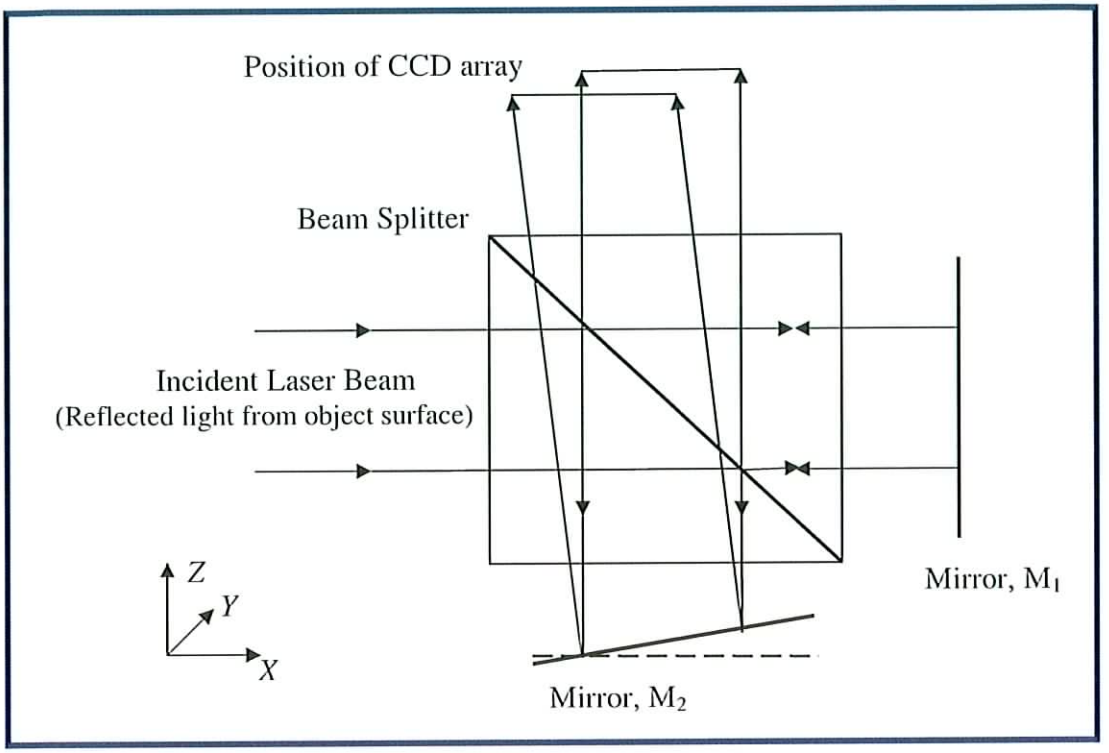

Figure 4.25. Modified Michelson Interferometer

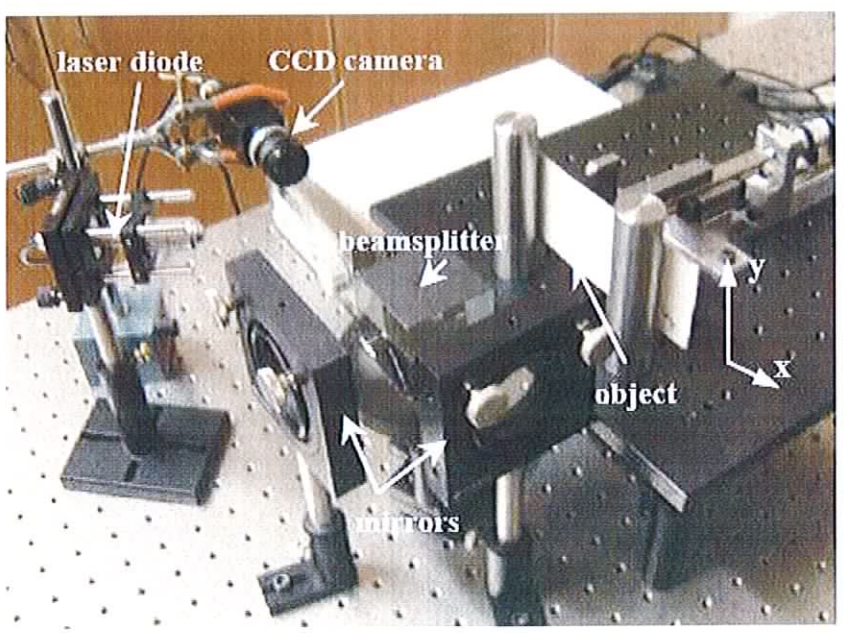

Figure 4.26. Shearography System (Michelson Type) used in the Experiment

The shearing component used in the experiment is a modified type of Michelson interferometer, as shown in Figure 4.25. In this modified Michelson type interferometer, one of the mirrors is slightly tilted to produce a lateral shift between the two speckle patterns. The object is illuminated by a collimated beam lying in the *xz* plane and making an angle with the normal of the surface, and then the reflected light was split by the beamsplitter and imaged by a CCD camera. This interferometer has been used to observe fringes depicting slope change contours in the configuration of angle is zero degree [92]. Figure 4.26 [116] showed the picture of the ESPSI system used in the experiment (Michelson type).

4.9.2 ESPSI System with Two Glass Plates as Shearing Device

A He-Ne laser with wavelength of 633nm and maximum power of 20mW was used as the light source in the experiment. The test object was illuminated by the laser beam at an angle to the normal of the object surface. The two images of the tested object are formed by reflection from the shearing device and they are imaged by a CCD camera. The shearing device used in this system consists of two glass plates (Figure 4.27) with refection coefficients of the coatings 0.3 and 0.7 respectively [117]. One of the mirrors is slightly tilted to produce a lateral shear. The resultant speckle patterns are produced by digital subtraction of the speckled images of the object before and after deformation. Then the light intensity of the resultant speckle patterns was converted to an electronic video signal. This signal was sent to an analogue-to-digital converter and to yield a digital picture made up of 512 x 512 sample points. Each point was quantised to 256 discrete grey levels. The frame memory is able to repetitively store frames at the camera rate of 1/30 of a second.

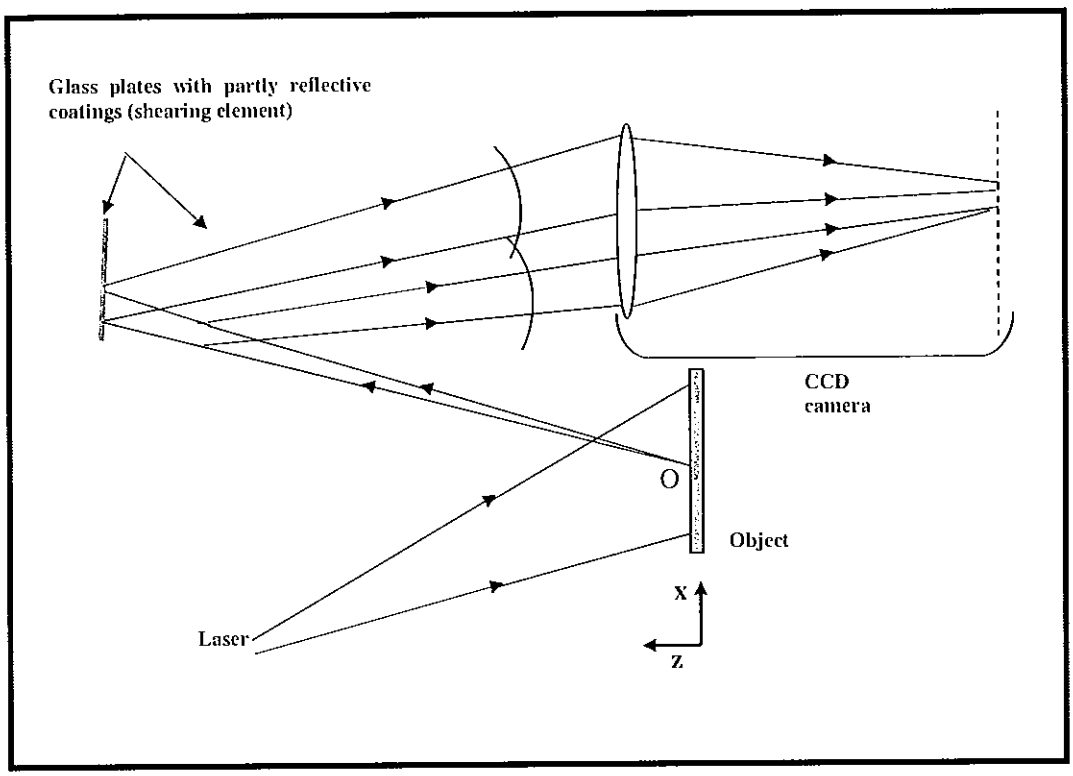

Figure 4.27. ESPSI Arrangement of Using Two Glass Plates as Shearing Device

The experiments were carried out in a dark room since direct light from lamps will greatly reduce the fringe contrast. To alternatively overcome this influence, a filter piece can be arranged in front of the CCD array so that only a wavelength in the neighborhood of the laser light could pass, therefore to enable the investigation being carried out in a bright workshop or production hall [76].

Also, the investigations were performed in a relatively quiet environment. Despite shearography being relatively insensitive to slight rigid-body motions and well suited for field testing, it is still sensitive to a large rigid-body motion. This motion can lead to speckle decorrelation, which reduces the fringe contrast and stability and eventually leads to a complete loss of fringes if the extent of the decorrelation is greater than the speckle size [76].

4.9.3 Loading Methods for Defects Detection

The flaw detection by shearography is based on the comparison of two states of deformation (before and after) in the object. Therefore, in order to detect the presence of the surface coating defects, a localised displacement field is required to

be induced. In the literature, there are various stressing methods that can be used depending on the type of material and the defects being investigated, such as pressurisation, partial vacuum stressing, thermal stressing and vibration, as described by Hung [15].

4.9.3.1 Three Point Bending

In the experiments, two stressing methods were employed: three-point bending and thermal stressing. A three-point bending test rig, as shown in Figure 4.28 [116], was designed and constructed for conduct the mechanical stressing. This rig is able to measure the deformation of the metal samples in the sub-micrometer range and it satisfies the requirement of controlling the bending deformation on the coated sample surface precisely for shearography [116]. The purpose of the arrangement is to compare the changes in shearographic fringe patterns on the sample surface with predetermined displacements.

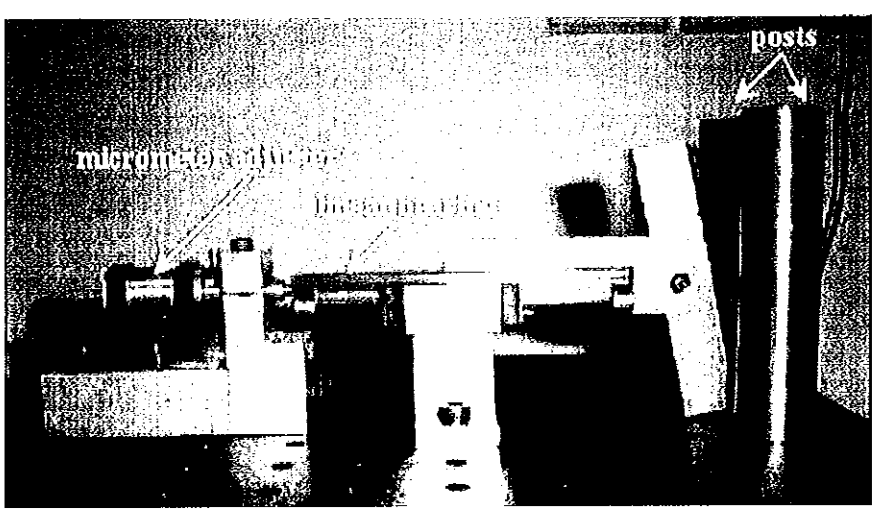

Figure 4.28. Picture of the Three-Point Bending Test Rig

Due to the sensitivity of the shearographic system, a means of producing deflections in the samples of the order of 10^{-7} m is required. This is achieved using a test rig which consists of a micrometer adjuster, a linear bearing, a knife edged push rod and two retaining posts, all mounted on an optical table. The micrometer adjuster used is an *Elliot Martock MDE 216* type, which provides 8mm of coarse adjustment with a resolution of 1 micron along with 0.3mm of fine adjustment with a resolution of

20nm. This enables the required control of the linear translation. The output from the micrometer is transferred to the centre of the sample via a linear bearing which has a knife edge mounted on the opposite end to that with which the micrometer is in contact. The linear bearing ensures that the load is applied centrally to the sample and also prevents all movements other than that parallel to the micrometer axis [116].

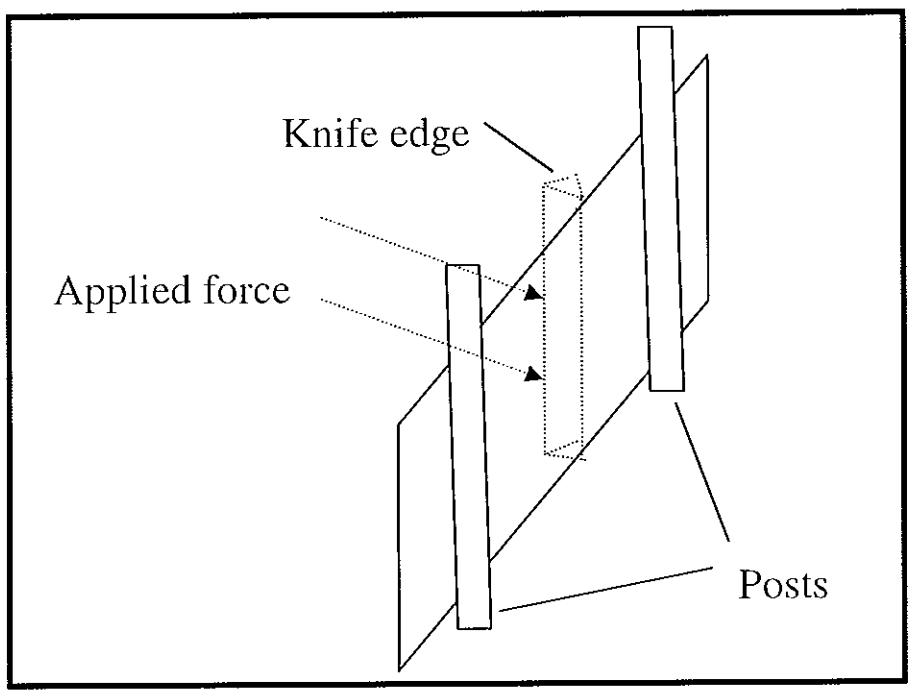

Figure 4.29. Principle of the Three-point Bending Test Rig Knife Edge Applies Load on the Sample

The knife-edge is mounted on the linear bearing by means of a horizontal pivot, which ensures that full and even contact in the vertical axis is achieved when a load is applied to the rear surface of the sample, as shown in Figure 4.29. The posts which used to withstand the bending of sample are two 25mm diameter stainless steel, and they are mounted on the optical table using 6mm studs. Dimensions for the sample thickness and post diameters were carefully chosen to ensure that measured movement at the sample surface is, as small as possible, compared to the deflection of the retaining posts. This is to maximise the bending effects in the sample and minimise the effects of the deflection in the retaining posts.

4.9.3.2 Thermal Stressing

The thermal stressing method was also used in the investigation. The temperature gradient induces thermal stresses in the object. If delaminations, non-adhesion, or microcracks exist in the object, anomalies or interruptions of the fringes appear in the real time shearogram at the position of the flaws.

The thermal stressing method is well suited for detecting the microcracks in the composite laminates and disbands between a cover plate and honeycomb structure, and it is also used to test compound materials and sintered metals [76].

Two approaches were made to thermally stress the samples through: attaching the back of the surface using a solder iron, and illuminating the coating surface by using a lamp. The field of view was 30mm×20mm in all experiments (Figure 4.30). It was assumed in the experiments that the lateral shearing is in x direction only, and there will be no shearing in the y direction.

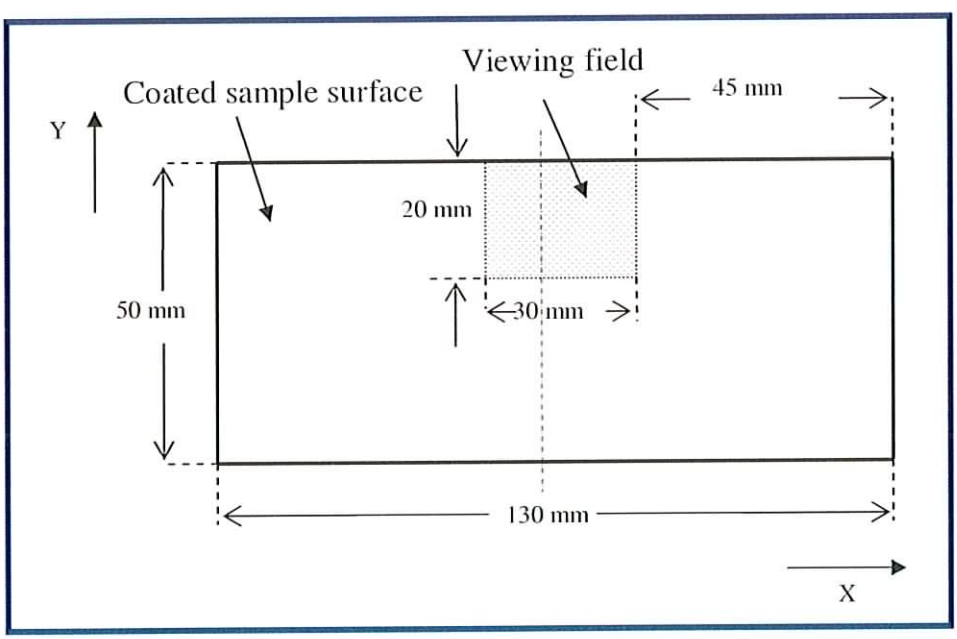

Figure 4.30. Viewing Area on the Coated Sample

Chapter 5 – Results and Discussion

5.1 INTRODUCTION

In this chapter, experimental results and discussion of thermal spray processes and coating evaluations are presented. The objectives of this project were to investigate the thermal spraying coating processes, characterise coating properties (mechanical methods and optical methods) and use the optical interferometric method to detect coating defects.

Feasibility studies on the application of metal alloy coatings on various types of substrate materials using SUPERJET spray process have been completed. Investigations were carried out on steel, copper, aluminium and polymer substrates. However, the results show that only the steel substrate is suitable for the SUPERJET process. None of the other materials (copper, aluminium and plastic) is suitable as substrate material. In the SUPERJET process, the coating material is melted or fused during the fusing process. Therefore, the coating material has to possess lower melting point than the substrate material. This is owing to the fact that if the substrate melts before the coating, it will be deformed and the shape of the substrate will be destroyed. Copper has a lower melting point (1083°C) than the alloy material NiCrSiB (1175°C) used in the experiments. Aluminium and plastic have even lower melting points. Steel (e.g. low carbon steel, stainless steel), which has a melting point greater than 1370°C, is the most suitable and commonly used material for SUPERJET process. In this research work, low carbon steels were used as substrates for all the coating samples.

The results are categorised in the following three parts:

1. Investigation of thermal spraying coating processes

    i. Temperature
    ii. Distance
    iii. Coating Defects

2. Surface coating characterisation by mechanical methods

    i. Coating thickness
    ii. Coating microstructure analysis
    iii. Hardness measurement
    iv. Surface roughness measurement
    v. Elastic properties measurement of coatings
    vi. Residual stresses measurement

3. Optical characterisation of thermal sprayed coatings

    i. Surface roughness measurement using WLI
    ii. Comparison between mechanical and optical measurements
    iii. Defect detection using Electronic Speckle Pattern Shearing Interferometry

5.2 INVESTIGATIONS OF THERMAL SPRAYING COATING PROCESS

5.2.1 Temperature Measurement

Temperature control in the SUPERJET spraying process is a key factor that influences the success of the coating deposition. A recommendation for spraying temperature is necessary. In the experiment, the temperatures were measured during thermal spraying by a thermocouple that was attached to the surface of the sample being coated.

The temperature can be easily measured for the preheating and fusing process. Simply attach the thermocouple under the spray zone and the temperature values can be obtained from the reading of a thermocouple converter. However, during the spraying process, measurement can be difficult to carry out. Incorrect readings will be recorded when the sprayed powders coat the surface of the thermocouple. Therefore, the temperature measurement was made at the area immediately after the spraying.

Figure 5.1 shows the temperature calibration graph for thermocouple measurement. Sample 1 and sample 2 have different substrate thicknesses, which are 3mm and 6mm respectively. The deposited coating powder for both of the samples is 10185 (Bronzochrom). The samples were coated following the procedures recommended by the supplier [12].

Inaccuracy may occur during the spraying temperature measurement due to the assembly method of the thermocouple. Since the measurement is only made after the spraying but not simultaneously, there might be heat loss during the period between.

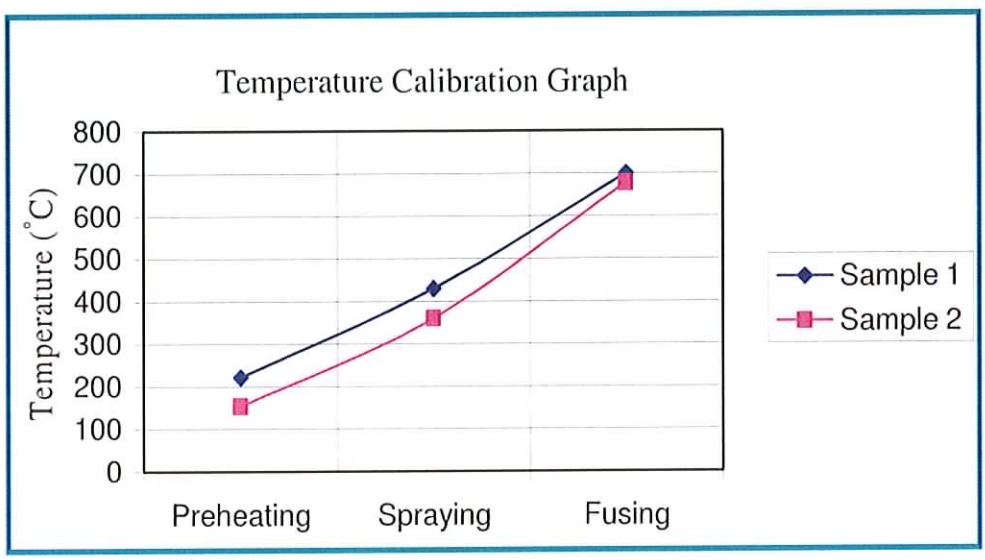

Figure 5.1. Temperature Calibration Graph for Thermocouple Measurement

5.2.2 Spraying Distance

During the SUPERJET process, the distance between the torch and the sample has to be altered and controlled for each individual step (preheating, spraying and fusing). Figure 5.2 shows the optimum distance for each process.

It is not very easy to control the exact distances during spraying. Unlike the CDS-8000 process that can be integrated into an assembly with automated operations, the SUPERJET process can only be handled by hand. However from the obtained results (Figure 5.2), it can be understood that the distance may be altered within the allowed tolerance, and this will not affect the coatings' quality.

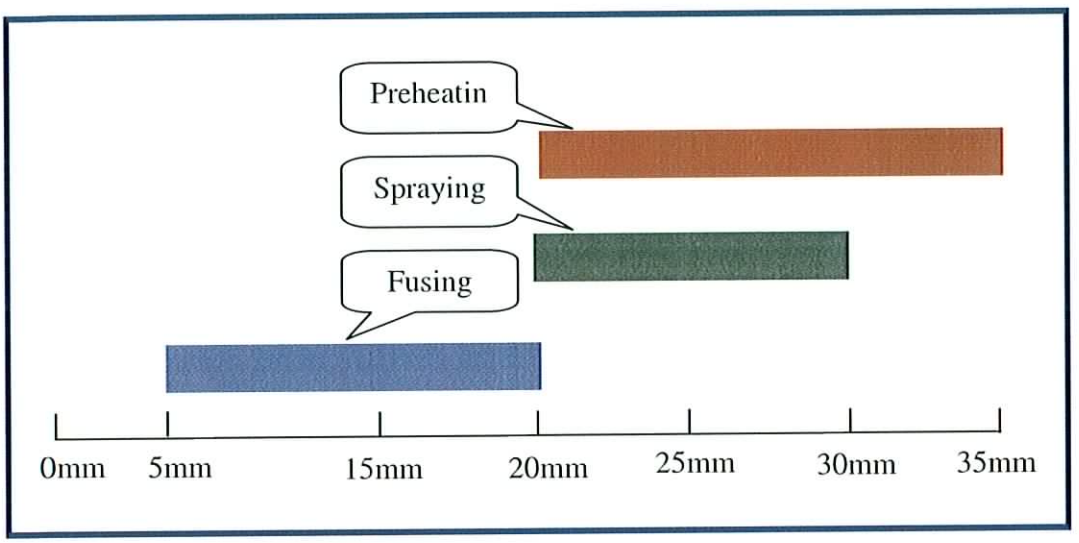

Figure 5.2. Distance (from the Gun Tip to the Substrate Surface) used in the Individual Process

5.2.3 Defects of Coatings

One of the objectives of this project is to detect defects within the thermal sprayed coatings using the ESPSI technique. Therefore, defective coatings are desired as the samples for the investigations. The nature and the characteristics of coating defects are analysed and concluded in Figure 5.3.

Most sprayed deposits have pores arising from shrinkage and degassing after deposition. Shrinkage gives acicular shaped pores, degassing gives more rounded pores. Oxide inclusions can arise from pick-up during spraying. Poor surface preparation will result in poor coating adhesion. Any traces of oil or grease or polishing debris on the surface of the substrate metal or in the coating material will tend to prevent the coating from adhering properly to the substrate. For nickel base alloy coatings, one of the reasons leading to poor adhesion is that the coating requires a temperature of 1000 °C minimum at the interface. Therefore, if the temperature in the substrate is too low, the coating may be fused but may not be bonded to the substrate.

Various defects are found in the thermal sprayed coatings, including:

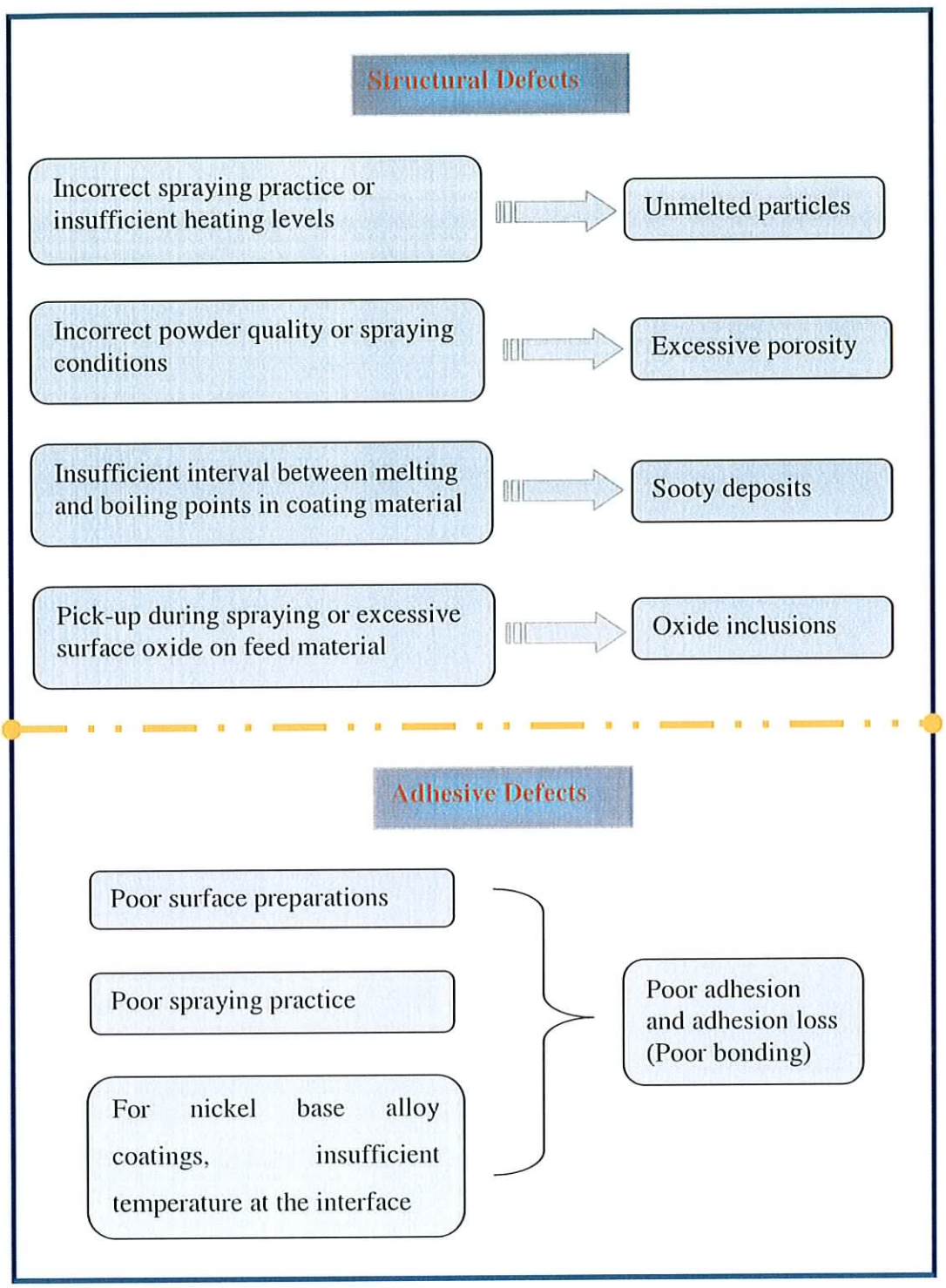

Figure 5.3. Summarised Coating Defects Found from the Experiments, adapted from [3]

Figure 5.4 shows examples of adhesive defects, including coating adhesion loss and coating detachment from the steel substrate.

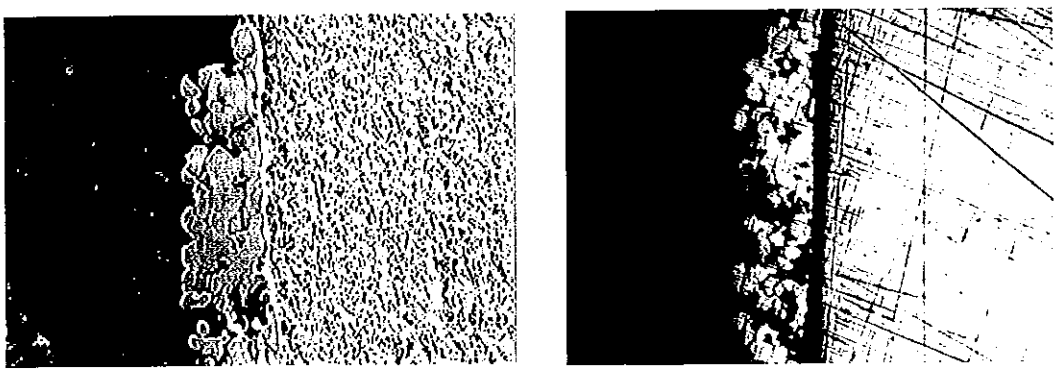

(a) (b)

Figure 5.4. Examples of Adhesive Defects, (a) Adhesion Loss; (b) Coating Detachment and Adhesion Loss

Other defects include the extremes of the coating thickness. If the coating thickness is too thin, a film may tend to contain pinholes. Contrarily, if the film is too thick, the coating surface will tend to be uneven.

5.3 MECHAINCAL MEASUREMENTS AND COATING CHARACTERISATION

5.3.1 Coating Thickness Measurement

Coating thickness measurement is an important procedure in this research work. The selection of the equipment depends on whether the thickness is of the order of micron or of the millimetre range. Since the coating thickness is in the range of hundreds of microns, the thicknesses of the coatings were measured by two methods: dial gauge method and microscopic method. Figure 5.5 shows the results of the coating thickness measurements of four samples.

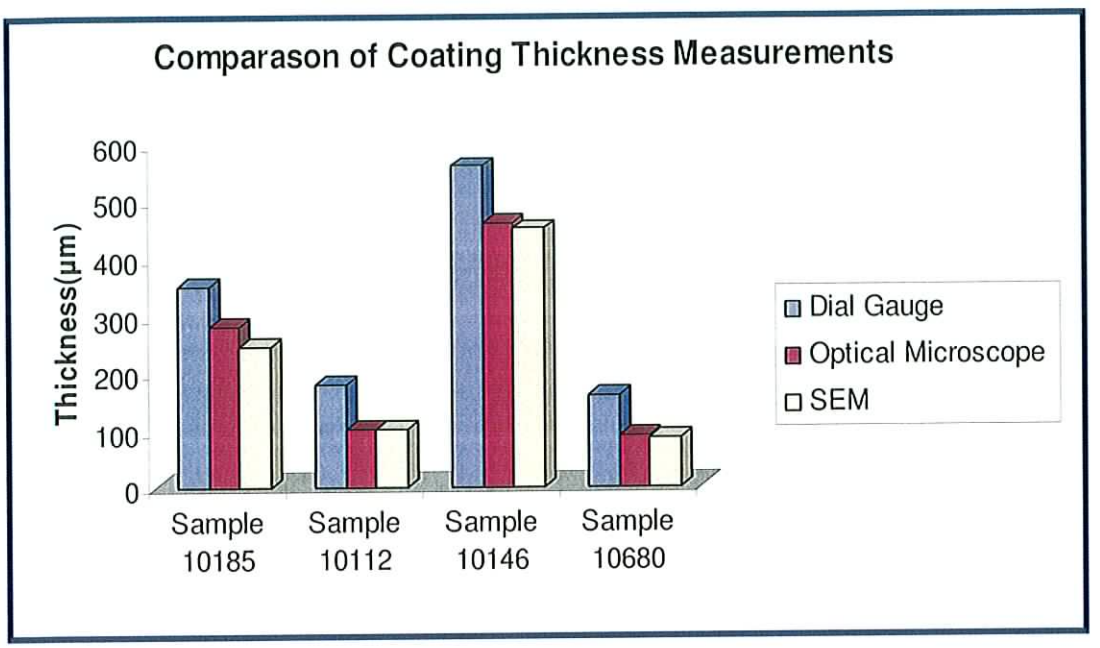

Figure 5.5. Comparison of Coating Thickness Measurement Results

The dial gauge method used for the measurement of the thickness has been stated in Chapter 4.5.1, and it is the result from the comparison between the measurement of thickness of the sample before and after coating deposition process. The optical measurement method was carried out using a very precisely calibrated scale on the recorded image. A line was drawn connecting two points from the coating/substrate interface to the end of the coating. The distance between these two points is the thickness of the coating. Computer software was then used to digitise the measured value. From the comparison between the results obtained from the dial gauge measurement and optical measurements (Figure 5.5), dial gauge method have results about 70µm ~ 100µm greater than optical measurements results, which is 18% ~ 44% of their own measurement results. It is known that microscopic method is very precise and reliable, therefore, the dial gauge method is not sufficiently accurate for measuring the coating thickness, especially in the range under 1mm. Using optical microscope and SEM give very similar result values.

From the pictures obtained from the microscopic studies, uneven coating thickness was found in some samples. An example is shown in Figure 5.6, it can be seen that the edge of the coating and the interface of the coating/substrate have an irregular profile. Since the samples were produced by SUPERJET spray process, and the spray

gun was hand-held during the spraying process, errors are inevitable. Therefore the deposited coating would have a variable thickness.

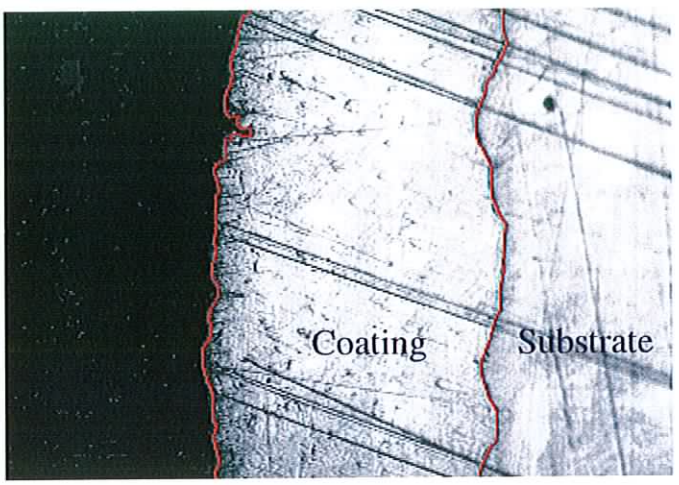

Figure 5.6. Uneven Coating Thickness Produced by SUPERJET Process

5.3.2 Microstructure Analysis

Microstructure analysis of the coating samples was carried out in this research work. Images were obtained both from optical microscopic studies and scanning electron microscopic studies. Sample surface preparations proved very necessary before the investigations. Figure 5.7 shows a picture of the steel substrate without preparation, and it is not possible to carry out investigation on the sample.

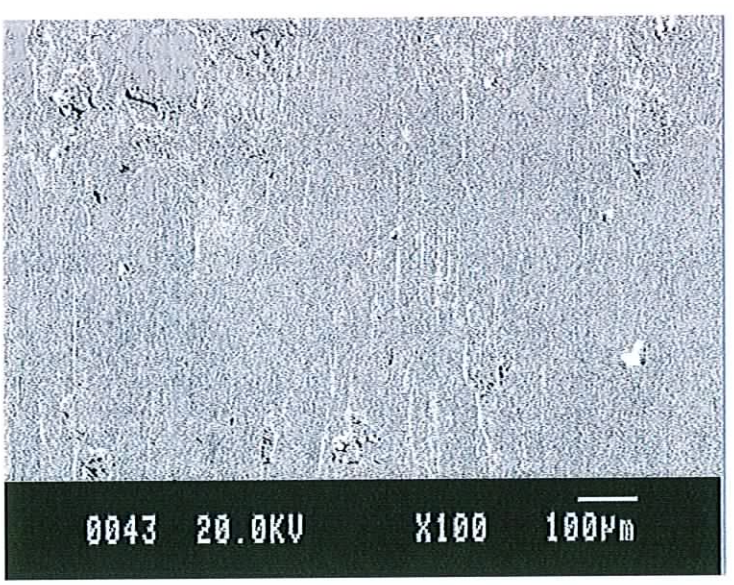

Figure 5.7. Steel Substrate without Surface Preparations (SEM)

Figure 5.8 shows the microstructures of four coating samples which were obtained using optical microscope.

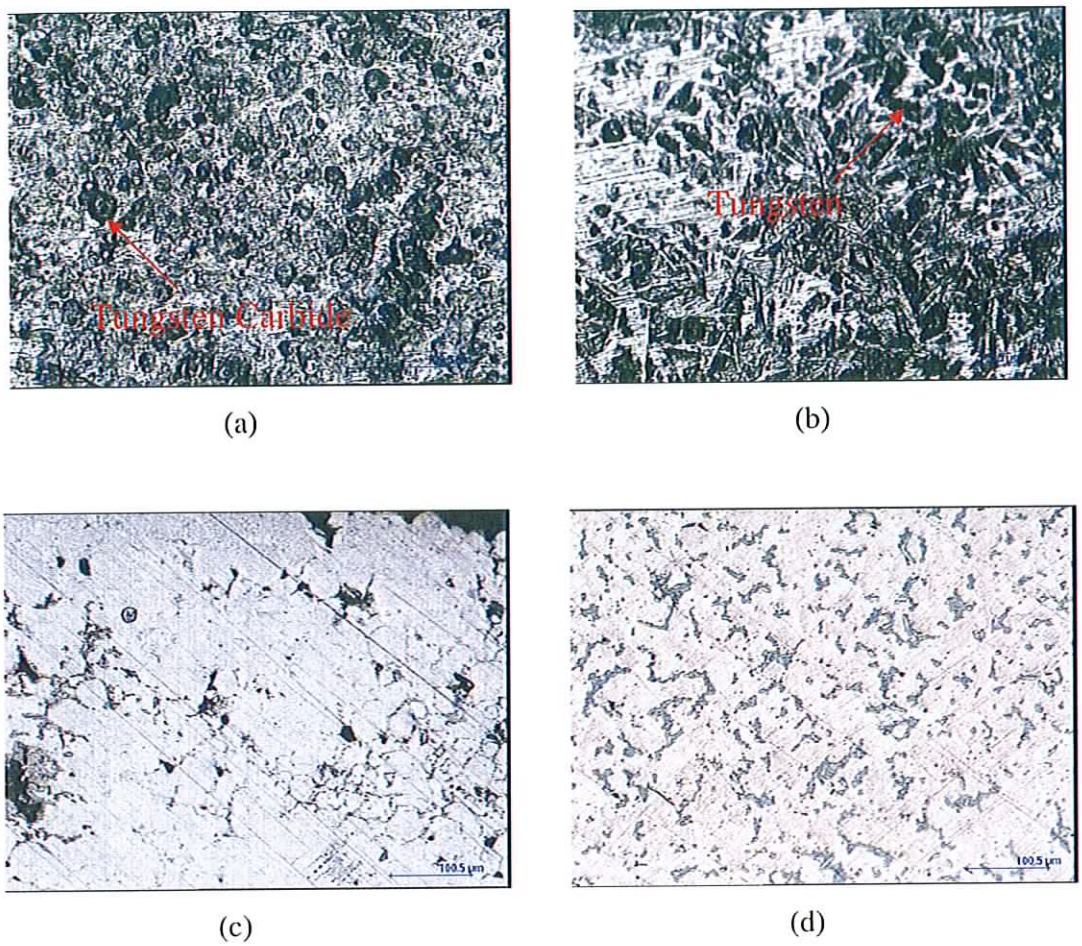

(a) (b)

(c) (d)

Figure 5.8. Microstructure of Coating Surface (100×): (a) Coating Sample 10011; (b) Coating Sample 10092; (c) Coating Sample 10185; (d) Coating Sample 10146.

In Figure 5.8 (a), the grain boundary was participated with some of the dark grey constituents of the alloy material. The black angularly rounded shape particles in Figure 5.8 (a) were identified as Tungsten Carbide. The greyish white triangular constituents can be seen in Figure 5.8 (b), which matched the structural appearance of Tungsten alloy. Figure 5.8 (d) showed that the surface was a large aggregate of pale blue constituents evenly spread in the structure. Considerable amounts of porosity can be identified under the microscopic studies. It is the nature of this coating process to produce porosity. The porosity may have the benefit of allowing thicker coating to be applied, as residual stresses in porous coatings tend to be lower [14].

SEM was also used for coating microstructure analysis. SEM images of the top of the thermal sprayed coating 10185 and 10680 have been shown in Figure 5.9.

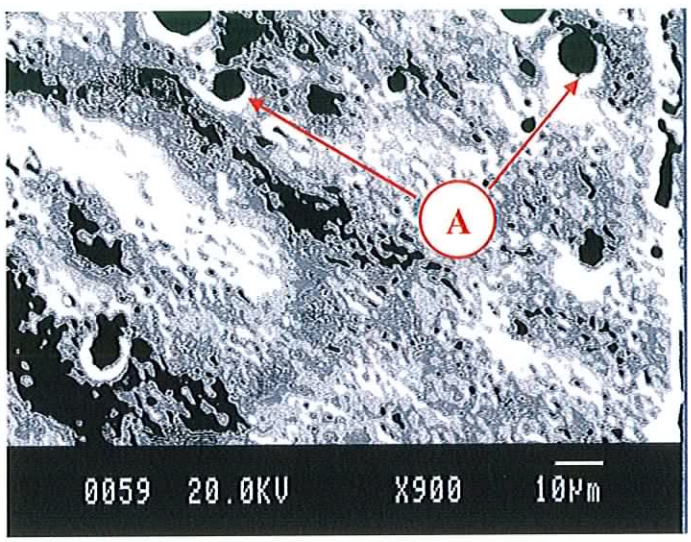

(a)

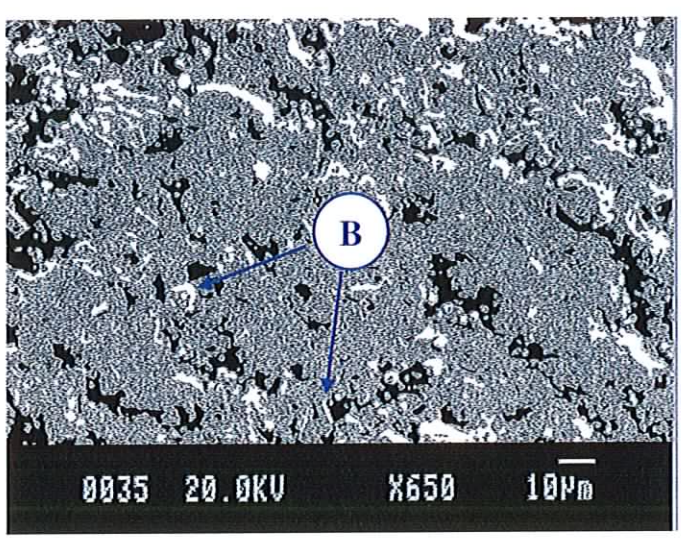

(b)

Figure 5.9. Scanning Electron Microscopic Surface Images of SUPERJET Sprayed Coatings, (a) 10185; (b) 10680. A = Air Pores, B = Un-melted Particles.

It can be seen from Figure 5.9 (a) that the coating sample 10185 has an uneven surface with hills and valleys. This is due to the fusing process actually melting the coating together with the substrate. When the coating solidifies from the molten state to form a solid surface it results in irregularities on the surface in terms of flatness. Also, a considerable amount of air pores were found on the surface. This can be

understood because this is the nature of the thermal spraying process. Unmelted material particles were found from Figure 5.9 (b) on sample 10680. Figures 5.10 (a) and (b) show the SEM images of the coating and the substrate of sample 10112 and 10146 respectively.

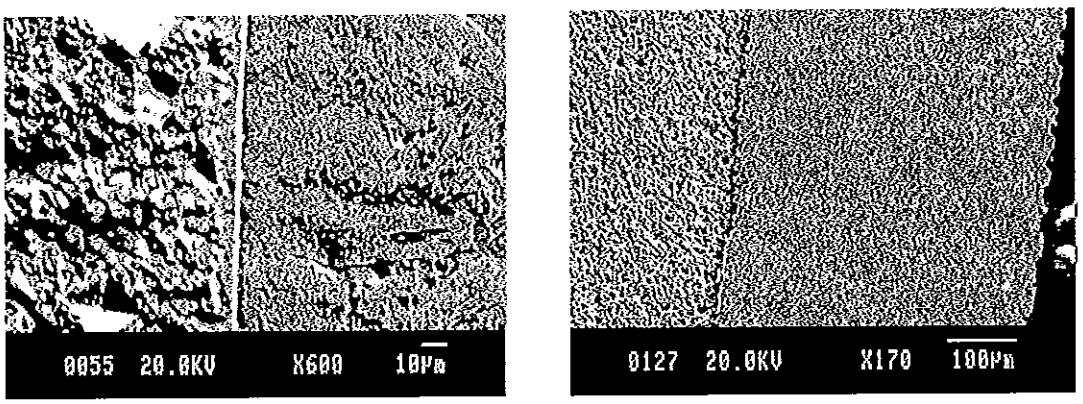

(a) (b)

Figure 5.10. SEM Images of Coating and the Substrate, (a) 10112; (b) 10146

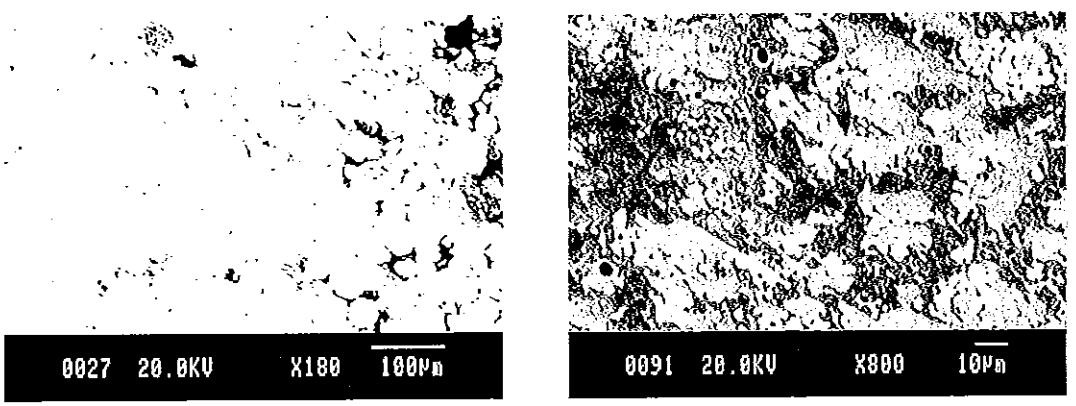

(a) (b)

Figure 5.11. SEM Images of Coating 10185, (a) Without Etching; (b) With Etching

Etching is important in some of the SEM studies of surface coatings. Without etching, small differences in reflectivity cannot be recognised by the naked eye. For example, from Figure 5.11 (a), which is recorded without any etching process, the shape of the particles and the boundary of the grains can not be observed distinguishingly clear as shown in Figure 5.11 (b), which is after a chemical etching process. The etching solution used was a mixture of 100ml Ethanol and 3ml Nitric acid.

5.3.3 Hardness Measurement

The hardness of the coating samples, which were produced by SUPERJET spray process, were measured by the Vickers test method using the *BUEHLER MICROMET II* micro hardness tester. The measurements were made at coating cross sections and the surfaces respectively. The indentation was observed using a microscope at a magnitude of 50X and the indentation width was measured and from this the hardness values were determined using Equation 4.1. The force P applied to cause the indentation was 300g with a load time of 13 seconds. Twelve samples were tested for analysing the hardness variations between three types of coating powders.

After the hardness measurements were made on each sample, a maximum and a minimum value were picked, and a diagram with a variation of the hardness values is plotted. Figure 5.12 shows the measured hardness at the cross sections of the coating samples.

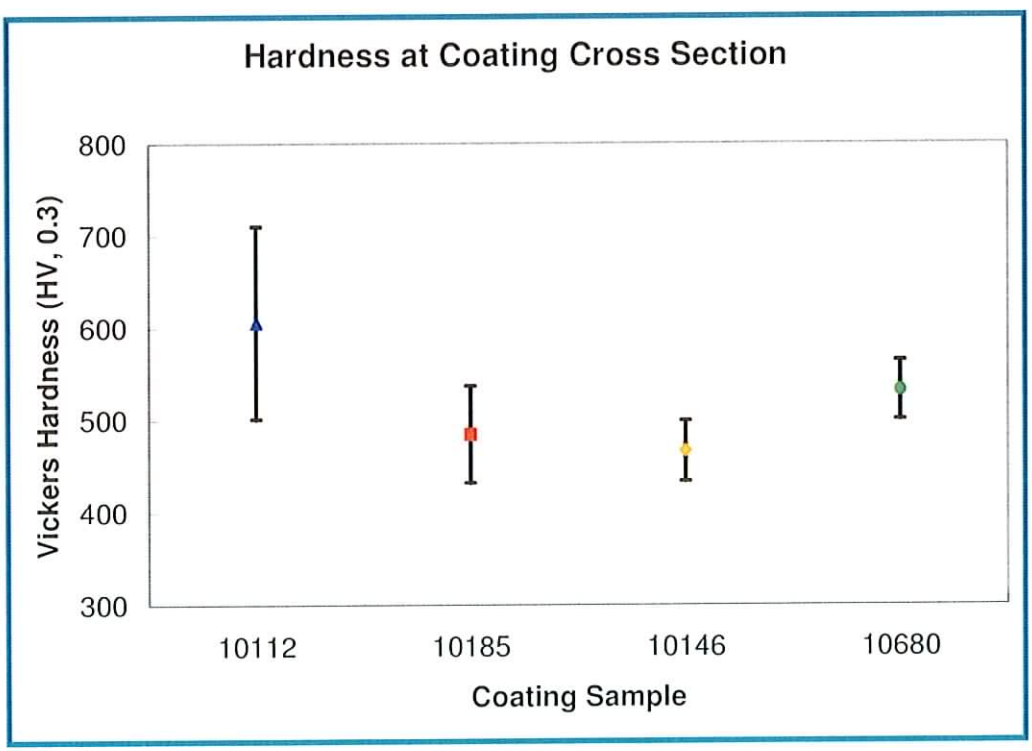

Figure 5.12. Hardness Measurement at Coating Cross Section

It can be noticed that the measured hardness values have a great variational range, i.e. sample 10112. The reason for the variations of the hardness values is the indentation

area difference. When the indentation was made on a particular area, in which hard particles were highly concentrated, such as on the Tungsten Carbide, the hardness value was higher; when the indentation was made on the area without many hard particles, the hardness value was relatively lower. This can also be observed from the optical microstructure imaging.

Figure 5.13 shows the hardness values of different coatings, which were measured at the coating surfaces. It can be noticed from the figure that coating sample 10112 has the highest hardness value, averaging 891 HV,0.3. The main contributory factor to this phenomenon is 60% Tungsten Carbide, which provided very high hardness. Therefore, coating sample 10112 would possess the best resistance to abrasion and wear compared to the others. Coating sample 10146 has the lowest hardness value of 446 HV,0.3. In some of the coatings, the material particles of the constituents are not uniformly distributed (i.e. coating 10112), this results in a greater variational range, as explained earlier in the cross section hardness measurement.

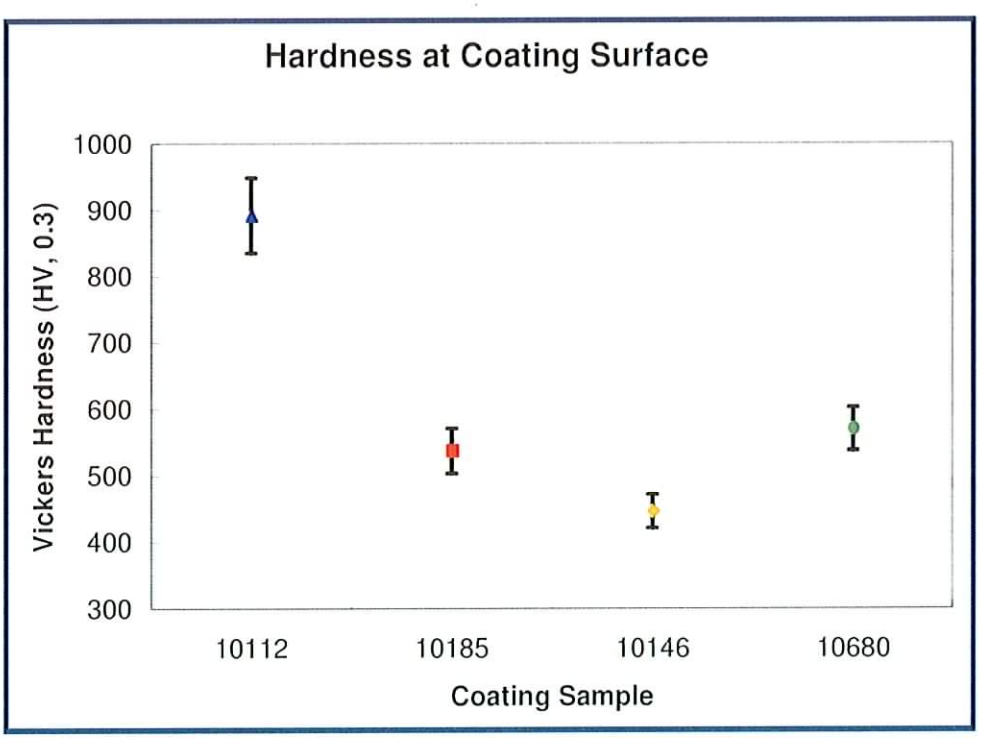

Figure 5.13. Hardness Measurement at Coating Surface

In comparison of the two measurements, at the cross sections and at the surfaces, hardness values of coating sample 10112 have considerable difference. The

measured value at the coating surface is much higher than at the cross section. This is again might be caused by the inhomogeneity of the WC particles distribution along the coating surface and the depth. The rest of the measurement comparisons (coating 10185, 10146 and 10680) all show a good similarity.

Errors may occur during the hardness measurement, such as when reading and judging the boundary of the indentation, or the indenter may sometimes give an unstable indentation.

5.3.4 Surface Roughness Measurement

Figure 5.14 shows the average surface roughness of the thermal sprayed alloy coating samples which are produced by SUPERJET process. These results are obtained from the measurements using a mechanical method. The equipment used for the measurement is *DIAVITE DH-6* surface roughness tester. It can be seen that the *Ra* value of the samples varies from 7μm to 13μm, and with an average value of 9.16μm. *Rq* has very close values for each sample, and its average is 1.306μm.

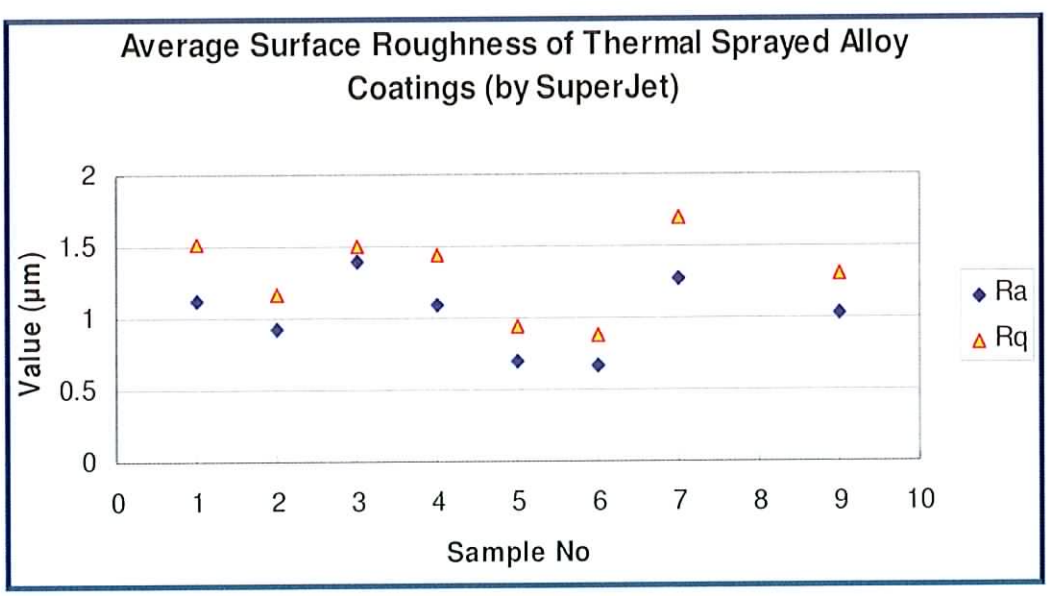

Figure 5.14. Average Surface Roughness of Coating Samples Produced by SUPERJET Process

5.3.5 Coating Elasticity Measurement

Residual stress results are presented in subsequent sections. Therefore it was necessary for the Young's modulus and Poisson's ratio for the NiCrSiB alloy deposit (10185) to be measured. This was done using the cantilever test described earlier at three loading levels (1kg, 2kg and 3kg weight).

The experiment was carried out on a cantilever beam (6.60mm x 25mm x 230mm), coated with NiCrSiB alloy powder, coupled with two rosette strain gauges attached on the top of the coating and at the bottom of the substrate. The strain gauge factor is 2.12. Table 5.1 lists the experimental data of the test.

Test No.	Load (g)	Deflection (mm)	Channel 1	Channel 2	Channel 3	Channel 4
1	1000	0.346	+41	-14	-46	+10
2	2000	0.683	+80	-26	-91	+22
3	3000	1.023	+123	-37	-135	+37

Table 5.1. Experimental Data of Cantilever Beam Test

The method is based on a least squares fit of the equilibrium equations utilising the strain gauge data. The functions described before (Equation 4.8 to 4.11) were analysed to evaluate a Young's modulus and Poisson's ratio for the coating deposit which minimised the stress difference in the equations. Minimising the function yielded a Young's modulus of 180.3GPa and Poisson's ratio of 0.28 for the NiCrSiB alloy material, as listed in Table 5.2.

	Substrate	Coating (10185) - Supplier	Coating (10185) – Experimental Results
Young's Modulus (MPa)	200	183	180.3
Poisson's Ratio	0.29	0.31	0.28
CTE (500 ~ 600 °C)	13.9	15.88	15.88

Table 5.2. Material Properties of Substrate and Coating (10185)

The data provided by the supplier shows the stiffness for the alloy powder 10185 is 183MPa, similarly the Poisson's ratio for the material is around 0.31 [12], hence this data supports the results found in the present study.

5.3.6 Residual Stress Measurement

Both of the residual stress measurements were carried out on the coating 10185 with mild steel substrate. The quenching stress has already been shown to be [95]:

$$\text{Quenching Stress, } \sigma_q \approx \alpha_c (T_m - T_s) E_c \qquad \text{Equation 5.1}$$

Where α_c, T_c, T_s, and E_c, are the respective deposit coefficient of thermal expansion, lamella temperature, substrate temperature and deposit stiffness (180.3GPa). Equation 5.2 estimates the stress generated in the coating due to the thermal expansion mismatch between coating and the substrate [119-121].

$$\sigma_{cooling} = \frac{[E_c \Delta T(\alpha_c - \alpha_s)]}{[1 + 2(E_c T_c / E_s T_s)]} \qquad \text{Equation 5.2}$$

Where ΔT is the difference in temperature between the coating and the substrate, and α_c and α_s are the thermal expansion coefficients for the deposit (17.5 W/mK) and substrate (51.9 W/mK).

Figure 5.15 (a) shows the substrate expands during the pre-heat treatment cycle, while subjected to a pre-heat temperature of 150 °C. As the change over from pre-heating to spraying occurs, the substrate temperature drops a little. During spraying the deposition temperature increases to 420 °C, therefore the substrate expands further. During the fusing process, the temperature increases to 700 °C, therefore the substrate expands more. The individual particles try to contract after they strike the substrate surface. However, the substrate resists this contraction, generating a tensile stress in the lamella, as shown in Figure 5.15 (b). Once deposition ceases, cooling stresses generate (Figure 5.15 (c). The substrate contracts to a greater extent than that of the deposit, producing a compressive stress during cooling. The final stress at the

coating surface is obtained by adding the quenching stress result to the cooling stress result [96].

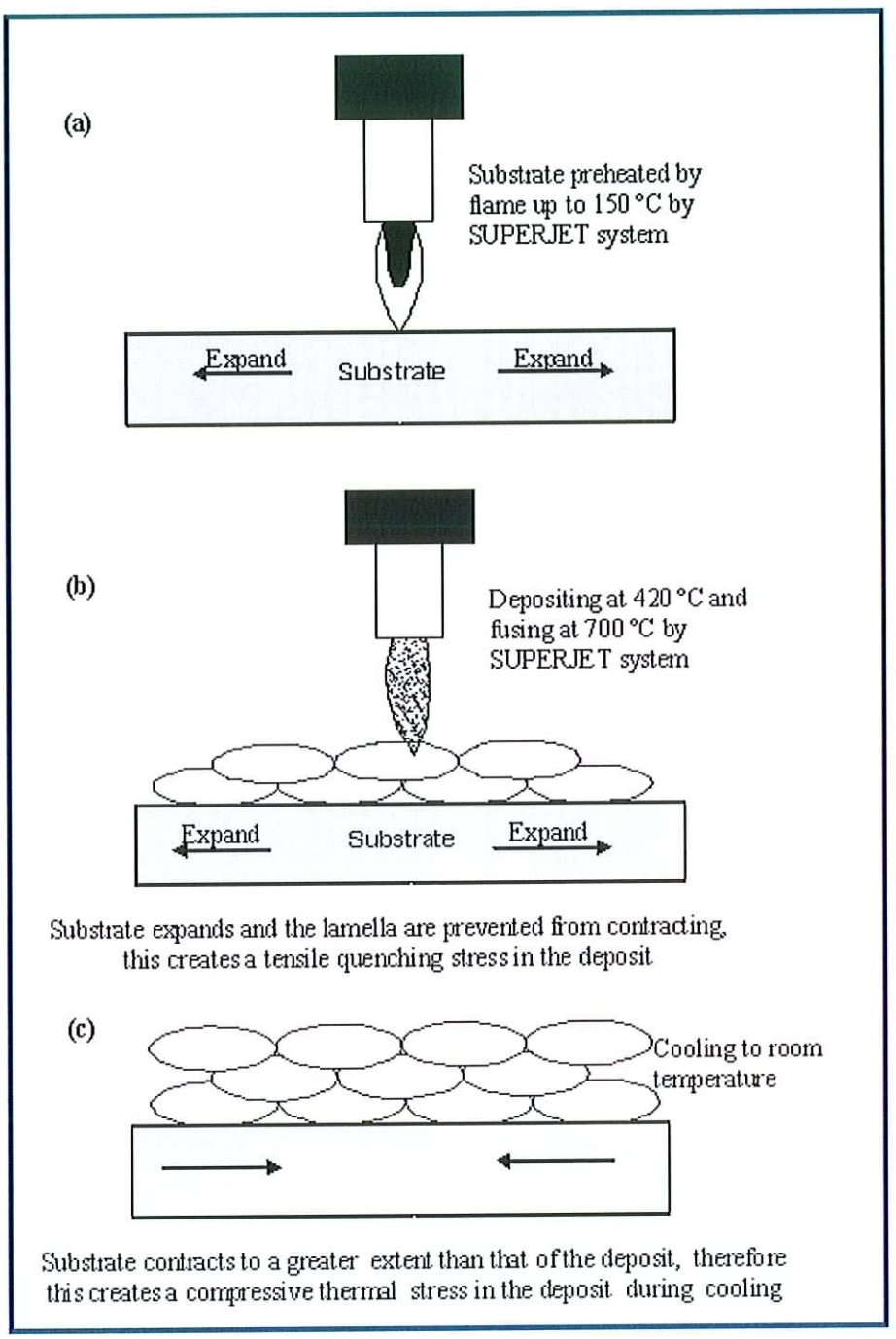

Figure 5.15. Residual Stresses Developed in the Deposit, Adapted from [24]

5.3.6.1 Residual Stress Measured by Hole Drilling Method

In the hole drilling method, the samples are relieved using a semi-destructive method, where a hole is milled through the sample. The drill used for the milling operation has a diameter of 1.57mm, and the diameter of the gauge circle is 5.13mm. The coefficient *a* and *b* can be found as 0.12 and 0.305 from Figure 4.23. The factor of the strain gauge used in the hole drilling method is 2.09.

Figure 5.16 shows the average stress measured as the carbide cutter mills a 0.5mm deep blind hole on the coating sample. Within the close vicinity of the hole, the relief is nearly complete when the depth of the drilled hole approaches 0.4D (the mean diameter of the strain gage circle) or in the case of a material whose total thickness is less than 1.2D, a hole passing through the entire thickness. The relief stress (the residual stress in deposit) in Figure 5.16 is taken to be 78MPa for example.

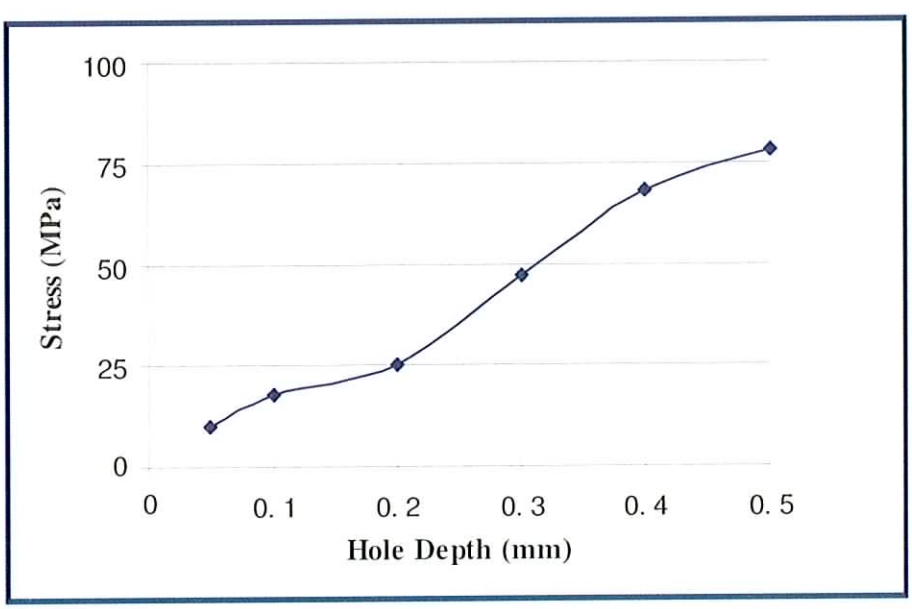

Figure 5.16. Stress Relieved with the Hole Drilling Method

5.3.6.2 Residual Stress Measurement by Cylne's Method

According to the data shown in table 5.2, the Young's modulus value used in the residual stress equations for the coating was 180.3GPa, which was found in the cantilever test. The Young's modulus value for the substrate was used in the

equations was 200Gpa, which was obtained from the data supplied by the material supplier. A Figure 5.17 shows the coated sample and its deflection.

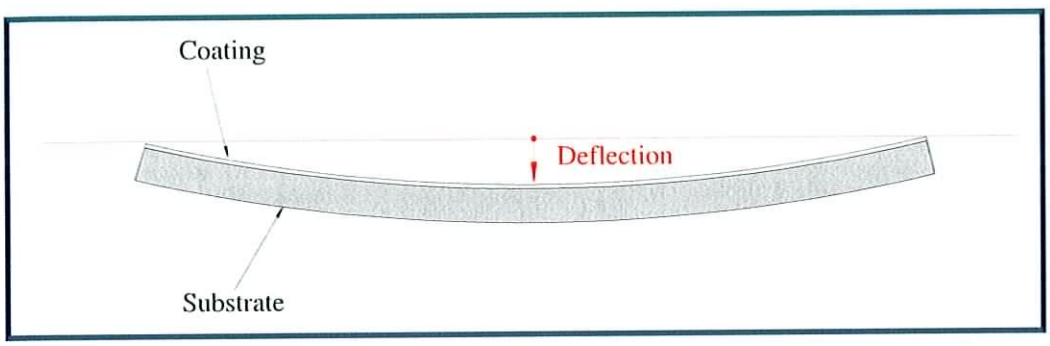

Figure 5.17. An Example of Deflected Sample

Figure 5.18 shows the residual stress distribution using Clyne's Analytical Method accounting for misfit strain, through a 0.5mm thick coating 10185 (NiCrSiB deposit). The figure shows the four calculated points (Equation 4.16 to 4.19), and these have been connected by straight lines, indicative of the stress distribution through the sample. The deposit has a compressive stress of 75.46MPa on its top surface (Table 5.3) and a tensile stress of 70.68MPa at the coating – substrate interface. The interface has a stress decrease of approximately 140MPa, whereas the coating experiences a stress change through the coating approximately of 145MPa.

Distribution of the Stress	**Stress Value (MPa)**
Stress at the top of the coating	-75.46
Stress at the interface of the coating	+70.68
Stress at the interface of the substrate	-68.15
Change across the deposit	+146.14
Positive (+): Tensile Stress, Negative (-): Compressive Stress	

Table 5.3. Residual Stresses Measurement of Sample 10185 Using Cylne's Method

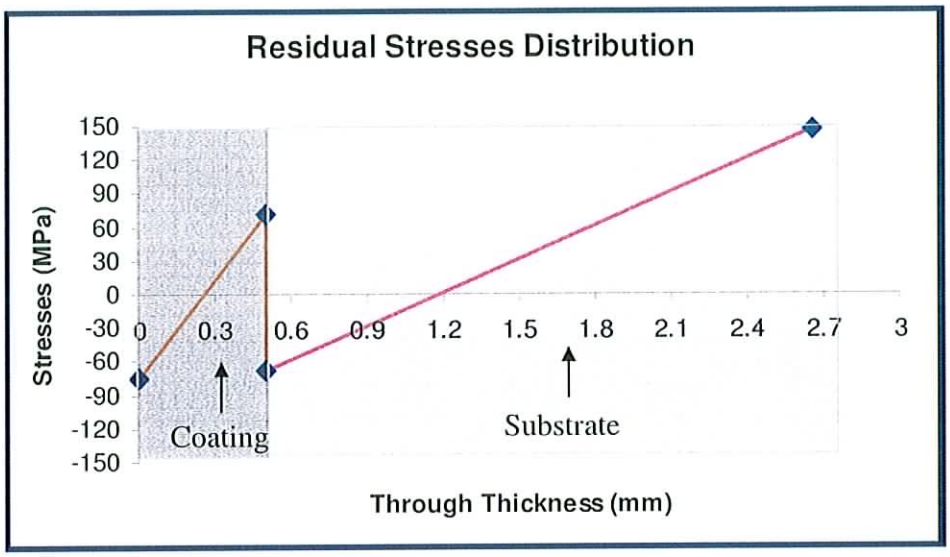

Figure 5.18. Distributed Residual Stress through 10185 Coating Calculated Using Cylne's Analytical Method

Clyne's Analytical Method accounts for misfit strain at the interface, and is used to identify the stress distribution through various samples. Experimentally measured deflections and material properties were placed into the analytical equations (Equations 4.16 to 4.19), to establish the distribution.

The thermal expansivity of the substrate and the deposit are very important for the quality of the coating product, particularly for those coatings which are deposited at high temperature, such as the coatings produced by SUPERJET spray process. Thermal contraction stress will build up when the deviation of the thermal expansion coefficient is large. These thermal contraction stresses may promote debonding during cooling, and will introduce errors in measurement of the deposition stress.

5.3.6.3 Comparison of the Two Measurements

Figure 5.19 shows the comparison between the residual stresses measured using the Clyne's method and the result found using the hole drilling method. Only the residual stresses in the interface of the coating and the substrate were compared, as this is where the maximum residual stress of the coating locates. The results show that Clyne's Analytical Method produced stress values approximately 91% of that found using the Hole Drilling method. It can be seen that the residual stress results obtained from these two methods show a very good agreement.

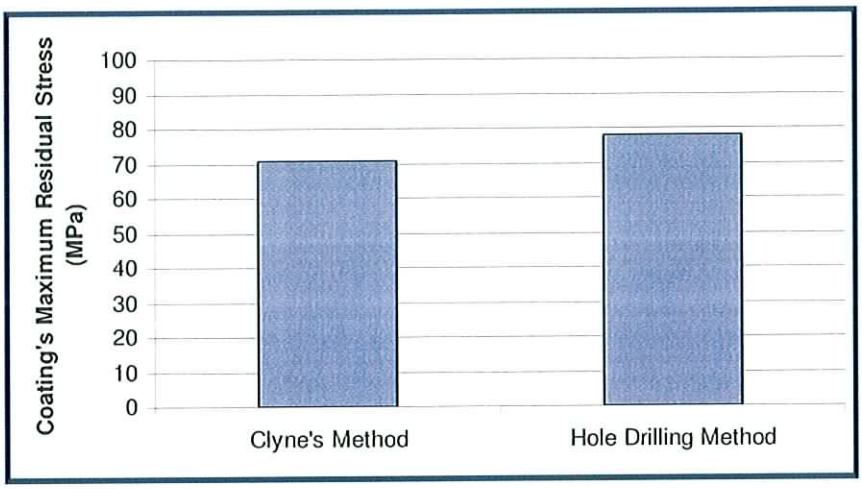

Figure 5.19. Comparison of Residual Stresses between Clyne's Method and the Hole Drilling Method

5.4 OPTICAL CHARACTERISATION OF THERMAL SPRAYED COATINGS

5.4.1 Coating Surface Roughness Measurement using WLI

The coatings surface was profiled using a WLI surface profiler *MicroXAM S/N 8038*, as shown in Figure. The White Light Interferometric profiler provides quantitative 2D and 3D visual data of the coatings. X-Y profiles of the coated surfaces provide valuable information about the profiles and dimensions of the defects detected. Figure 5.20 shows the 3D height profile and Figure 5.21 shows the X-Y profile of the coating sample 10009. Figure 5.22 shows the 3D height profile and Figure 5.21 shows the X-Y profile of the coating sample 10185. The *Ra* values of samples 10009 and 10185 can be found as 1.37μm and 0.67μm respectively.

The technique is non-contact and covers the whole surface, unlike conventional stylus profilometry. It also offers very high precision limited only by the minimum translation step of the mirror. Computer algorithms have been developed to cope with smooth and rough surfaces.

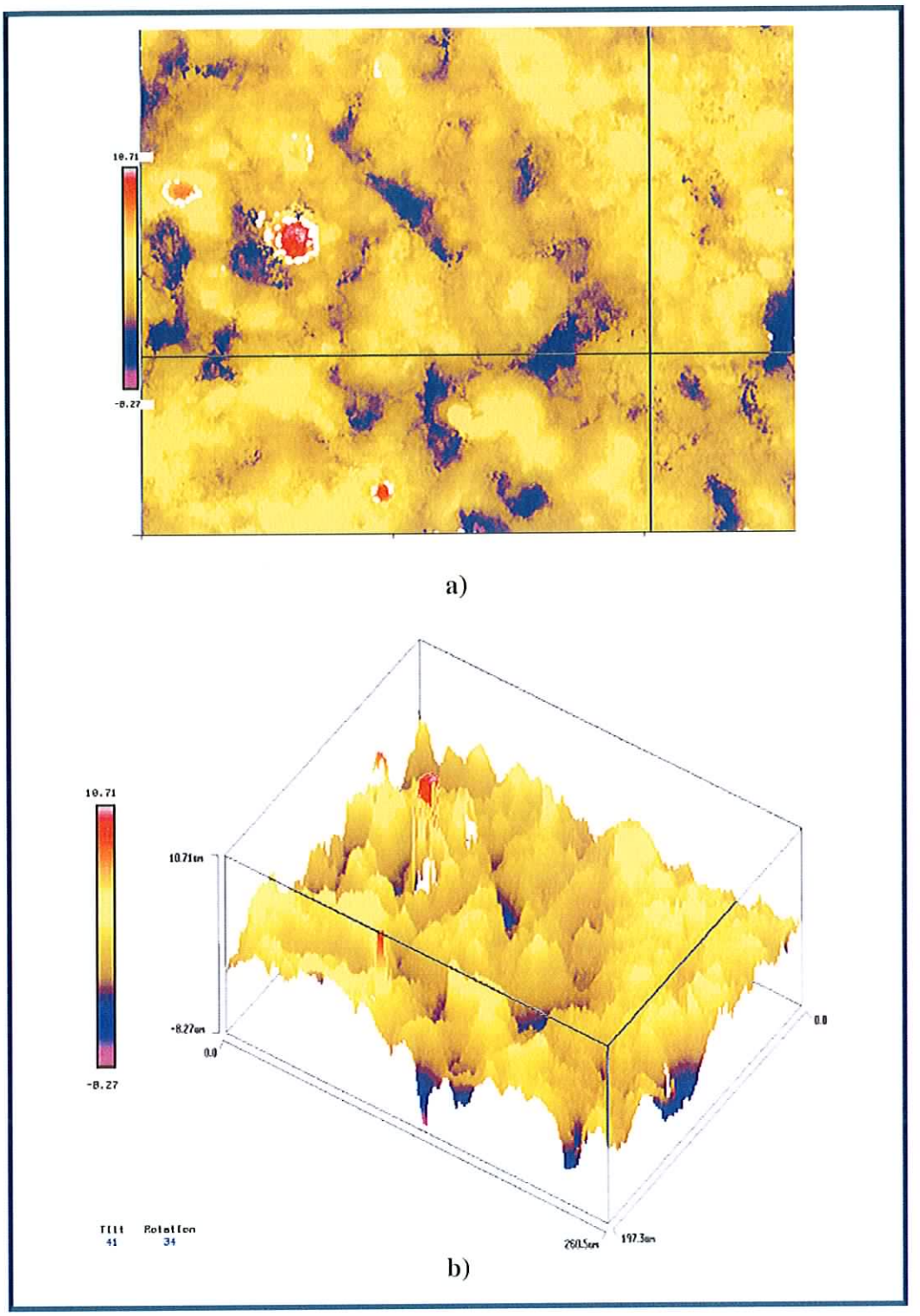

Figure 5.20. White Light Interferometer Measurement of Sample 10009, a) 162.82x123.29 μm Image of Coating Sample; b) the 3D Height Profile, Magnification of 50.4

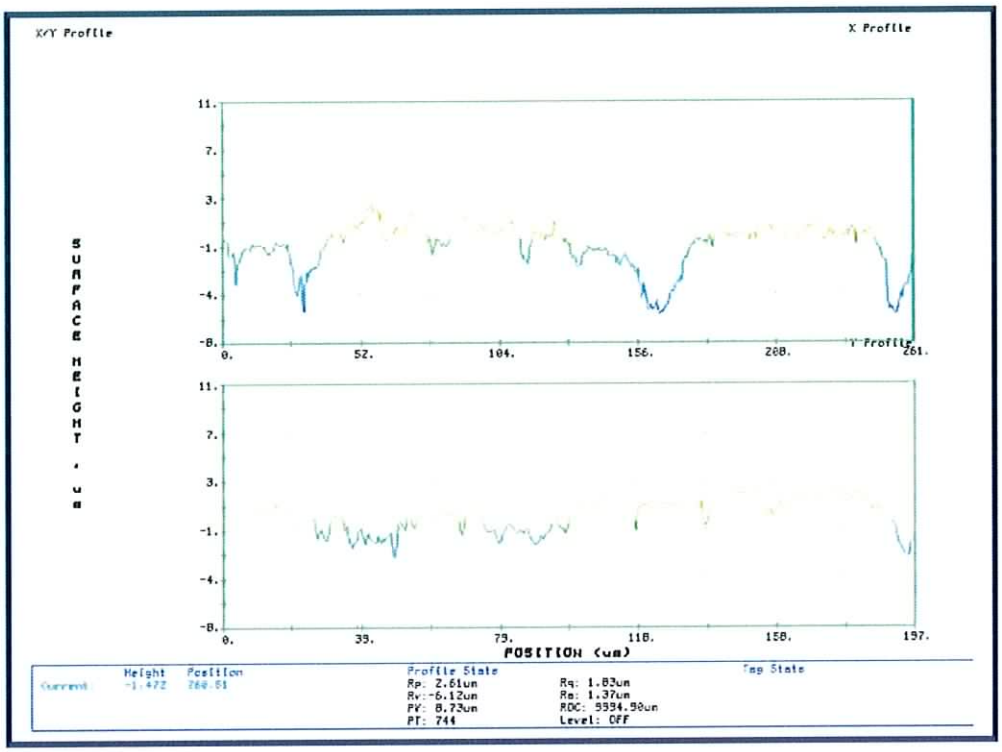

Figure 5.21. The X-Y Profile of Sample 10009 in WLI Measurement, Magnification of 50.4

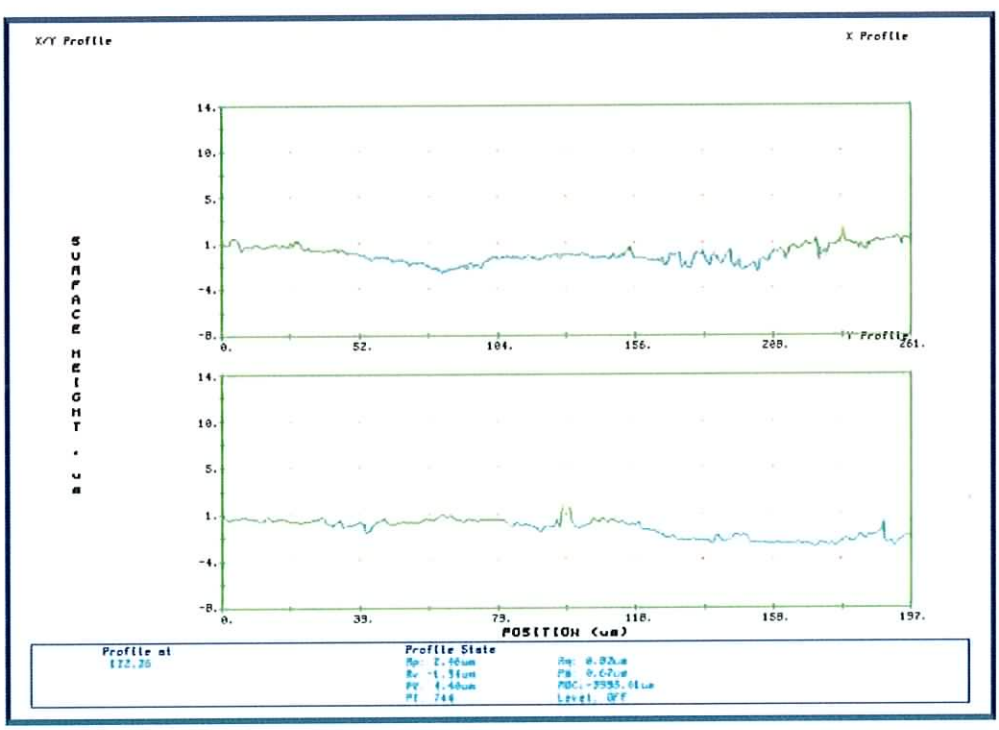

Figure 5.22. The X-Y Profile of Sample 10185 in WLI Measurement, Magnification of 50.4

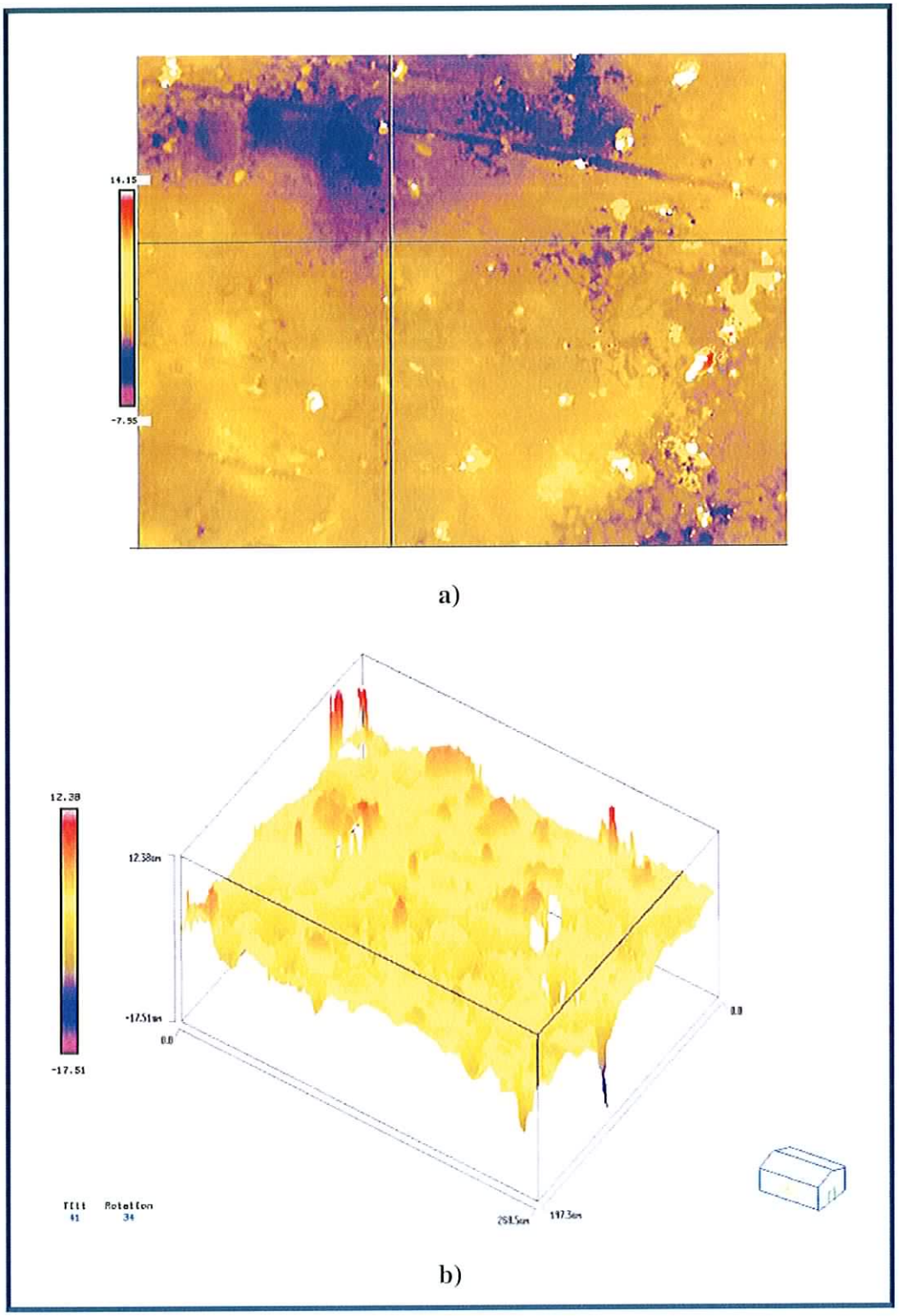

Figure 5.23. White Light Interferometer Measurement of Sample 10185, a) 162.82x123.29 µm Image of Coating Sample; b) the 3D Height Profile, Magnification of 50.4

5.4.2 Comparison of Mechanical and Optical Measurements

A comparison between mechanical and optical measurement has been made, as shown in Figure 5.24. The comparison shows a good agreement between the two types of techniques. However, it can be seen that the mechanical measurements show greater values than the optical measurement. Some of the mechanical measurements obtained from the Taylor-Hobson method are very inaccurate and they are not reliable.

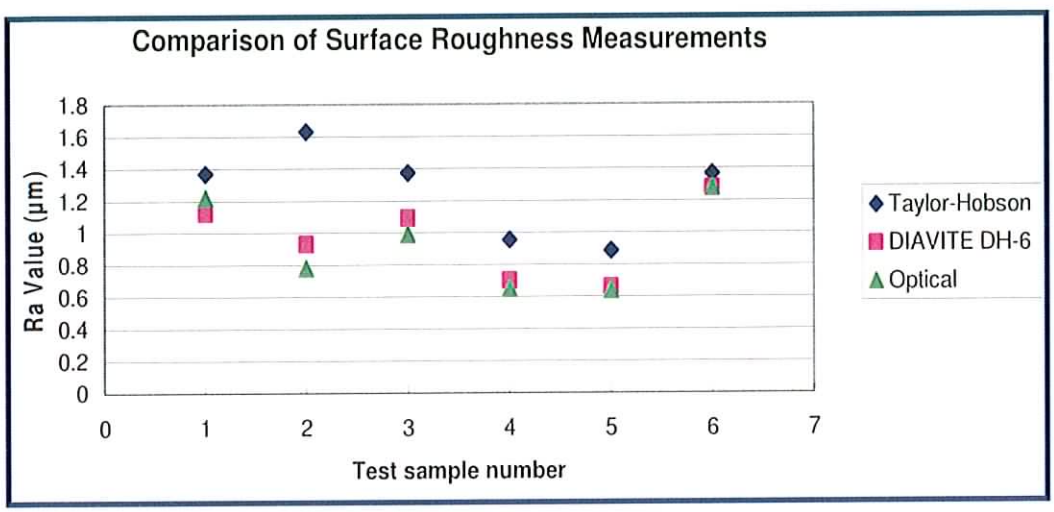

Figure 5.24. Comparison of Roughness Measurements of Several Coating Samples

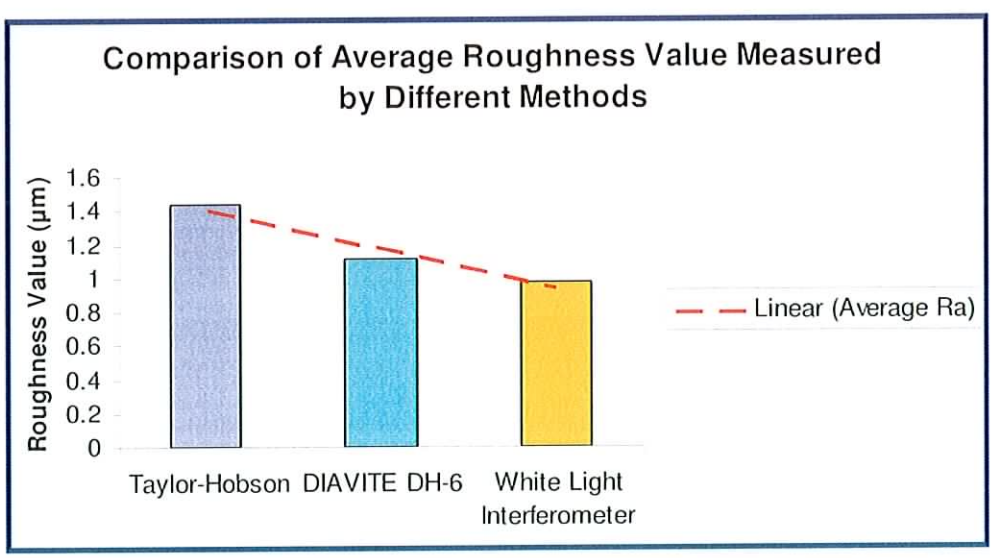

Figure 5.25. Comparison of Average Roughness Values between Different Methods

The average roughness of the coating samples measured from mechanical method is given as 1.02 microns, and the average roughness value of these samples from optical measurement is given as 0.96 microns. Thus compared to the British Standard [122], the average roughness of coating samples which are produced by SUPERJET spray process is illustrated in Figure 5.26.

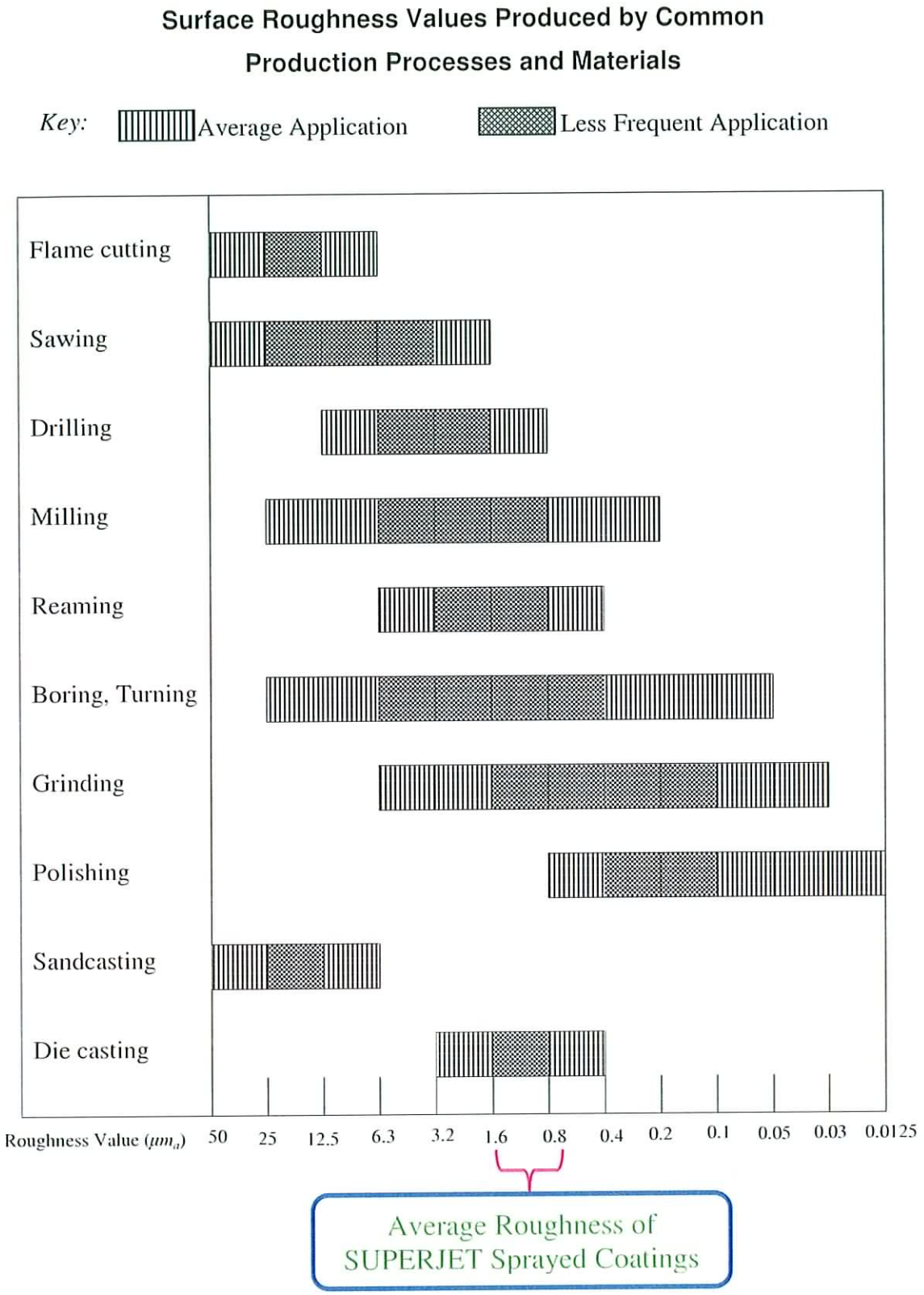

Figure 5.26. Surface Roughness of Various Common Processes and Materials, Adapted from [122]

5.4.3 Defect Detection of ESPSI

The detection of delamination, inadhesion, and microcracks depends to a great extent on the type of stress, the shape of the test structure, and the shearing direction of the measurement device.

In general, for a certain stressing magnitude, the anomalous ranges of the fringe pattern depend on the size of the defects and the fringe density, and these are determined by both the size of the disbonds and their penetration of the object's surface [76].

Using the thermal stressing method, a steady-state thermal deformation cannot usually be easily maintained. Therefore, it is difficult to generate a phase map when the change in the temperature gradient is great. A wait of a few minutes after introducing the thermal stressing is recommended.

The temperature difference causes local strain differences (or differences in the deformation gradient) because of the different properties of the alloy coating and the mild steel substrate, such as the density and the linear coefficient of the thermal expansion. A different strain distribution occurs, which can be detected by shearography. A large shearing amount increases the number of fringes until the fringe density can no longer be resolved, and with that, the sensitivity of the measuring method becomes greater and vice versa [76].

To make a sample that is more suitable for a three point bending test rig, one solution is to use thinner substrates, although there is a limit to this, since very thin substrates become difficult to handle and prone to fracture or undergo plastic deformation.

The relative deformation means the deformation difference between two points with separation of a shearing amount. The relative deformation depends greatly on the shearing amount. A measurement with a big shearing amount is sensitive to the relative deformation not only at the defect position but also at the area of base material. This will make the localisation of defect and determination of defect size difficult [75].

The measuring sensitivity for NDT will reflect how small a defect can be detected. In shearographic systems, shearing amount will be the factor determining the measuring sensitivity of the system. In most of the industrial applications, the minimal diameter of defect which is being detected is usually known. Therefore, the shearing amount can be accordingly selected approximately with the half diameter of the minimal defect [75].

Figure 5.27 shows the area under investigation on the sample 10112.

Figure 5.27. The Area of the Sample 10112 under Investigation. The Field of View is 30mm x 20mm.

Figure 5.28 to 5.30 show the shearographic fringe patterns depicting the derivatives of the deflections on sample 10112 with shear of 4mm, 8mm and 12mm respectively. These fringe patterns are obtained in real time. It is proved that the shearing amount affects the fringe order numbers. The bigger shearing amount, the more fringes observed from the experiment. In each figure (Figure 5.28, 5.29 and 5.30), (a), (b), (c) and (d) represent deflections of 40nm, 80nm, 120nm and 160nm produced by the three-point bending test rig, respectively. It is observed that these fringe patterns have a very good repeatability and consistency, which proves that this three-point bending test rig produces the required displacements and is suitable for ESPSI quantitative measurement.

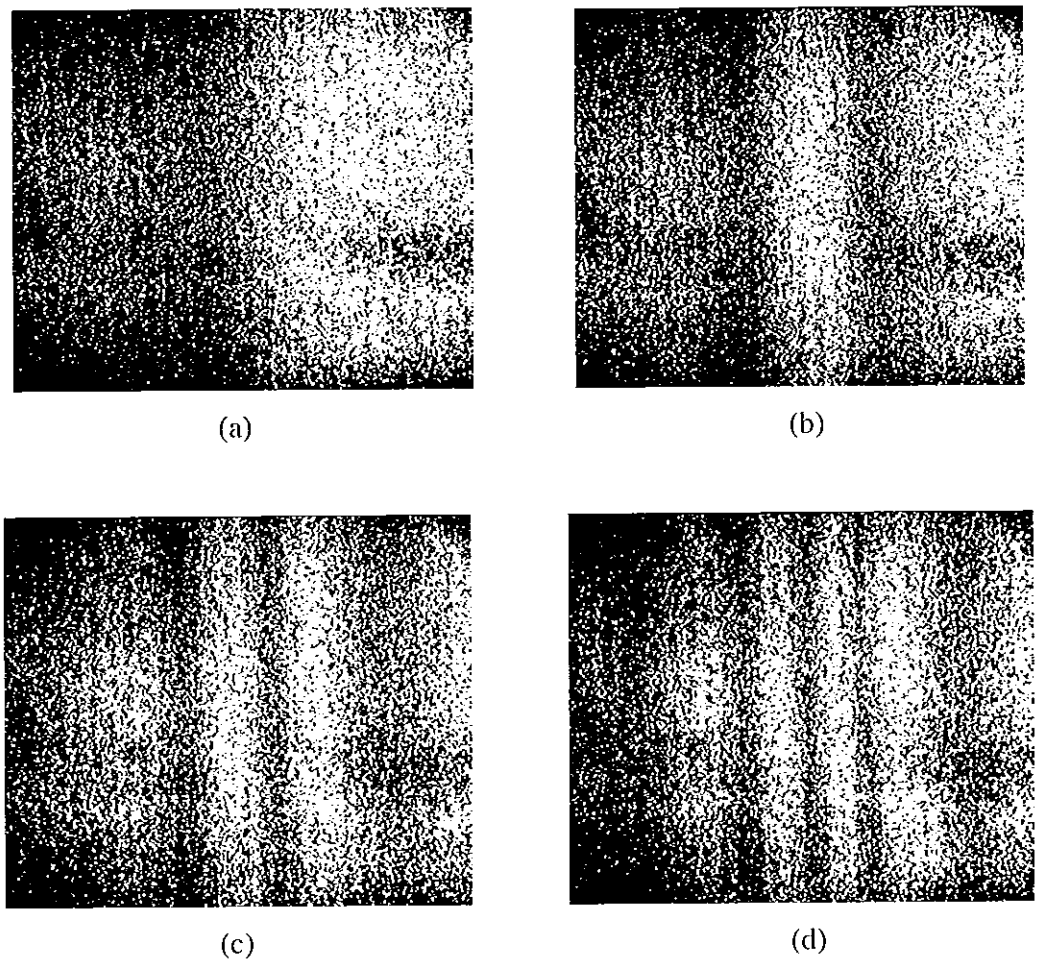

(a) (b)

(c) (d)

Figure 5.28. ESPSI Fringe Patterns of Coated Sample 10112 during Three-Point Bending under Deflection of: (a) 40nm; (b) 80nm; (c) 120nm; (d) 160nm. The Shear is Δx =4mm. The Field of View is 30mm x 20mm.

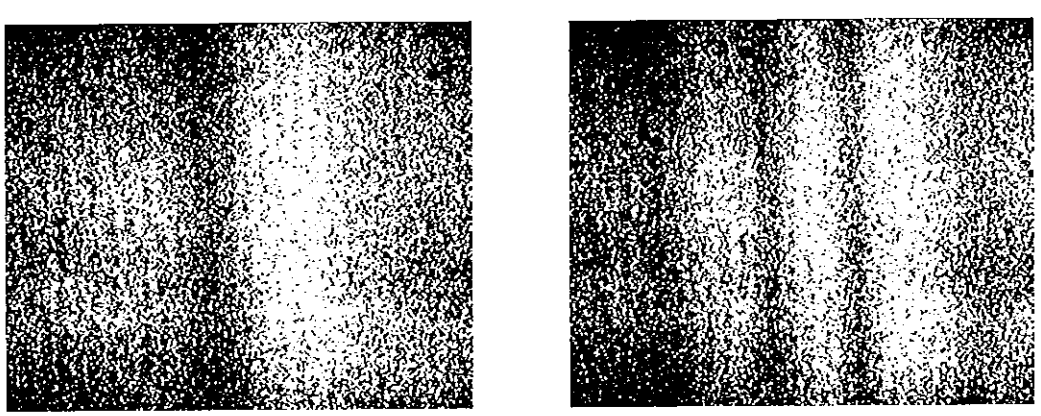

(a) (b)

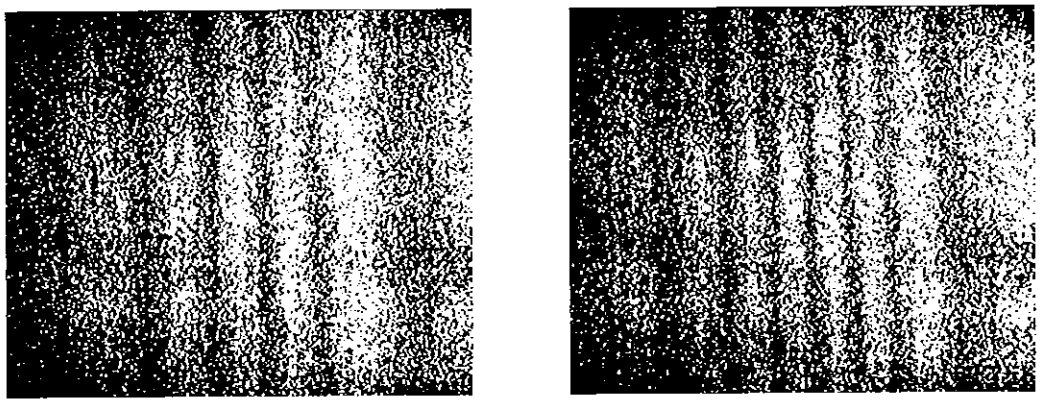

(c) (d)

Figure 5.29. ESPSI Fringe Patterns of Coated Sample 10112 during Three-Point Bending under Deflection of: (a) 40nm; (b) 80nm; (c) 120nm; (d) 160nm. The Shear is Δx =8mm. The Field of View is 30mm x 20mm.

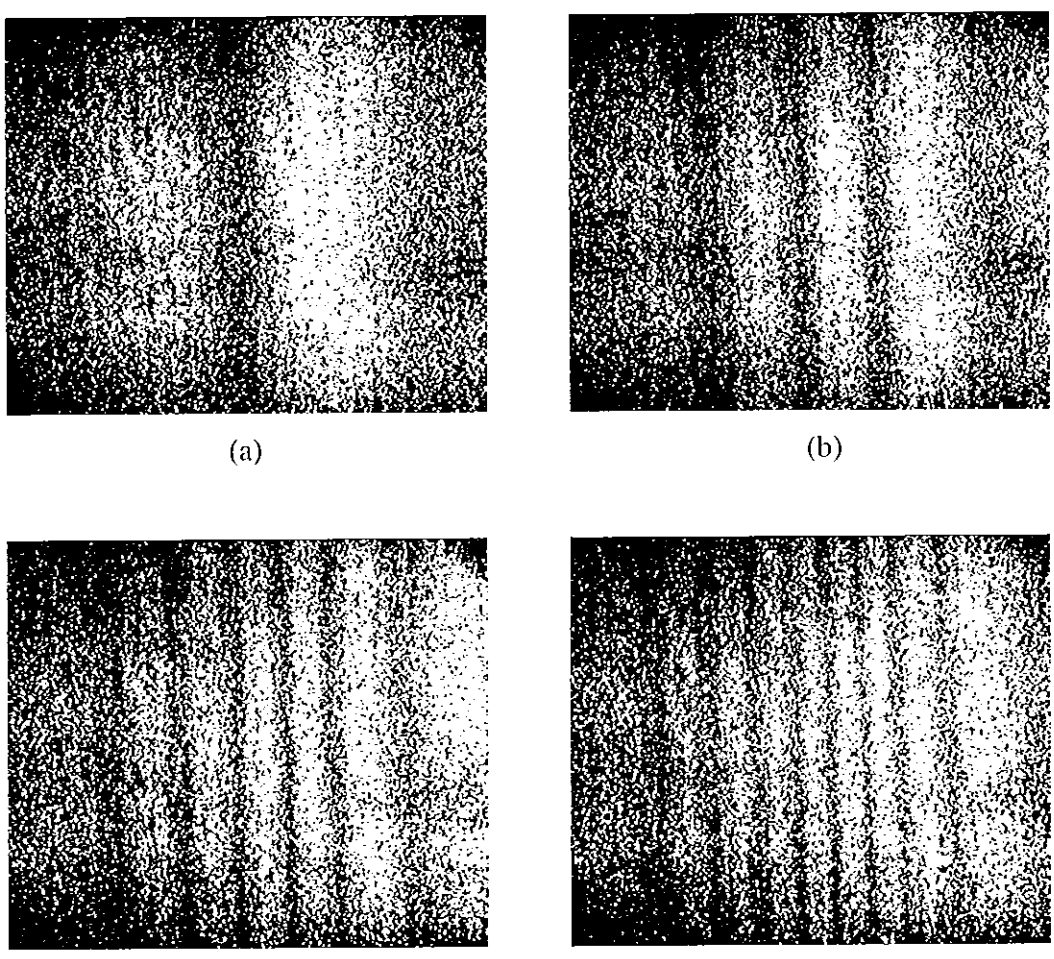

(a) (b)

(c) (d)

Figure 5.30. ESPSI Fringe Patterns of Coated Sample 10112 during Three-Point Bending under Deflection of: (a) 40nm; (b) 80nm; (c) 120nm; (d) 160nm. The Shear is Δx = 12mm. The Field of View is 30mm x 20mm.

Figure 5.31 presents some examples of the ESPSI results for non-defective sample 10112 under cooling. The sample was stressed by heating it with a tungsten-halogen lamp. During experiments we observed irregular dark fringes moving rapidly all over the area under investigation. They disappear quickly, and there is no repeatability and consistency. They are clearly due only to the random variations in the rate at which the surface cools and contracts.

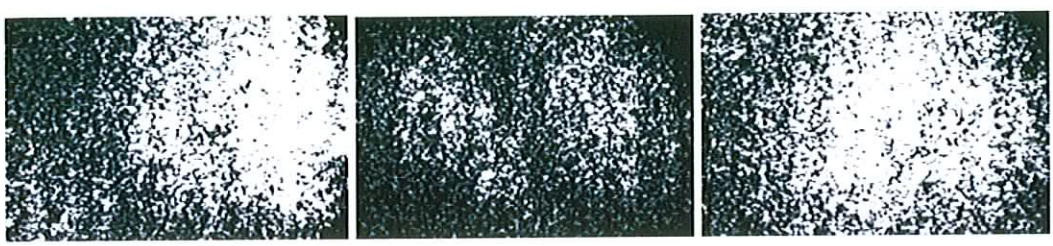

(a) (b) (c)

Figure 5.31. ESPSI Fringe Patterns of Coated Sample 10112 under Thermal Stressing by using a Tungsten-Halogen Lamp during Cooling: (a) 2nd Second; (b) 4th Second; (c) 6th Second. The Shear is Δx =8 mm. The Field of View is 30mm x 20mm.

On sample 10185, a large delamination on the coating was found, as shown in Figure 5.32. In this area, a part of the coating was lifted off due to the poor coating adhesion.

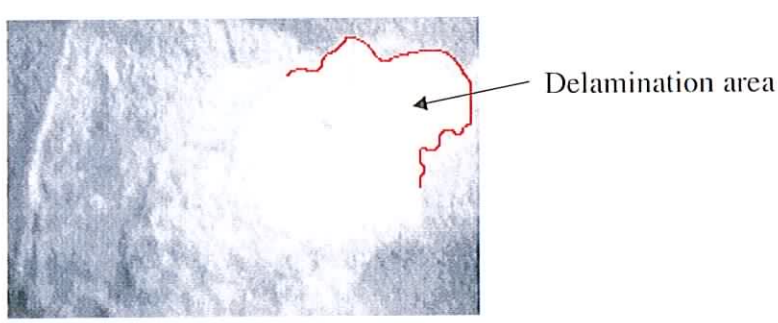

Figure 5.32. Area of the Delamination of Coating Sample 10185
The field of view is 30mm x 20mm

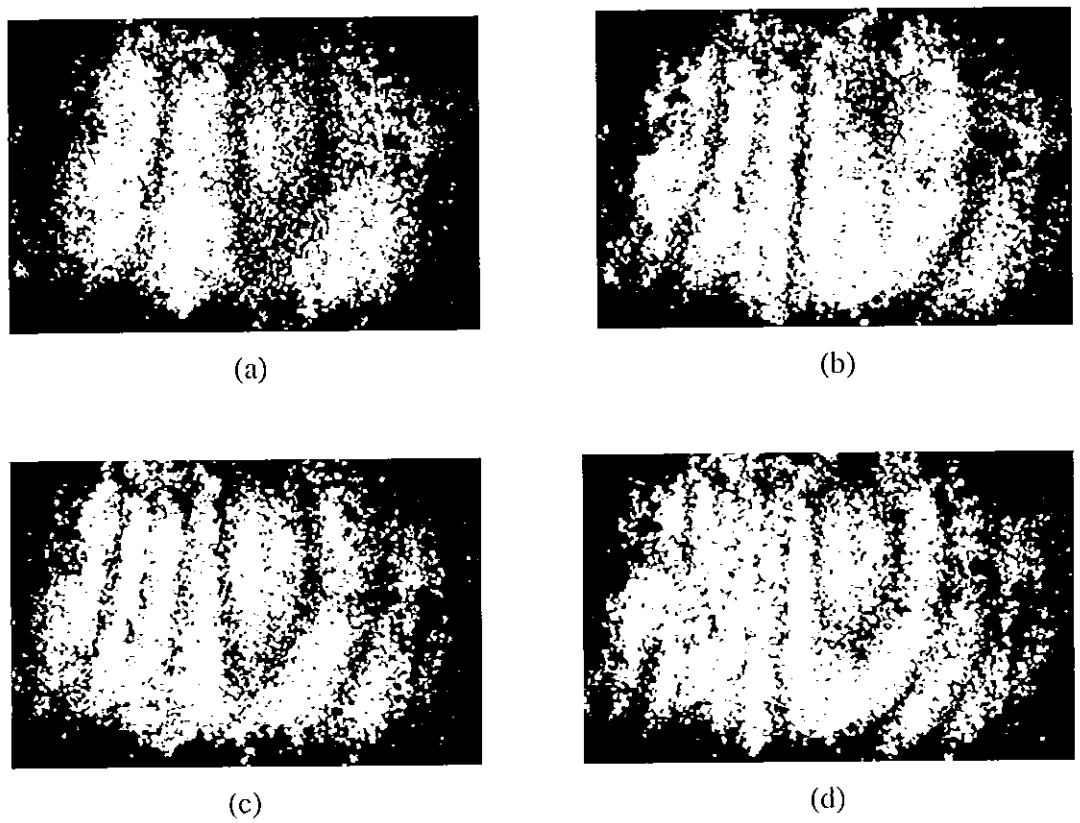

Figure 5.33. ESPSI Fringes of Coated Sample 10185 under Thermal Stressing by using a Tungsten-Halogen Lamp during Cooling: (a) 1st Second; (b) 2nd Second; (c) 3rd Second; (d) 4th Second. The Shear is $\Delta x = 10mm$. The Field of View is 30mm x 20mm.

Figure 5.33 showed the ESPSI results for the sample 10185 which were obtained at the 1st, 2nd, 3rd and 4th second of the recording. In this case, the sample was thermally loaded by using a tungsten-halogen lamp illuminating near the sample surface for approximately 30 seconds. This time, in addition to the rapidly moving fringes observed above, fringes were consistently observed in the area of the delamination. This is probably due to the very different cooling rate there, and indicates the presence of large disbond at the suspect area in the sample 10185. The number of fringes is a function of image shear, applied pressure and the diameter and the thickness of the defect. A large number of fringes for the same image shear and the same pressure implies a thinner region [13].

Figure 5.34 shows the ESPSI results for the sample 10185, which were obtained under mechanical stressing. ESPSI fringes were repeatably produced and consistently observed in the area of the delamination.

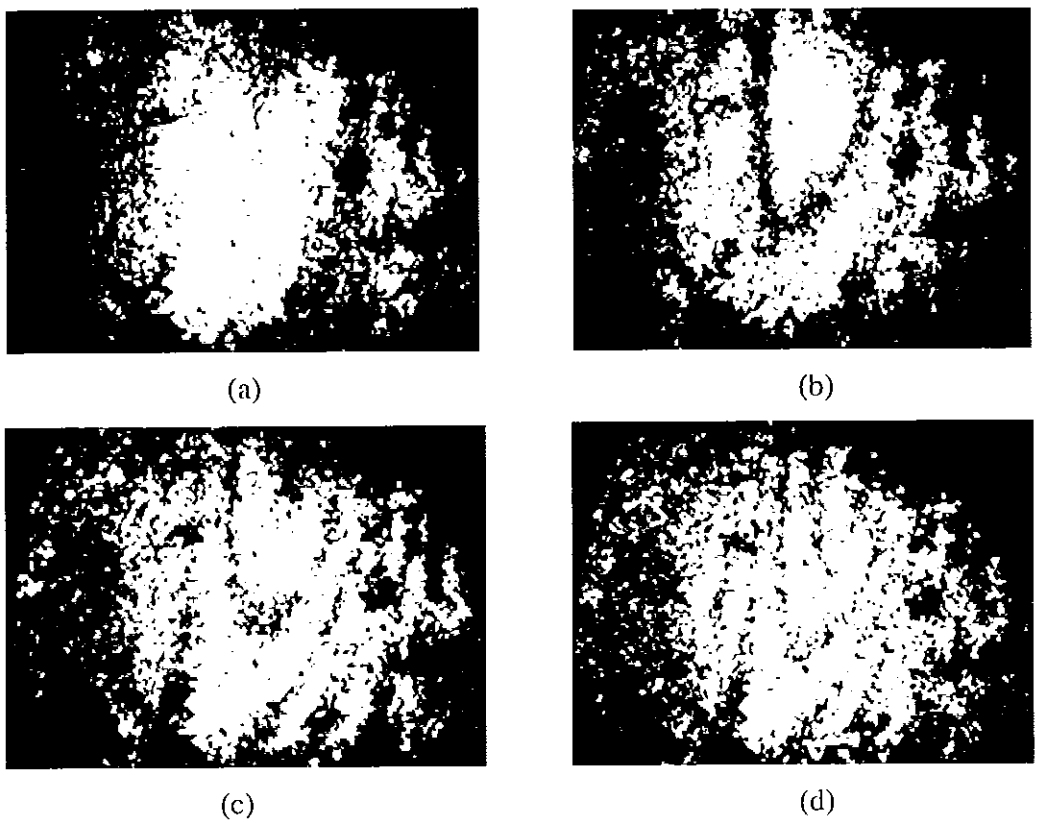

Figure 5.34. ESPSI Fringes of Coated Sample 10185 under Mechanical Stressing by using a Three-Point Bending Test Rig under Deflection of: (a) 20nm; (b) 40nm; (c) 60nm. The Shear is Δx =10mm. The Field of View is 30mm x 20mm.

The fringes are affected by both optical and electronic noise, which result in the degradation of the quality of the interferograms. The optical noise is intrinsically caused by the presence of speckles. The electronic noise is related to the video camera output and to the digitisation process. Fringe contrast reduction is often caused by speckle decorrelation effects [72].

To further the study of defect detection using ESPSI, experiments have been done on other type of coating samples. Figure 5.35 shows the ESPSI results of a thin copper plate coated with paint. On the coated surface, a "cross" scratch was made deliberately. Fringe anomalies can be found from the obtained results. These fringes were obtained under mechanical stressing method by using a three-point bending test rig under deflection of 20nm, 40nm, 60nm, 80nm and 100nm. The shear used is 8mm. The field of view is 30mm x 20mm.

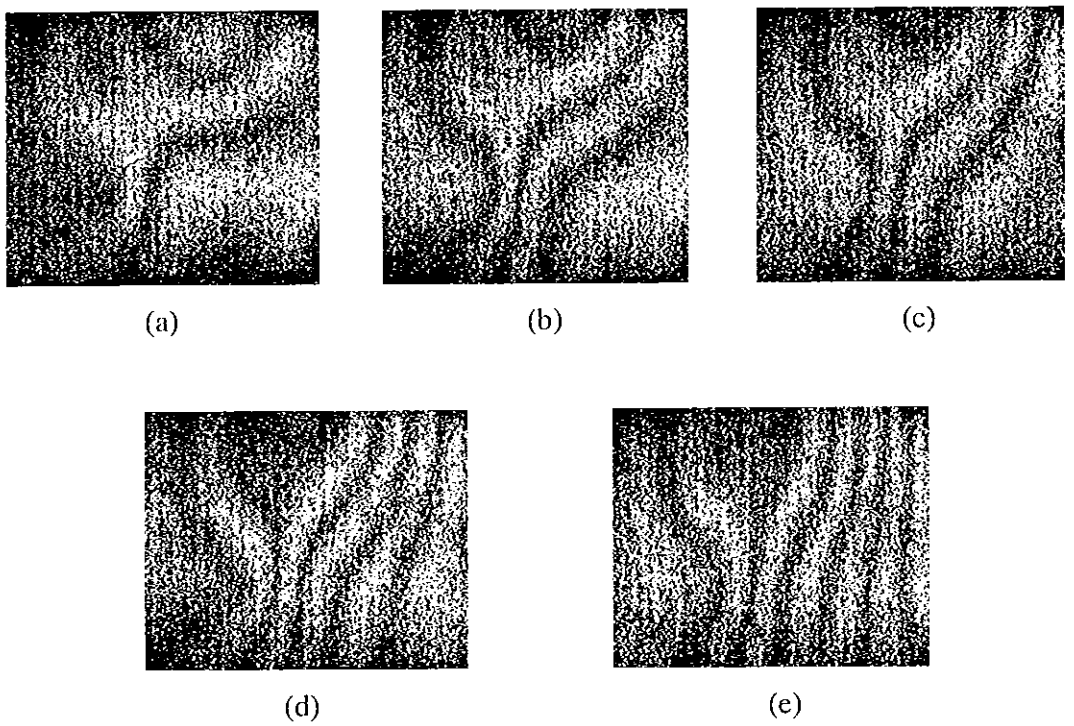

Figure 5.35. ESPSI Fringes of a Thin Copper Plate with Scratches under Mechanical Stressing by using a Three-Point Bending Test Rig under Deflection of: (a) 20nm; (b) 40nm; (c) 60nm; (d) 80nm; (e) 100nm. The Shear is Δx *=8mm. The Field of View is 30mm x 20mm.*

5.5 TEST PROCEDURES

The experimental tests conducted are repeatable by the use of White Light Interferometry and Electronic Speckle Pattern Shearing Interferometry techniques in the laboratory. Deposition of surface coating samples and testing processes of the coatings by these techniques also are repeatable, and that is what makes the process a very successful industrial tool for detecting defects in samples.

Chapter 6 – Conclusions and Recommendations

6.1 CONCLUSIONS

The aims and objectives of this work were:

i. Research of various surface coating techniques and testing methods (mechanical and optical);
ii. Sample preparation and coating deposition by using various coating materials apply on various substrate materials;
iii. Mechanical measurement and testing of coatings (hardness, surface roughness, Young's Modulus and residual stress);
iv. Optical evaluation of surface coatings (microstructure and surface roughness), coating defect detection and analysis using optical methods;
v. Compare the results obtained from the two measurements;
vi. To report on the benefits of optical processes for surface coating evaluation.

In the research, a comprehensive literature review of coating techniques and testing methods was carried out. Over 100 samples were prepared and deposited through thermal spraying by using the SUPERJET gun. Flame powder spraying process was investigated. The nature and the characteristics of coating defects were analysed and summarised. Some of the mechanical properties of coating's were measured and characterised. At least three samples were used in each type test, and the final results were drawn based on the average of the values. The conclusions resulting from the investigation are summarised as follows:

i. Some basic parameters of the SUPERJET spray process, such as spray distance and coating temperature, were calibrated and optimised.
ii. Coating thickness was measured by using dial-gauge, optical microscope and SEM methods. Dial-gauge method have results of 18% ~ 44% greater than optical measurements results (optical microscope and SEM). It can be concluded that the dial gauge method is not sufficiently accurate for measuring the coating thickness, especially in the range under 1mm. Using optical microscope and SEM give very similar result values.

iii. Elastic properties of NiCrSiB coating samples were measured using a Cantilever Beam test. Young's modulus and Poisson's ratio were found to be 180.3GPa and 0.28 respectively.

iv. Vicker's hardness of the coatings was measured on the coating surface and the cross section area. The hardness showed that coating sample 10112 had the highest value because the 60% of WC in the composition. Therefore coating 10112 possesses the best resistance to abrasion and wear compared to the others.

v. Microstructure analysis of the coating samples were carried out. Images were obtained from both optical microscopic studies and scanning electron microscopic studies.

vi. Surface roughness was measured by both mechanical method and optical method. The average roughness of the SUPERJET-produced coatings measured using mechanical method was found as 1.02 microns. The average roughness value of these samples from optical measurement was found as 0.96 microns. These results showed that optical measurements have a good agreement with mechanical measurements, and it is very suitable for surface roughness measurement of thermal sprayed coatings. Optical method also shows great advantages over mechanical method since the measurement is very fast to be carried out and the results are very accurate and give more information of the surface topography.

vii. Residual stress results were found using the Clyne's Analytical Method and were compared with Hole Drilling method. Results showed that Clyne's Analytical Method produced stress values approximately 91% of that found using the Hole Drilling. This shows a very good agreement between the two methods.

viii. ESPSI technique was used for defect detection of coating samples in the research. The obtained results showed that ESPSI was suitable for detection of delaminations and disbonds in thermal sprayed alloy coatings. The type and the magnitude of the loading affect the success of defect detection significantly. Thermal stressing and mechanical stressing were both suitable as loading methods for detection of delaminations in metal coatings. ESPSI would seem to have great potential for NDT and quality inspection of thermal sprayed alloy coatings, based on its advantages: simple optical set-up, easy to

detect defects which create strain concentrations, fast full-field technique, insensitive to small rigid body motions and thus suited for industrial applications. However, shearography also has limitations such as it is still sensitive to ambient noises, big rigid-body motion and thermal air currents, and it is difficult to measure a flaw located deep far from the object surface.

6.2 RECOMMENDATIONS FOR FUTURE WORK

i. During the temperature measurement, difficulties have been encountered when measuring the temperature during the spraying process, since the sprayed powders would have covered the thermocouple if the thermocouple was exposed and attached on the surface being coated. Recommendations can be made for overcoming this difficulty. The thermocouples can be covered under a shield or isolated from the spray zone by using a steel plate. Alternatively, the temperature can be measured at the back of the sample when applying coating at the front, then using a relationship (heat transfer) between the back and the front to work out the temperature at the front. Another method for spraying temperature measurement is using Pyrometer, which has none of these disadvantages [24].

ii. The defect detection of the coatings was carried out using two types of ESPSI arrangements. The main difference between them was the shearing device used in the system. One of the arrangements was a Michelson type system which utilised a beamsplitter as the shearing device, whereas two glass plates were used as the shearing device in the other arrangement. The results obtained from both of the arrangements showed that they were effective for the defect detections. However, the results were not compared between these two arrangements. Future work on the comparison of these two systems could be carried out.

iii. Future work could extend to other coating techniques and other substrate and coating materials (such as polymer coating and polymer substrate).

References

[1] Aldrich, D., "Surface Engineering and Golf". *Surface Engineering*, Vol. 20, No. 1, 2004.

[2] Diamond-Like Coatings, *www.arrowprecision.co.uk*, Arrow Precision Engineering, Accessed 18 October, 2005.

[3] Frainger, S., Blunt, J., *Engineering Coatings – Design and Application*, 2nd edition, Abington Publishing, Abington, England, 1998.

[4] Matthews, A., Artley, R., Holiday, P., "2005 Revisited: The UK Surface Engineering Industry to 2010", Farnborough, NASURF, 1998.

[5] Greving, D. J., and Shadley, J. R., "Experimental Evaluations of Thermal Spray Coatings for Oilfield Equipment Applications", *Proceedings of 13th International Thermal Spray Conference*, Florida, USA, pp. 605-610, 1992.

[6] Nakagawa, P. M., Kawakami, F., and Kudoh, T., "Trends in Automotive Applications of Thermal Spray Technology in Japan", *Proceedings of the 7th National Thermal Spray Conference*, Boston, pp. 1-6, 1994.

[7] Nguyentat, T., Dommer, K. T., and Bowen, K. T., "Metallurgical Evaluation of Plasma Sprayed Structural Materials for Rocket Engines", *Proceedings of 13th International Thermal Spray Conference*, Florida, USA, pp. 321-326, 1992.

[8] Ohmori, A., "Thermal Spraying: Current Status and Future Trends", *Proceedings of the 14th International Thermal Spray Conference*, Kobe, Japan, ISSN 1241-3074, 1995.

[9] Herman, H., "Advances in Thermal-Spray Technology", *Journal of Advanced Materials and Processes*, Vol. 137 (4), 1990.

[10] Siegmann, S. and Brown, C. A., 1996. "Investigations on the Substrate Surface Morphology for Thermal Sprayed Coatings". *In: 17th International SAMPE Europe Conference: Success of Materials by Combination*, Basel, Switzerland, pp.149-158.

[11] Sampath, S., Jiang, X. Y., Matejicek, J., Prchlik, L., Kulkarni, A., Vaidya, A., 2004. "Role of Thermal Spray Processing Method on the Microstructure, Residual Stress and Properties of Coatings: An Integrated Study for Ni-5 wt.

%Al Bond Coats", *Journal of Materials Science and Engineering*, A364, pp.216-231.

[12] Information Documents and Technical Specifications, Castolin Eutectic Company Ltd.

[13] Sirohi, R. S., Tay, C. J., Shang, H. M., Boo, W. P., "Nondestructive Assessment of Thinning of Plates Using Digital Shearography". *Optical Engineering,* 38 (9), 1582-1585, 1999.

[14] Hung, Y. Y., "Shearography: A Novel and Practical Approach for Nondestructive Testing". *Journal of Nondestructive Testing*, 8(2) 55-67, 1989.

[15] Hung, Y. Y., "Shearography for Non-Destructive Evaluation of Composite Structures". *Opt. Lasers Eng.* 24, 161-182, 1996.

[16] Yang, L. X., Hung, Y. Y., "Digital Shearography for Nondestructive Evaluation and Application in Automotive and Aerospace Industries". *Proceedings of 16th World Conference on NDT*, Montreal, 2004.

[17] Foresight, "*Foresight in Surface Engineering: A Report by the Surface Engineering committee of the Institute of Materials*", Surface Engineering Committee of the Institute of Materials, 2000.

[18] Melford, D., "*A Study of Surface Engineering in the UK*", CEST, London, 1989.

[19] Halling, J., "Introduction". *In* J. Halling, *Recent Developments in Surface Coating and Modification Processes.* Mechanical Engineering Publication Ltd, London, 1985.

[20] Neale, M. J., Polak, T. A., Priest. M., "*Handbook of Surface Treatments and Coatings*", Professional Engineering Publishing Limited, UK, 2003.

[21] James, A. S., Thomas, K., Mann, P., Wall, R., "The Role and Impacts of Surface Engineering in Environmental Design". *Materials and Design*, Vol 26, 7, pp 594-601, 2005.

[22] Corrosion Cost in USA, *www.corrosioncost.com.* Corrosioncost, Accessed 20 March, 2004.

[23] Bhushan, B., and Gupta, B. K., "*Handbook of Tribology: Material Coating and Surface Treatments*", McGraw-Hill, New York, 1991.

[24] Stokes, J., "*Production of Coated and Free-Standing Engineering Components using the HVOF (High Velocity Oxy-Fuel) Process*". Ph.D.

Thesis, Materials Processing Research Centre, Dublin City University, Ireland, 2003.

[25] Dusa, K. M., "*Spraytime Magazine: ITSA Historical Collection Growing*". ASM Thermal Spray and International Thermal Spray Societies, Vol. 8 (2), 2001.

[26] Houben, J. M., "Future Developments in Thermal Spraying". *In:* F. N. Longo, ed. *2nd National Conference on Thermal Spray.* 31 October-2 November 1984 California. American Society for Metals, pp.1-19, 1985.

[27] Steffens, H. D., "Spray and Detonation Gun Technologies, Laser-assisted Techniques". *In* E. Lang, ed. *Coatings for High Temperature Applications.* Applied Science Publishers, pp.121-138, 1983.

[28] Parker, D. W., Kutner, G. L., "HVOF-Spray Technology-Poised for Growth", *Journal of Advanced Materials and Processes*, Vol. 139 (4), 1991.

[29] De Villiers Lovelock, H. L., Richter, P.W., Benson, J. M., and Young, P. M., "Parameter Study of HP/HVOF Deposited WC-Co Coatings", *Journal of Thermal Spray Technology*, Vol. 7 (1), 1998.

[30] Jacobs, L., Hyland, M. M., and De Bonte, M., "Comparative Study of WC-Cermet Coatings Sprayed Via the HVOF and HVAF Process", *Journal of Thermal Spray Technology*, Vol. 7 (2), 1998.

[31] Halling, J., "Chemical Vapour Deposition (CVD) for Surface Modification". *In* J. Halling, organized, *Recent Developments in Surface Coating and Modification Processes.* Mechanical Engineering Publication Ltd, London, 1985.

[32] Thermal Spray Coatings, *www.gordonengland.co.uk,* Gordon England, Accessed 23, September, 2005.

[33] John, V., "*Testing of Materials*". Macmillan, London, 1992.

[34] Holmberg, K., Mathews, A., "Coatings Tribology: A Concept, Critical Aspects and Future Directions", *Thin Solid Films*, 253 (1-2), 173-178, 1994.

[35] Tabor, D., "*The Hardness of Metals*", Charedon Press, Oxford. 1951.

[36] Chandler, H., "*Hardness Testing*", 2nd edition, ASM International, USA, 1999.

[37] ASTM B578-87, "*Standard Test Method for Microstructure-Hardness of Electroplated Coatings*", American Society for Testing and Materials Standards, Philadelphia, 1987.

[38] ASTM B18-94, "*Standard Test Method for Rockwell Hardness and Rockwell*

Superficial Hardness of Metallic Materials", American Society for Testing and Materials Standards, Philadelphia, 1994.

[39] ISO 4516, "*Metallic and Related Coatings – Vickers and Knoop Micro-hardness Tests*", International Standards, 1980.

[40] Maier, P., Richter, A., Faulkner, R. G. and Ries, R., "Application of Nanoindentation Technique for Structural Characterisation of Weld Materials". *Materials Characterization*, Volume 48, Issue 4, pp 329-339, 2002.

[41] Olivier, W. C., and Pharr, G. M., "An Improved Technique for Determining Hardness and Elastic Modulus Using Load Displacement Sensing Indentation Experiments". *Journal of Material Research*, 7, pp 1564–1583, 1992.

[42] Smith, M. F., McGuffin, D. T., Henfling, J. A., and Lenling, W. B., "A Comparison of Techniques for the Metallographic Preparation of Thermal Sprayed Samples", *Proceedings of the 4th National Thermal Spray Conference*, Pittsburgh, USA, pp. 97-104, 1991.

[43] BS EN ISO 4287:2000, "*Geometrical Product Specification (GPS) - Surface Texture: Profile Method - Terms, Definitions and Surface Texture Parameters*". British Standard, 2000.

[44] BS 1134-1:1988, "*Assessment of Surface Texture - Part 1: Methods and Instrumentation*". British Standard, 1988.

[45] Roberts, S. G. and Briggs, G. A. D., "*Characterization of Surface Roughness and Subsurface Damage*", Final Report on EPSRC, Oxford University, 1996.

[46] Bilgen, M. and Rose, J. H., "Focused Ultrasonic Probes and the Effects of Surface Roughness on Material Noise", in "*Review of Progress in Quantitative Non-destructive Evaluation*", Ed. by D. O. Thompson and D. E. Chimenti, Vol. 13B, pp 1769- 1776, 1993.

[47] Hilton, P. J., "*Image Surface Roughness Using Correlated Speckle Grain Pairs*", Report No. DICTA/IVCNZ97, pp 349-354, Massey University, New Zealand. 1997.

[48] Ohtsubo, J., "Measurement of Roughness Properties of Diamond-turned Metal Surfaces Using Light-Scattering Method". *Journal of the Optical Society of America A*, 3(7) 982-7, 1986.

[49] Peiponen, K. E., Tsuboi, T., "Metal Surface Roughness and Optical Reflectance". *Optical & Laser Technology*, 22(2) 127-30, 1990.

[50] Stover, J. C., Serati, S. A., "Calculation of Surface Statistics from Light Scatter". *Optical Engineering*, 23, 406, 1984.

[51] Gorecki, C., "Surface Classification by an Optoelectronic Implementation of the Karhunen-Loeve Expansion". *Applied Optics*, 30, 4548, 1991.

[52] Fujii, H., Asakura, T., Shindo, Y., "Measurement of Surface Roughness Properties by Using Image Speckle Contrast". *Journal of the Optical Society of America*, 66(11), 1217-21, 1976.

[53] Leonard, L. C., Toal, V., "Roughness Measurement of Metallic Surfaces Based on the Laser Speckle Contrast Method", *Optics and Lasers in Engineering*, 30(5), 433-440, 1998.

[54] Léger, D., Mathieu, E., Perrin, J. C., "Optical Surface Roughness Determination Using Speckle Correlation Technique". *Applied Optics*. 14, 872, 1975.

[55] Léger, D., Perrin, J. C., "Real-time Measurement of Surface Roughness by Correlation of Speckle Patterns". *Journal of the Optical Society of America*, 66(11) 1210-7, 1976.

[56] Hertwig, M., "Application of Improved Speckle Contouring Technique to Surface Roughness Measurements". *Optics and Lasers in Engineering*, 26, 115-130, 1997.

[57] Withers, P. J., Bhadeshia, H. K. D. H., "Residual Stress, Part 1 – Measurement Techniques", *Materials Science and Technology*, Vol.17, pp.355-365, 2001.

[58] Clyne, T. W., "Residual Stresses in Surface Coatings and Their effects on Interfacial Debonding", *Key Engineering Materials*, Vol. 116-117, pp. 307-330, 1996.

[59] Clyne, T. W., Gill, S. C., "Residual Stresses in Surface Coatings and Their effects on Interfacial Debonding: A Review of Recent Work", *J. Thermal Spray Technology*, Vol. 5 (4), pp.401-418, 1996.

[60] Schajer, G. S., Roy, G., Flaman, M. T., Lu, J., "Title". *In* J. Lu, ed. *Handbook of Measurement of Residual Stresses*. Lilburn, GA, Society for Experimental Mechanics, pp. 5-34, 1996.

[61] Wang, Y. Y., Chiang, F. P., "Experimental Study of Three-dimensional Residual Stresses in Rails by Moirés Interferometry and Dissecting Methods", *Optics and Laser Engineering*. 1997, 27, pp. 89-100, 1997.

[62] McDonach, A., McKelvie, J., MacKenzie, P. M., and Walker, C. A., "Improved Moire Interferometry and Applications in Fracture Mechanics, Residual Stress and Damaged Composites". *Exp. Tech.*, 7, 20-4, 1983.

[63] Nelson, D. V. and McCrickerd, J. T., "Residual-Stress Determination through Combined Use of Holographic Interferometry and Blind Hole Drilling". *Exp. Mech.*, 26, 371-8, 1986.

[64] Bass, J. D., Schmitt, D., and Ahrens, T. J., "Holographic in situ Stress Measurements". *Geophys. J. R. Astr. Soc.*, 85, 13-41, 1986.

[65] Nelson, D. V., Makino, A., and Fuchs, E. A., "The Holographic-hole Drilling Method for Residual Stress Determination". *Optics & Lasers in Engineering*, Vol 27, No. 1, pp. 3-23, 1997.

[66] Hung, Y. Y., Long, K. W., and Wang, J. Q., "Measurement of Residual Stress by Phase Shift Shearography". *Optics & Lasers in Engineering*, Vol 27, No. 1, pp. 61-73, 1997.

[67] Zukas, J. A., Nicholas, T., et al., "*Impact Dynamic*", John Wiley and Sons Inc., New York, 1982.

[68] Hatanaka, H., Arakawa, T., "Ultrasonic Examination of Thermal Sprayed Coatings with Frequency Analysis". *Proceedings of 15th World Conference on NDT*, Roma, 2000.

[69] Silva Gomes, J. F., Vaz, M. A. P., "Laser Interferometry Techniques in Experimental Stress Analysis and N.D.T. of Structures and Materials". *Keynote Lecture-Mechanics in Design*. Universidade de Toronto, Canada, 1996.

[70] Jones, R., Wykes, C., "*Holographic and Speckle Interferometry*", 2nd edition, Cambridge University Press, Cambridge. 1989.

[71] Mihaylova, E.. Toal, V., Martin, S., Bowe, B., "Mechanical Characterization of Polyvinylchloride Pipes Using Electronic Speckle Pattern Interferometry". *OPTO-IRELAND - SPIE's Regional Meeting on Optoelectronics, Photonics and Imaging*, Galway, Ireland, pp.994-1007, 2002.

[72] Owner-Petersen M., "Decorrelation and Fringe Visibility: on the Limiting Behaviour of Various Electronic Speckle-Pattern Correlation Interferometers", *Journal of the Optical Society of America*. A 8, 1082-1089, 1991.

[73] Silva Gomes, J. F., Monteiro, J. M., Vaz, M. A. P., "NDI of Interfaces in Coating Systems Using Digital Interferometry". *Mechanics of Materials.* 32, 837-843, 2000.

[74] Albrecht, D., "*Electronic Speckle Pattern Interferometry Instruments Development, Optimisation and applications*", PhD thesis, Loughborough University, UK, 1998.

[75] Yang, L., Chen, F., Steinchen, W., Hung, M. Y., "Digital shearography for nondestructive testing: potentials, limitations and applications". *J. Holography and Speckles,* V1, 2, pp 69-79, 2004.

[76] Steinchen, W., Yang, L. X., "*Digital Shearography - Theory and Application of Digital Speckle Pattern Shearing Interferometry*". SPIE Press, Washington, USA, 2003.

[77] Joenathan, C., "Speckle Photography, Shearography, and ESPI". *In* P. K. Rastogi, ed. *Optical Measurement Techniques and Applications*, Attech House, pp.151-182, 1997.

[78] Malmo, J. T., Lokberg, O. J., and Slettemoen, G. A., "Interferometric Testing at Very High Temperatures by TV Holography (ESPI)", *Experimental. Mechanics*, Vol. 28, pp.315-322, 1988.

[79] Lokberg, O. J., Jones, R. C., and Wykes, C., "Electronic Speckle Pattern Interferometry". *In*: R. S. Sirohi, ed. *Speckle Metrology.* Marcel Dekker, New York, pp.157-194, 1993.

[80] Hung, Y. Y., "Applications of Digital Shearography for Testing of Composite Structures", *Composites, Part B: engineering*, 30, 765-773, 1999.

[81] Recent Developments in Digital Speckle Pattern Interferometry, Guest ed, *Optics and Lasers in Engineering*, Vol. 40, pp.439-445, 2003.

[82] Krupka, R., Walz, T., Ettemeyer. A., "Industrial Applications of Shearography for Inspection of Aircraft Components". *Proceedings of 8th European Conference on NDT*, Barcelona, Spain, June 17-21, 2002.

[83] Mayer, T., Scherling, D., Sun, J., "Shearography Testing on Aerospace CFRP Components". *Proceedings of 8th European Conference on NDT*, Barcelona, Spain, June 17-21, 2002.

[84] Maji, A. K., Satpathi, D., Zawaydeh, S., "Assessment of Electronic Shearography for Structural Inspection", *Experimental Mechanics,* 37, 2, 197-204, 1997.

[85] Hung, Y. Y., and Shi, D., "Technique for Rapid Inspection of Hermetic Seals of Microelectronic Packages Using Shearography", *Optical Engineering*, 37, 5, 1406-1409, 1998.

[86] Collett, C. V., Hope, A. D., "*Engineering Measurements*", 2nd ed. Longman Scientific & Technical, London, 1983.

[87] Young, M., "*Optics and Lasers, Including Fibers and Optical Waveguides*", Springer, 2000.

[88] Gåsvik, Kjell J., "*Optical Metrology*". 2nd ed. John Wiley & Sons, England, 1995.

[89] Butters, J. N., Jones, R. C., and Wykes, C., "Electronic Speckle Pattern Interferometry". In: R. K. Erf, ed. *Speckle Metrology*. Springer Verlag, pp 111-157, 1975.

[90] Bowe, B., Martin, S., Toal, V., Langhoff, A., Whelan, M., "Dual In-Plane Electronic Speckle Pattern Interferometry System with Electro-Optical Switching and Phase Shifting", *Applied Optics*, 38 No 4, pp.666-673, 1999.

[91] Toal, V., Rice, H., Meskell, C., Armstrong, C., Bowe, B., "Evaluation of High Frequency Vibrations Using Electronic Speckle Pattern Interferometry". *OPTO-IRELAND - SPIE's Regional Meeting on Optoelectronics, Photonics and Imaging*, Galway, Ireland, pp.1054-1063, 2002.

[92] Rastogi, P. K., "Techniques of Displacement and Deformation Measurements in Speckle Metrology". *In*: R. S. Sirohi, ed. *Speckle Metrology*. Marcel Dekker, New York, pp.41-98, 1993.

[93] Kuroda, S., Clyne, T. W., "The Quenching Stress in Thermally Sprayed Coatings", *Thin Solid Films*, Vol. 200, pp. 49-66, 1991.

[94] Quenching Stress, *www.msm.cam.ac.uk/mmc/research*, Composites and Coating Group, Cambridge University, Accessed 23, September 2005.

[95] Pawlowski, L., "*The Science and Engineering of Thermal Spray Coatings*", Wiley and Sons, London, 1995.

[96] Bianchi, L., Baradel, N., Liorca-Isern, N., and Bertran-Vidal, G., "Influence of Plasma Spraying Parameters on Coating Damage", *Proceedings from the First International Thermal Spray Conference (ITSC'00)*, Montreal, Canada, pp. 29 – 36, 2000.

[97] Mellali, M., Grimaud, A., Frauchais, P., "Parameters controlling the sand blasting of substrates for plasma spraying". *Proceedings of the 7th National Thermal Spray Conference*, Boston, pp. 227-232, 1994.

[98] Glancy, S. D., "How Metallographic Preparation Affects the Microstructure of WC/Co Thermal Spray Coatings", *Proceedings of the 7th National Thermal Spray Conference*, Boston, pp. 771-777, 1994.

[99] Glancy, S. D., "Preserving the Microstructure of Thermal Spray Coatings". *Journal of Advanced Materials and Processes*, Vol. 148 (1), pp. 37-40, 1995.

[100] Petzow, G., Carle, V., and Harnisch, U., 2nd edition, *"Metallographic Etching"*, ASM International, The Materials Information Society, 1999.

[101] Gabe, D. R., *"Principles of Metal Surface Treatment and Protection"*, 2nd edition, Pergamon Press, Oxford, England, 1978.

[102] Mihaylova, E., Lyng, F., and Faoláin, E., "Comparison of Surface Roughness Measured with a White Light Profilometer, a Confocal Microscope and a Stylus Profilometer", *26th Annual M.S.I. Meeting*, Galway, Ireland, 2002.

[103] Bhushan, B., *"Handbook of Micro/Nano Tribology"*, CRC Press, 1999.

[104] Fischer-Cripps, A., *"Nanoindentation"*, Springer, 2002.

[105] Schneider, D., Schwaz, T., Schultrich, B., "Determination of Elastic Modulus and Thickness of Surface Layers by Ultrasonic Surface Waves", *Thin Solid Films*, Vol. 219, n1-2, pp 92-102, 1992.

[106] Fang, W., "Determination of the Elastic Modulus of Thin Film Materials Using Self-Deformed Micromachined Cantilevers", *Journal of Micromechanics and Microengineering*, Vol. 9, n3, pp 230-235, 1999.

[107] Rybicki, E. F., Shadley, J. R., Xiong, Y., and Greving, D. J., "A Cantilever Beam Method for Evaluation of Young's Modulus and Poisson's Ratio of Thermal Spray Coatings". *Journal of Thermal Spray Technology*, Vol. 4 (4), pp. 377-383, 1995.

[108] Richard, C. S., Béranger, G., Lu, J., Flavenot. J. F., and Grgoire, T., "Four-Point Bending Tests of Thermally Produced WC-Co Coatings", *Journal of Surface and Coatings Technology*, Vol. 78, pp 284-294, 1996.

[109] Nakahira, H., Tani, K., Miyajima, K., and Harada, Y., "Anisotropy of Thermally Sprayed Coatings", *Proceedings of the 13th International Thermal Spray Conference*, Florida, USA, pp. 1011-1017, 1992.

[110] ASTM E837-96, "*Determining Residual Stresses by the Hole-Drilling Strain-Gage Method*", American Society for Testing and Materials Standards, Philadelphia, USA, 1996.

[111] Measurements Group, "Measurement of Residual Stresses by the Hole-Drilling Strain Gauge Method," *Tech Note TN-503-4*, Measurements Group, Inc., Raleigh, NC, USA, 2000.

[112] ASTM Standard E1561-96, "*Analysis of Strain Gage Rosette Data*", American Society for Testing and Materials Standards, Philadelphia, USA, 1996.

[113] Rendler, N. J., et. al, "The Hole Drilling Strain Gauge Method of Measuring Residual Stresses", *Experimental Mechanics*, Vol. 6, pp. 577-586, 1966.

[114] Tsui, Y. C., Clyne, T. W., "An Analytical Model for Predicting Residual Stresses in Progressively Deposited Coatings, Part 1: Planar Geometry", *Thin Solid Films*, 306, 23-33, 1997.

[115] Clyne, T. W., "Residual Stresses in Thick and Thin Surface Coatings", *Encyclopaedia of Materials: Science and Technology, 4.1.3b - "Composites: MMC, CMC, PMC*, A. Mortensen (ed.), Elsevier, 2001.

[116] Mihaylova, E., Murphy, N., Xue, Y., Kennedy, D., Toal, V., "Test Rig Design for Optical Inspection of Metal Samples by Electronic Speckle Pattern Shearing Interferometry". *Proceedings of MATRIB'04*, p. 33. Vela Luka, Croatia, 2004.

[117] Mihaylova, E. M., Whelan, M. P., Toal, V., "A Simple Phase-Shifting Lateral Shearing Interferometer", *Optics Letters*. 29 (11), 1264, 2004.

[118] Xue, Y., Kennedy, D., Mihaylova, E., "Electronic Speckle Pattern Shearing Interferometry for Non-Destructive Testing of Thermal Sprayed Alloy Coatings". *Proceedings of SPIE OPTO-Ireland 2005*. Vol. 5824, pp. 241-249, Ireland, 4-6. 04. 2005.

[119] Vijgen, R. O. E., and Dautzenberg, J. H., "Mechanical Measurement of the Residual Stress in thin PVD Films", *Journal of Thin Solid Films*, Vol. 270, pp. 264 – 269, 1995.

[120] Senderoff, S., and Brenner, A., "*Journal of Research, National Bureau of Standards*", Vol. 42 (2), pp. 105-123, 1949.

[121] Tipton, A. A., "The Effect of HVOF Sprayed Coatings on the Elevated Temperature High Cycle Fatigue Behaviour of a Martensitic Stainless Steel",

Proceedings of the 8th National Thermal Spray Conference, Houston, Texas, pp. 463 – 468, 1995.

[122] BS 1134-2:1990, "*Assessment of Surface Texture - Part 2: Guidance and General Information*". British Standard, 1990.

[123] Kennedy, D., "*Surface Engineering*", Chairman's Address, Presentation Notes, IEE Irish Branch Programme 2004/2005, 2004.

Appendix I – Hole Drilling Method (Measurement Group)

RS-200 Milling Guide

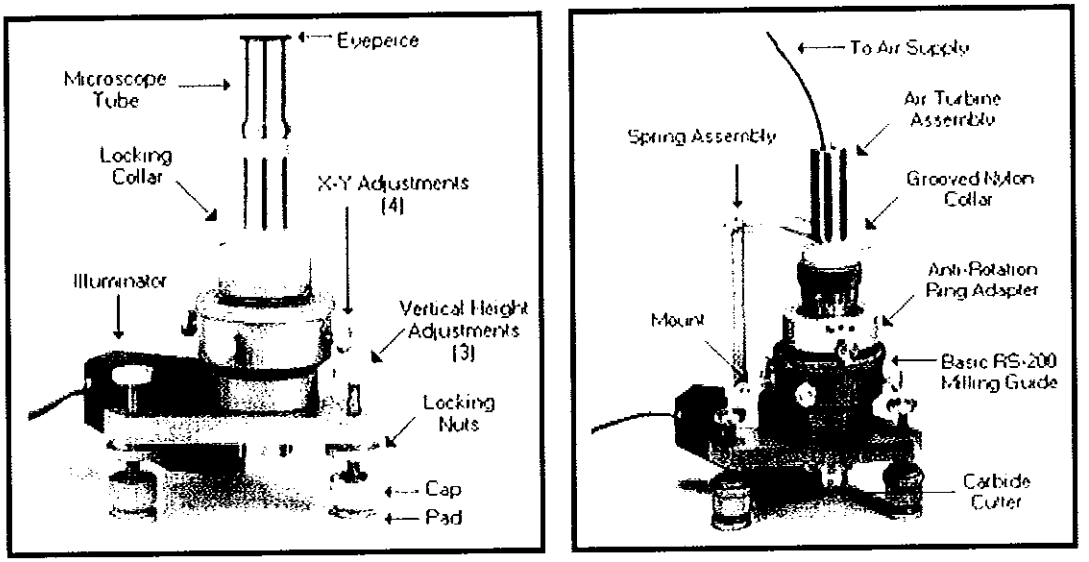

(a) (b)

Figure A1. RS-200 Milling Guide, (a) with Eyepiece; (b) with Air Turbine

Figure A1 (a) shows the required alignment (precision within 0.025 mm), which is accomplished using the RS-200 Milling Guide.

Figure A1 (b) shows the air turbine/carbide cutter assembly installed using the RS-200 Milling Guide.

Figure A2. Example of the Hole Drilling Method Procedure

Briefly summarised, the measurement procedure involves six basic steps:

i. A special three-element strain gage rosette is installed on the test part at the point where residual stresses are to be determined.
ii. The three gage grids are wired and connected to a static strain indicator through a switch-and-balance unit.
iii. A precision milling guide (Model RS-200, shown above) is attached to the test part and accurately centered over a drilling target on the rosette.
iv. After zero-balancing the gage circuits, a small, shallow hole is drilled through the center of the rosette.
v. Readings are made of the relaxed strains, corresponding to the initial residual stress.
vi. Using special data-reduction relationships provided here, the principal residual stresses and their angular orientation are calculated from the measured strains.

The foregoing procedure is relatively simple, and has been standardised in ASTM Standard Test Method E837.

In most practical applications of the method, the drilled hole is blind, with a depth which is: (a) about equal to its diameter, and (b) small compared to the thickness of the test object.

Through-hole analysis

Figure A3 depicts a local area within a thin plate which is subject to a uniform residual stress, σ_x.

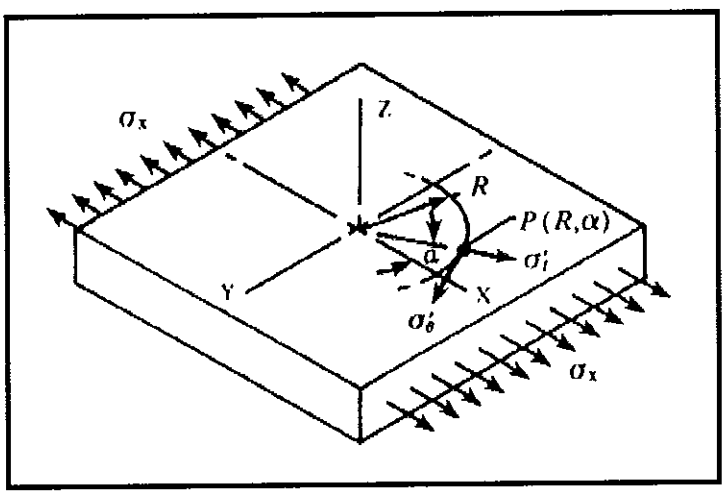

Figure A3. Stress States at P (R, α) Before the Introduction of a Hole

The initial stress state at any point *P (R, α)* can be expressed in polar coordinates by:

$$\sigma_r = \frac{\sigma_x}{2}(1+\cos 2\alpha) \qquad \text{Equation 1a}$$

$$\sigma_\theta = \frac{\sigma_x}{2}(1-\cos 2\alpha) \qquad \text{Equation 1b}$$

$$\sigma_{r\theta} = -\frac{\sigma_x}{2}(\sin 2\alpha) \qquad \text{Equation 1c}$$

Figure A4 represents the same area of the plate after a small hole has been drilled through it.

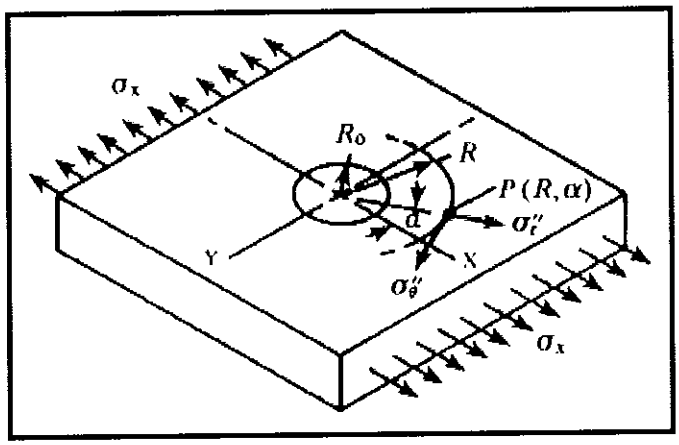

Figure A4. Stress States at P (R, α) After the Introduction of a Hole

The stresses in the vicinity of the hole are now quite different, since σ_r, and $\tau_{r\theta}$ must be zero everywhere on the hole surface. A solution for this case was obtained, and the following expressions for the stresses at the point *P (R, α)* have been made:

$$\sigma_r'' = \frac{\sigma_x}{2}(1-\frac{1}{r^2}) + \frac{\sigma_x}{2}(1+\frac{3}{r^4}-\frac{4}{r^2})\cos 2\alpha \qquad \text{Equation 2a}$$

$$\sigma_\theta'' = \frac{\sigma_x}{2}(1+\frac{1}{r^2}) - \frac{\sigma_x}{2}(1+\frac{3}{r^4})\cos 2\alpha \qquad \text{Equation 2b}$$

$$\tau_{r\theta}'' = -\frac{\sigma_x}{2}(1-\frac{3}{r^4}+\frac{4}{r^2})\sin 2\alpha \qquad \text{Equation 2c}$$

Where:

$$r = \frac{R}{R_0}(R \geq R_0)$$

R_0 = hole radius, R = arbitrary radius from hole center

Assume the material of the plate is homogeneous and isotropic in its mechanical properties, and linear-elastic in its stress/strain behavior, the equations can be substituted into the biaxial Hooke's law to solve for the relieved normal strains at the point *P (R, α)*. The resulting expressions are as follows:

$$\varepsilon_r = -\frac{\sigma_x(1+\nu)}{2E}[\frac{1}{r^2} - \frac{3}{r^4}\cos 2\alpha + \frac{4}{r^2(1+\nu)}\cos 2\alpha] \quad \text{Equation 3a}$$

$$\varepsilon_r = -\frac{\sigma_x(1+\nu)}{2E}[\frac{1}{r^2} - \frac{3}{r^4}\cos 2\alpha + \frac{4}{r^2(1+\nu)}\cos 2\alpha] \quad \text{Equation 3b}$$

The preceding equations can be written in a simpler form as:

$$\varepsilon_r = \sigma_x(A + B\cos 2\alpha) \quad \text{Equation 4a}$$

$$\varepsilon_\theta = \sigma_x(-A + C\cos 2\alpha) \quad \text{Equation 4b}$$

The coefficients A, B, and C have the following definitions:

$$A = -\frac{(1+\nu)}{2E}(\frac{1}{r^2}) \quad \text{Equation 5a}$$

$$B = -\frac{(1+\nu)}{2E}[(\frac{4}{1+\nu})\frac{1}{r^2} - \frac{3}{r^4}] \quad \text{Equation 5b}$$

$$C = -\frac{(1+\nu)}{2E}[-(\frac{4\nu}{1+\nu})\frac{1}{r^2} + \frac{3}{r^4}] \quad \text{Equation 5c}$$

When both residual stresses are present simultaneously, the general expression for the relieved radial strain due to a plane biaxial residual stress state is:

$$\varepsilon_r = \sigma_x(A + B\cos 2\alpha) + \sigma_y(A - B\cos 2\alpha) \quad \text{Equation 6}$$

The common procedure for measuring the relieved strains is to mount three resistance strain gauges in the form of a rosette around the site of the hole before drilling. The schematic diagram of a rosette is shown in Figure A5, where three radially oriented strain gauges are located with their centers at the radius R from the center of the hole site.

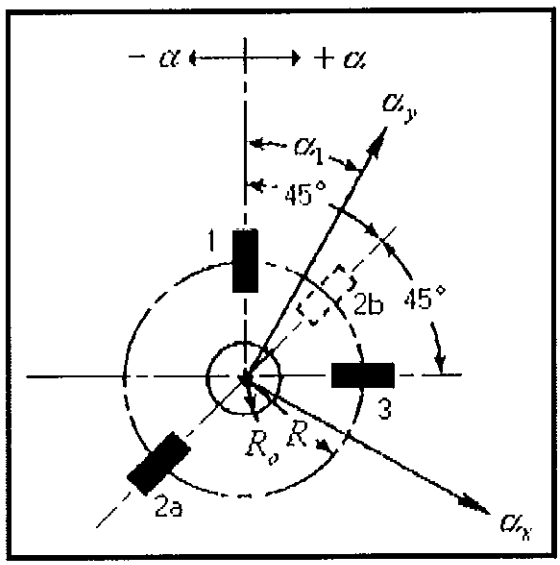

Figure A5. Strain Gauge Rosette Arrangement for Determining Residual Stress

As indicated above, α_1 is the acute angle from the nearer principal axis to gage no. 1, while $\alpha_2 = \alpha_1 + 45°$ and $\alpha_3 = \alpha_1 + 90°$, with positive angles measured in the direction of gauge numbering.

Equation 6 can now be written three times, once for each gauge in the rosette:

$$\varepsilon_1 = A(\sigma_x + \sigma_y) + B(\sigma_x - \sigma_y)\cos 2\alpha \qquad \text{Equation 7a}$$

$$\varepsilon_2 = A(\sigma_x + \sigma_y) + B(\sigma_x - \sigma_y)\cos 2(\alpha + 45°) \qquad \text{Equation 7b}$$

$$\varepsilon_3 = A(\sigma_x + \sigma_y) + B(\sigma_x - \sigma_y)\cos 2(\alpha + 90°) \qquad \text{Equation 7c}$$

When Equations 7 are solved simultaneously for the principal stresses and their direction, the results can be expressed as:

$$\sigma_{max} = \frac{\varepsilon_3 + \varepsilon_1}{4A} - \frac{\sqrt{(\varepsilon_3 - \varepsilon_1)^2 + (\varepsilon_3 + \varepsilon_1 - 2\varepsilon_2)^2}}{4B} \qquad \text{Equation 8a}$$

$$\sigma_{min} = \frac{\varepsilon_3 + \varepsilon_1}{4A} + \frac{\sqrt{(\varepsilon_3 - \varepsilon_1)^2 + (\varepsilon_3 + \varepsilon_1 - 2\varepsilon_2)^2}}{4B} \qquad \text{Equation 8b}$$

$$\tan 2\alpha = \frac{\varepsilon_3 + \varepsilon_1 - 2\varepsilon_2}{\varepsilon_3 - \varepsilon_1}$$ Equation 8c

Where

$$A = -\frac{1+\nu}{2E} \times \bar{a}$$ Equation 9a

$$B = -\frac{1}{2E} \times \bar{b}$$ Equation 9b

The $\bar{a}$ and $\bar{b}$ coefficients for Micro-Measurements residual stress rosette are provided graphically in Figure A6, where the solid lines apply to full-depth blind holes and the dashed lines to the through holes. It is assumed that in both cases that the initial residual stress is uniform with depth. Through-hole coefficients were obtained by numerically integrating the expressions, for the relieved longitudinal strains along the individual gridlines.

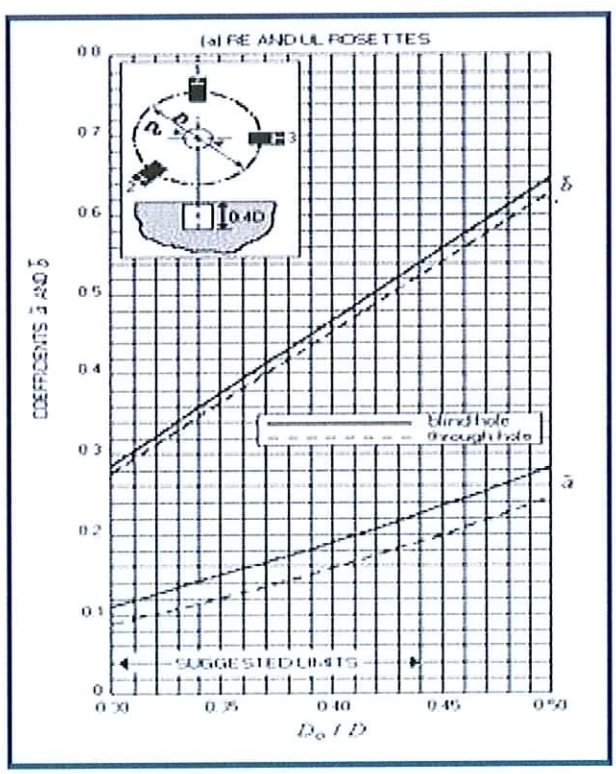

Figure A6. Data-Reduction Coefficients $\bar{a}$ and $\bar{b}$ Versus Dimensionless Hole Diameter for Measurements Group Residual Stress Rosettes

Appendix II – Optical System Apparatus and Software Specifications

1. Framegrabber hardware – data translation DT 2861 16 buffer fgrabber.
2. Uniphase He-Ne class IIIb laser.
3. Oriel encoder Mike controller. Minimum step 22.4 arcsec (for rotator).
4. Panasonic high performance CCD camera, 512 x 512 pixels.
5. High resolution Fujinon HF25HA-1 zoom lens with C-mount, focal length 25mm.
6. Newport optical bench and optics used throughout.
7. Framegrabber software: "Fgrabber", written by A. Langhoff © European commission Joint Research Centre, Ispra, Italy.
8. C-832 DC motor controller operating prigram © Physik Instruments (PI) GmbH, Germany.

List of Publications

1. Xue, Y., Kennedy, D., Mihaylova, E., "Thermal Spraying and Optical Characterisation of Alloy Surface Coatings". *Proceedings of MATRIB'04*, pp. 338-343, Vela Luka, 23-25. 06. 2004.
2. Mihaylova, E., Murphy, N., Xue, Y., Kennedy, D., Toal, V., "Test Rig Design for Optical Inspection of Metal Samples by Electronic Speckle Pattern Shearing Interferometry". *Proceedings of MATRIB'04*, pp. 172-177, Vela Luka, 23-25. 06. 2004.
3. Xue, Y., Kennedy, D., Mihaylova, E., "Electronic Speckle Pattern Shearing Interferometry for Non-Destructive Testing of Thermal Sprayed Alloy Coatings". *Proceedings of SPIE OPTO-Ireland 2005*, Vol. 5824, pp. 241-249, Ireland, 4-6. 04. 2005.
4. Xue, Y., Kennedy, D., Mihaylova, E., "Current and Future Applications of Surface Engineering". *The Engineers Journal*, Vol. 59, pp. 287-292, 2005.